POLITECNICO
MILANO 1863

Department of Mathematics
Doctoral Programme in Mathematical Models and Methods in Engineering

Parallel Mixed-mode 3D-TCAD Simulation of Power Semiconductor Devices

Doctoral Dissertation of:
Davide Cagnoni

Advisor:
Prof. Carlo de Falco

Co-advisor:
Dr. Marco Bellini

Tutor:
Prof. Roberto Lucchetti

The Chair of the Doctoral Program:
Prof. Roberto Lucchetti

XXVIII Cycle

al mio dono più grande

Contents

Contents v

1. Introduction 1

1.1. Power semiconductor devices . . . 3
1.1.1. Rectifying p-i-n power diodes . . . 3
1.1.2. Thyristors . . . 4
1.1.3. Numerical simulation for power electronics . . . 7

I. Mathematical and physical models 11

2. The Drift–Diffusion Model for Charge Transport 13

2.1. PDE Conservation Laws . . . 13
2.1.1. Poisson's equation . . . 13
2.1.2. Charge transport equations . . . 15
2.1.3. The drift–diffusion currents . . . 15
2.2. Constitutive Relations for System Coefficients . . . 16
2.2.1. Band–gap Narrowing . . . 16
2.2.2. Charge Density and Electric Field Dependent Mobility . . . 20
2.2.3. Charge Carrier Generation and Recombination . . . 24
2.3. Boundary Conditions . . . 31
2.3.1. Ohmic contacts . . . 32
2.3.2. Contact currents . . . 34
2.4. Conditioning of the Drift–Diffusion System . . . 35
2.4.1. Non–dimensional Form and Scaling . . . 35
2.4.2. Conditioning Analysis . . . 36

3. Lumped–Element Electrical Circuits 39

3.1. Modified Nodal Analysis . . . 39
3.1.1. Network–level conservation laws . . . 39
3.1.2. Standard device models and MNA . . . 42
3.2. Coupling Lumped-Element Circuit and Distributed Devices . . . 44
3.3. Analytical Results for the Coupled System . . . 47

II. Numerical algorithms 53

4. Time Discretization 55
4.1. Implicit Schemes for DAE . . . 55
4.2. Time–step Adaptivity . . . 56

5. Nonlinear Iterations 59
5.1. The Gummel Map . . . 59
5.2. Newton's Method . . . 61
5.2.1. Newton–like methods . . . 62
5.2.2. Implementation of the nonlinear solver . . . 65

6. Space Discretization 73
6.1. The Diffusion–Reaction Problem . . . 74
6.2. The Galerkin/Finite Element Method . . . 75
6.3. The Edge Averaged Finite Element (EAFE) Method . . . 78
6.4. Exponential Fitting . . . 80
6.5. 3D Extension of the EAFE Method . . . 81

7. Solution of the Linearized System 83
7.1. LU Factorization and Fill–in . . . 83
7.2. Block Gauß–Seidel Iterations . . . 86
7.2.1. Device–circuit coupling . . . 87

III. Test cases 93

8. Validation of the Physical Models 95
8.1. Band gap narrowing model . . . 95
8.2. Carrier lifetimes model . . . 97
8.3. Mobility models . . . 99
8.4. Trap assisted generation–recombination . . . 101
8.5. Impact ionization model . . . 102

9. *p-i-n* Power Diode 111
9.1. Simulation in Quasi–static Regime . . . 111
9.2. Simulation in AC Regime . . . 114
9.3. Reverse Recovery Simulation . . . 120

10. Thyristor 125
10.1. Depletion Simulation . . . 125
10.2. Phase Controlled Thyristor . . . 129

11. Conclusions 133

Appendix **137**

A. Circuital examples **137**

1. Introduction

Figure 1.1.: An array of thyristor valves in an ABB HVDC converter station. (image from [12])

The push for deployment of renewable energy technologies across the EU is generating transformation pressure on the transmission infrastructure. In particular, the role High Voltage Direct Current (HVDC) technology in the grid is growing [10]. Novel Power Semiconductor devices such as the BiGT [15, 1, 7] or improvements in well–proven devices such as the thyristor [16, 13, 17] (see figure 1.2) are a key enabling technology allowing for the feasibility of HVDC grids [15, 1, 7, 6, 8], see figure 1.1.

Technology Computer Aided Design (TCAD) simulations play a key role in the development and optimization of new devices. As complex geometries [7] are an important ingredient for optimal performance of high power, large area semiconductor devices, full scale 3D simulations are required [11, 18]. Large current densities and fast switching speeds, lead to non–negligible multi–physics effects such as interactions of charge transport with substrate heating [18, 4, 2].

The complexity of the physical phenomena that govern the performance of new and advanced device structures makes it extremely difficult to develop compact

models for them. Furthermore, available compact models depend on a very large number of parameters, that require a lengthy and expensive tuning procedure in order to be accurate over a wide range of operating conditions [14]. For such reason in the technology design phase it is often required to perform mixed–mode simulations, i.e., to simulate the device performance when coupled to controlling circuit and load [18, 9].

The present thesis was carried out in the framework of a collaboration between the Modeling and Scientific Computing (MOX) lab of Politecnico di Milano, and the Power Electronics department in the Corporate Research Center of ABB in Baden–Dättwil, Switzerland aimed at implementing a parallel 3D TCAD simulator especially tailored for the needs of the Power Semiconductors industry in general and for those of ABB in particular.

The resulting C++ code, named CGDD++, was developed from scratch during the preparation of the present thesis, building on the experience gained during a preliminary feasibility study and the Fortran 2003 code (CGDD) that was implemented during that preliminary phase and was based on the FEMilaro [20] library.

CGDD++ relies on the BIM++ [19] library for spatial discretization of differential operators and uses MUMPS [22] or LIS [21] for the solution of linear systems of algebraic equations.

The development of CGDD was partially supported by the SuperComputing Applications and Innovations (SCAI) department of CINECA, Italy through the Interdisciplinary Laboratory for Advanced Simulation (LISA) projects 3DSPEED (3D Simulation of PowEr Electronics Devices, 2014) and PDDD (3D Power electronics Drift Diffusion Device simulation, 2013).

The main feature of CGDD++, which were the objective of this thesis, is the ability to allow implementation and testing of a wide range numerical algorithms suited for very large scale parallel mixed–mode simulation of Power Semiconductor devices, including electro–thermal effects.

Particular emphasis was devoted during the development of this thesis to the implementation and assessment of various linear and nonlinear iteration strategies.

In the remaining part of this chapter we introduce briefly two important classes of Power Semiconductor devices, in order to outline their peculiarities that drive the selection of physical models and numerical algorithms employed in this thesis work, a full outline of the rest of the thesis is given at the end of the chapter.

Figure 1.2.: An ABB Phase controlled thyristor, with wafer and packaging. (image from [12])

1.1. Power semiconductor devices

In this section we briefly introduce two very common power semiconductor device structures and their basic working principles. The purpose of the section is not an in–depth discussion of the physics of such devices (for which we refer the interested reader to, *e.g.*, [3]) but rather to outline the specific features of such devices that are relevant for the development of a numerical simulator.

Section 1.1.1 introduces the basic features of *p*-*i*-*n* rectifying power diodes, while section 1.1.2 discusses the principles of operation of the thyristor. Finally section 1.1.3 collects the features previously highlighted, which a simulation tool needs to handle when dealing with power devices.

1.1.1. Rectifying *p*-*i*-*n* power diodes

Power diodes are blocking devices based on a doping profile of type p^+-n^--n^+, where the large *drift* region inbetween is almost intrinsic (hence the *p*-*i*-*n* denomination). Such doping profile allows the device to attain much higher breakdown voltage ratings, since most of the bias is sustained by the low doping region, limiting the maximum electric field in the junction. From an application perspective, power diodes can be divided in two classes:

- rectifying diodes for grid voltages at 50-60 Hz frequencies, with high carrier lifetimes in the drift region;
- fast recovery diodes, commuting with frequencies up to 20 kHz, where the carrier lifetime in the drift region need to be reduced.

The parameter governing the diode characteristic is the length of the intrinsic region w_{B} which determines the maximum blocking voltage, as it matches the

depletion region for sufficiently high reverse bias. The breakdown voltage V_{bd} follows approximately a power law: $V_{\mathrm{bd}} \propto w_{\mathrm{B}}^{-8/7}$. When the breakdown voltage is reached, the avalanche multiplication caused by impact ionization (which is discussed in section 2.2) produces enough carriers to enable conduction.

The transition of the diode from the blocking state to the on–state is accompanied by an overshoot in the anode voltage which increases the power dissipation. This phenomenon is referred to as the *forward recovery.* When the diode switches from the on–state to the reverse–blocking state, the stored charge within the drift region of the power rectifier must be extracted before it is able to support high voltages. This produces a large reverse current for a short time duration. This phenomenon is referred to as the *reverse recovery*, and produces even greater power losses.

During reverse recovery, the current does not monotonically reduce to zero. If the reversal in the voltage is performed with a circuit comprising a voltage source and a series resistance, a constant reverse current is observed immediately after the voltage changes from its positive value to a negative value. This current persists until the stored charge is sufficiently removed to allow the junction to support the voltage by the formation of a depletion layer. This reverse recovery process pertains to a resistive load.

In power electronic circuits, it is commonplace to use power rectifiers with an inductive load. In this case, the current reduces at a constant ramp rate, until the diode is able to support voltage. Consequently, a large peak reverse recovery current (I_{PR}) occurs due to the stored charge followed by the reduction of the current to zero. The power rectifier remains in its forward biased mode with a low on–state voltage drop during part of the current switching, then rapidly increases to the supply voltage with the rectifier operating in reverse bias mode. The current flowing through the rectifier in the reverse direction reaches I_{PR} when the reverse voltage becomes equal to the reverse bias supply voltage.

The simultaneous presence of a high current and voltage produces large instantaneous power dissipation in the power rectifier. The peak reverse recovery current also flows through the power switch that is controlling the switching event increasing the power losses in the transistor. Large reverse recovery currents can trigger latch–up failures that can destroy both the transistor and the rectifier. It is therefore desirable to reduce the magnitude of the peak reverse recovery current and the time duration of the recovery transient. This time duration is referred to as the *reverse recovery time.*

1.1.2. Thyristors

Thyristors were initially developed to replace vacuum valves in power electronics and first reached the market in the early 1960's.

A thyristor basically consists of three series–connected *p-n* junctions. Such a

simple structure leads to a voltage–current characteristics displaying a bi–stable behavior which allows operation both in *blocking regime* with low off–state currents and in a *conduction regime* with low on–state voltages. Thyristors have blocking capability both in forward and reverse bias conditions, which makes them particularly well suited for AC applications.

The device may be triggered to on–state from forward blocking state by applying a suitable gate signal. Once conduction has been triggered, the thyristor remains in a stable on–state condition even with no gate current. Moreover, a thyristor automatically switches to reverse bias blocking state due to change of sign in the voltage in an AC circuit.

Applications of thyristors range from home appliances to electrical energy distribution. For this latter application the current capability of current solid state thyristors has reached $5000A$ while the blocking voltage capability is as high as $8000V$ [5]. Such high ratings are required for HVDC networks [16]. Figure 1.3

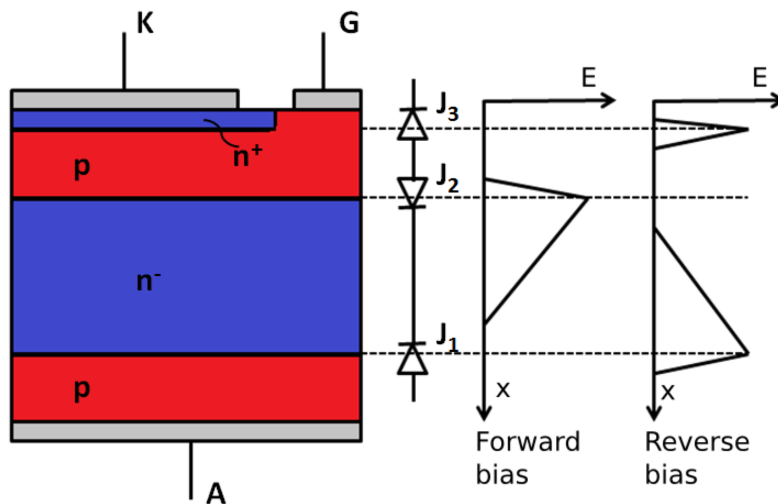

Figure 1.3.: Basic thyristor structure and electric field distribution in forward and reverse bias conditions.

displays schematically the structure of a thyristor; four regions with different doping form three *p*-*n* junctions labeled J_1, J_2 e J_3, respectively. In forward bias the junctions J_1 and J_3 are forward biased, while J_2 is reverse biased. As shown in figure 1.3, in this case, the voltage drop is mainly supported by the charge accumulating in the depleted region around J_2. In reverse biased conditions J_2 is forward biased while J_1 and J_3 are reverse biased. In this latter case most part of the voltage drop is across J_1. A simple model that can be used to understand the behavior of a thyristor consists of two bipolar transistors (one *p*-*n*-*p* and one *n*-*p*-*n*) connected as shown in figure 1.4. Denoting by α_1 and α_2 the current gain

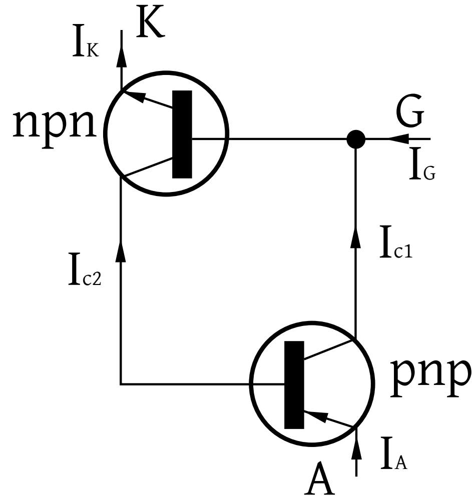

Figure 1.4.: Circuital equivalent of a thyristor

coefficients of the two transistors one can easily write an equation for the current I_{A} at the anode (A). Expressing the currents I_{C1} and I_{C2} as

$$I_{\mathrm{C1}} = \alpha_1 I_{\mathrm{A}} + I_{p0} \tag{1.1}$$

$$I_{\mathrm{C2}} = \alpha_2 I_{\mathrm{K}} + I_{n0} \tag{1.2}$$

one gets

$$I_A = I_{\mathrm{C1}} + I_{\mathrm{C2}} = \alpha_1 I_{\mathrm{A}} + \alpha_2 I_{\mathrm{K}} + I_{p0} + I_{n0} \tag{1.3}$$

where I_{p0} and I_{n0} are diffusion leakage currents of the n^- region and of the p region, respectively.

By balancing the currents flowing into the device one may write

$$I_{\mathrm{K}} = I_{\mathrm{A}} + I_{\mathrm{G}} \tag{1.4}$$

which gives

$$I_{\mathrm{A}} = \alpha_1 I_{\mathrm{A}} + \alpha_2 I_{\mathrm{A}} + \alpha_2 I_{\mathrm{G}} + I_{p0} + I_{n0} \tag{1.5}$$

solving with respect to a I_{A} gives

$$I_{\mathrm{A}} = \frac{\alpha_2 I_{\mathrm{G}} + I_{p0} + I_{n0}}{1 - (\alpha_1 + \alpha_2)}. \tag{1.6}$$

Equation 1.6 is valid as long as avalange multiplication due to impact ionization remains negligible. Anode current tends to infinity if the denominator in 1.6 tends to 0. If $\alpha_1 + \alpha_2 \geq 1$ the thyristor is in conduction and a positive feedback loop is formed in the device.

In forward bias there are two branches in the I–V characteristics: blocking and conducting. When in reverse bias the device can only operate in blocking mode. In both forward bias and reverse bias blocking mode, the maximum attainable voltage value is given by the maximum allowed leakage current.

In both cases there is a threshold blocking voltage beyond which a current blow–up occurs: in reverse bias such threshold is the breakdown voltage V_{bd}, while in forward bias it is the breakover voltage V_{bo}. For forward biases larger than V_{bo} the device turns on and switches to conduction mode. This latter switching event is to be avoided in high–power devices as the resulting large currents may cause severe device damages.

The blocking capability is limited by two phenomena: *breakdown* and *punch–through*. Breakdown has been already discussed in section 1.1.1 while punch–through occurs when, with increasing applied voltage, the space charge extending from the n^- region reaches the adjacent p region. In such occurrence, holes from the p region are forced by electric field and the thyristor switches to a conducting regime.

Assuming piecewise linear electric field in the n^- region and neglecting built–in voltage, the punch–through voltage can be estimated as

$$V_{\mathrm{pt}} = \frac{qN_{\mathrm{D}}w_{\mathrm{B}}^2}{\varepsilon} \tag{1.7}$$

where w_{B} is the length of the n^- region. As N_{D} increases, a trade–off between V_{bd} and V_{pt} occurs at constant w_{B}: V_{pt} increases, while V_{bd} decreases; at constant doping, on the other hand, increasing w_{B} results in increased V_{pt} and V_{bd}.

1.1.3. Numerical simulation for power electronics

From the description of two important classes of power semiconductor devices, we can evince a list of characteristics that need to be satisfied by a tool aimed at their numerical simulations. In particular, it is necessary to deal with:

- highly variable doping densities – and consequently highly variable charge carrier densities with steep boundary or internal layers,
- very high applied voltages, both in conducting and blocking regime,
- high frequencies and fast transients (recoveries), as well as quasi–static (conducting, blocking) regimes,
- very large conducting currents, and large peak switching currents,

- wide range of operation temperatures, and therefore temperature effects on charge transport phenomena,
- effects of semiconductor process technology, like lifetime engineering, used to enhance device performance,
- complex shapes, doping and contacts distributions, and small details in otherwise large devices, requiring full–scale three–dimensional representation,
- controlling and loading by coupled external circuits, comprising time-dependent and possibly nonlinear components.

The framework of models and algorithms presented in this thesis has been built in order to satisfy all of these often much demanding requirements. The relevant mathematical modeling of power devices is presented in part I. Chapter 2 deals with the differential modeling of semiconductor devices, the material properties dependence on doping, temperature, process, and the mathematical properties of the model. Chapter 3 treats the circuital modeling, and some aspects related to the coupling of lumped and distributed models.

The algorithmic aspects are discussed in part II: chapter 4 deals with time discretization, chapter 5 with the solution of nonlinear systems of equations, chapter 6 discusses the discretization of the distributed models, and chapter 7 proposes a specifically tailored strategy for the solution of the linear systems obtained. Finally, part III presents a series of test cases where the proposed algorithms were applied.

References

[1] M. Rahimo, A. Kopta, et al. "The Bi-mode Insulated Gate Transistor (BiGT) A potential technology for higher power applications". In: *Proc. ISPSD09*. 2009, pp. 283–286.

[2] Giuseppe Alì, Andreas Bartel, et al. "Analysis of a PDE thermal element model for electrothermal circuit simulation". In: *Scientific Computing in Electrical Engineering SCEE 2008*. Springer, 2010, pp. 273–280.

[3] B Jayant Baliga. *Fundamentals of power semiconductor devices*. Springer Science & Business Media, 2010.

[4] Massimiliano Culpo, Carlo de Falco, et al. "Automatic thermal network extraction and multiscale electro-thermal simulation". In: *Scientific Computing in Electrical Engineering SCEE 2008*. Springer, 2010, pp. 281–288.

[5] J. Vobecky. "Future trends in high power devices". In: *Microelectronics proceedings (MIEL), 2010 27th International Conference on Microelettrionics* (2010), pp. 67–72.

[6] Christian M. Franck. "HVDC Circuit Breakers: A Review Identifying Future Research Needs". In: *IEEE Transactions on Power Delivery* 26.2 (Apr. 2011).

[7] L. Storasta, M. Rahimo, et al. "The radial layout design concept for the bi-mode insulated gate transistor". In: *Proceedings of ISPSD*. 2011, pp. 56–59.

[8] M. Callavik, A. Blomberg, et al. *The hybrid HVDC breaker*. Tech. Paper. ABB Grid Systems, 2012.

[9] Andreas Bartel, Markus Brunk, et al. "Dynamic iteration for coupled problems of electric circuits and distributed devices". In: *SIAM Journal on Scientific Computing* 35.2 (2013), B315–B335.

[10] A. D. Andersen. "No transition without transmission: HVDC electricity infrastructure as an enabler for renewable energy?" In: *Environmental Innovation and Societal Transitions* 13 (2014), pp. 75–95.

[11] Marco Bellini and Jan Vobecky. "Large-scale 3D TCAD study of the impact of shorts in phase controlled thyristors". In: *Simulation of Semiconductor Processes and Devices (SISPAD), International Conference on*. IEEE. 2014.

[12] Sven Klaka. *Thyristors – The heart of HVDC*. Nov. 2015. URL: `https://www.abb-conversations.com/2015/11/thyristors-the-heart-of-hvdc/` (visited on 12/2015).

[13] Neophytos Lophitis, Marina Antoniou, et al. "Improving Current Controllability in Bi-mode Gate Commutated Thyristors". In: *Electron Devices, IEEE Transactions on* 62.7 (July 2015), pp. 2263–2269. ISSN: 0018-9383. DOI: `10.1109/TED.2015.2428994`.

[14] Daniele Prada, Marco Bellini, et al. "On the Performance of Multiobjective Evolutionary Algorithms in Automatic Parameter Extraction of Power Diodes". In: *Power Electronics, IEEE Transactions on* 30.9 (2015), pp. 4986–4997.

[15] L. Storasta, M. Rahimo, et al. "Optimized Power Semiconductors for the Power Electronics Based HVDC Breaker Application". In: *Proceedings of PCIM Europe 2015*. 2015, pp. 1–7.

[16] J Vobecky, V Botan, et al. "A novel ultra-low loss four inch thyristor for UHVDC". In: *Power Semiconductor Devices & IC's (ISPSD), 2015 IEEE 27th International Symposium on*. IEEE. 2015, pp. 413–416.

[17] J Vobecky, V Botan, et al. "New Low Loss Thyristor for HVDC Transmission". In: *PCIM Europe 2015; International Exhibition and Conference for Power Electronics, Intelligent Motion, Renewable Energy and Energy Management; Proceedings of*. VDE. 2015, pp. 1–6.

[18] Davide Cagnoni, Marco Bellini, et al. "An algorithm for mixed-mode 3D TCAD for power electronics devices, and application to power p-i-n diode". In: *Progress in Industrial Mathematics at ECMI 2014*. Mathematics in Industry. Springer, 2016.

[19] *BIM++*. URL: `http://gitserver.mate.polimi.it/redmine/projects/bim` (visited on 02/01/2016).

[20] *FEMilaro*. URL: http://code.google.com/p/femilaro/ (visited on 02/01/2016).

[21] *Lis: Library of Iterative Solvers for Linear Systems*. URL: http://www.ssisc.org/lis/ (visited on 02/01/2016).

[22] *MUMPS: a MUltifrontal Massively Parallel sparse direct Solver*. URL: http://mumps.enseeiht.fr/ (visited on 02/01/2016).

Part I.

Mathematical and physical models

2. The Drift–Diffusion Model for Charge Transport

In this chapter, we present the full partial differential equations used in this thesis to describe the transport of charge carriers in semiconductors. Section 2.1 derives and describes the system of partial differential equations upon which the drift–diffusion model is based. Section 2.2 introduces models to account for temperature and material properties through the equations coefficients. Section 2.3 introduces the models and assumption we employ when accounting for interaction of the semiconductor device with the external environment. Finally, in section 2.4, we review some analytical results which will be useful when defining the strategy for obtaining a numerical approximation to the problem solution.

2.1. PDE Conservation Laws

In this section, the partial differential model known as *drift–diffusion* equations is obtained, starting from the basic laws of electrodynamics. Only the main differential terms are obtained, while the specific treatment of nonlinear coefficients is delayed to section 2.2.

2.1.1. Poisson's equation

Electrodynamics is mathematically described by Maxwell's equations

$$\nabla\times \vec{H} = q\vec{J} + \frac{\partial \vec{D}}{\partial t}, \tag{2.1a}$$

$$\nabla\times \vec{E} = -\frac{\partial \vec{B}}{\partial t}, \tag{2.1b}$$

$$\nabla\cdot \vec{D} = \rho, \tag{2.1c}$$

$$\nabla\cdot \vec{B} = 0, \tag{2.1d}$$

coupling electric field $\vec{E}$, electric displacement $\vec{D}$, magnetizing field $\vec{H}$ and magnetic induction $\vec{B}$ to current density $q\vec{J}$ and space charge density ρ.

Electric displacement and electric field are related, in isotropic, linear materials, by the constitutive equation

$$\vec{D} = \varepsilon\vec{E}, \tag{2.2}$$

ε being the material dielectric permittivity.

It is in practice useful to express the fields in function of potentials. Let $\vec{A}$ be the vector potential satisfying

$$\vec{B} = \nabla\times\vec{A}, \tag{2.3}$$

$$\nabla\cdot\vec{A} = 0. \tag{2.4}$$

Replacing (2.3) in (2.1b) results in

$$\nabla\times\left(\vec{E} + \frac{\partial\vec{A}}{\partial t}\right) = 0, \tag{2.5}$$

thanks to which the irrotational field $\vec{E} + \frac{\partial\vec{A}}{\partial t}$ can be seen as the gradient of a scalar potential ϕ:

$$\vec{E} = -\frac{\partial\vec{A}}{\partial t} - \nabla\phi. \tag{2.6}$$

Employing then (2.2) and (2.6) to transform (2.1c), one can show that

$$\nabla\cdot\left(\varepsilon\frac{\partial\vec{A}}{\partial t}\right) + \nabla\cdot(\varepsilon\nabla\phi) = -\rho. \tag{2.7}$$

Supposing the studied domain was much smaller than the wavelength of the electromagnetic radiation at the typical frequences involved, quasi–static conditions could be assumed and time derivatives in (2.6) and (2.7) could be neglected. The following equations then rise:

$$\vec{E} = -\nabla\phi \tag{2.8}$$

$$\nabla\cdot(\varepsilon\nabla\phi) = -\rho. \tag{2.9}$$

In semiconductors, as explained in the introductive chapter, the space charge is given by the built–in dopants and the free charge carriers:

$$\rho = q(p - n + N_{\mathrm{D}} - N_{\mathrm{A}}) = q(p - n + N_{\mathrm{bi}}) \tag{2.10}$$

where n and p represent the number density of free electrons and holes, while N_{bi}, the built–in net dopant particles number density, is given by the combination of donors, N_{D} and acceptors, N_{A}.

Subtracting (2.9) expression from (2.10) the form of Poisson's equation we will carry on in the following becomes:

$$-\nabla\cdot(\varepsilon\nabla\phi) = q(p - n + N_{\mathrm{bi}}) \tag{Poisson}$$

2.1.2. Charge transport equations

The conservation of electric charge can be derived from (2.1a), by applying the divergence operator, resulting in the conservation law usually referred to as Kirchoff's current law (KCL):

$$\nabla\cdot\,(\nabla\times\vec{H}) = \nabla\cdot(q\vec{J}) + \frac{\partial\rho}{\partial t} = 0. \tag{2.11}$$

In semiconductors, $\vec{J}$ is made of two contributions, the electron and hole current densities:

$$q\vec{J} = q\vec{J}_p - q\vec{J}_n. \tag{2.12}$$

If time variations in N_{bi} are negligible, namely

$$\frac{\partial(N_{\mathrm{D}} - N_{\mathrm{A}})}{\partial t} = \frac{\partial(N_{\mathrm{bi}})}{\partial t} = 0, \tag{2.13}$$

then (2.11) can be restated as:

$$\nabla\cdot(\vec{J}_p - \vec{J}_n) + \frac{\partial(p-n)}{\partial t} = 0 \tag{2.14}$$

Decomposing the terms in (2.14) with the help of an additional variable R, the two equations

$$\frac{\partial n}{\partial t} + \nabla\cdot\,\vec{J}_n = -R \tag{n-balance}$$
$$\frac{\partial p}{\partial t} + \nabla\cdot\,\vec{J}_p = -R \tag{p-balance}$$

rise, where the right hand side represents the net generation or recombination rate, namely

$$R = R_n - G_n = R_p - G_p. \tag{2.15}$$

2.1.3. The drift–diffusion currents

Current density in a gas of charged particles can be expressed as the product of the elementary charge, the particles number density, and the average particle velocity:

$$\begin{aligned} q\vec{J}_p &= qn\vec{v}_n, \\ q\vec{J}_p &= qp\vec{v}_p. \end{aligned} \tag{2.16}$$

Motion of carriers is defined, over distances much longer than the lattice vectors, by collisions with the lattice itself. As a consequence, the applied force is proportional to the average speed $\vec{v}$, rather than the acceleration:

$$\begin{aligned} \vec{v}_n &= \mu_n\vec{F}_n = \mu_n\nabla\phi_n \\ \vec{v}_p &= \mu_p\vec{F}_p\ = -\mu_p\nabla\phi_p \end{aligned} \tag{2.17}$$

the scalar fields ϕ_n, ϕ_p being the electrochemical or quasi–Fermi potentials for electrons and holes respectively.

In non–degenerate semiconductors, it is usually safe to assume the Maxwell-Boltzmann relation between carrier density, electric and electrochemical potentials:

$$\begin{aligned} \phi_n &= \phi - \phi_{\mathrm{th}} \ln\left(\frac{n}{N_{\mathrm{i}}}\right) \\ \phi_p &= \phi + \phi_{\mathrm{th}} \ln\left(\frac{p}{N_{\mathrm{i}}}\right) \end{aligned} \tag{2.18}$$

where N_{i} is the intrinsic density of free carriers while ϕ_{th} is the thermal voltage $k_{\mathrm{B}}Tq^{-1}$. Replacing (2.18) and (2.17) in (2.16), the following current density definitions can be derived:

$$\vec{J}_n = -\mu_n \phi_{\mathrm{th}} \left(\nabla n - \frac{n}{\phi_{\mathrm{th}}} \nabla \phi\right) \tag{n-current}$$

$$\vec{J}_p = -\mu_p \phi_{\mathrm{th}} \left(\nabla p + \frac{p}{\phi_{\mathrm{th}}} \nabla \phi\right) \tag{p-current}$$

Equations (n-current) and (p-current) work as constitutive relations for (n-balance) and (p-balance); they comprise carrier diffusion terms ∇n, ∇p, and transport or drift terms $-n\nabla\phi$, $p\nabla\phi$, hence the name of the current model.

2.2. Constitutive Relations for System Coefficients

In this section, we describe thoroughly the models for the various physical coefficients appearing in the drift–diffusion model, presented in section 2.1. We will describe in particular the models for the band gap energy and effective intrinsic density in subsection 2.2.1, for the mobility of carriers in subsection 2.2.2, and finally for the different types of carrier generation and recombination in subsection 2.2.3.

In power electronics devices, temperature effects are particularly important due to the high powers being dissipated. The decision hereby taken of limiting the model to deal with uniform, constant temperature as a parameter is due to the necessity of taking a first step, and being able to investigate different regimes in a simpler way, as it happens e.g. in section 9.3. The framework presented in this thesis, however, provides means of including either lumped or distributed temperature models, task we can consider as a future research objective.

2.2.1. Band–gap Narrowing

For an isolated atom, the energy of electrons is limited to discrete values. In a lattice, however, the allowed discrete values cluster to form continuous *energy*

bands, separated by forbidden regions, or *band gaps.* In semiconductors, the Fermi potential lies in one of those gaps, and the nearest energy bands take the name of *conduction band* (N_C) and *valence band* (N_V). The valence band is the highest range of electron energies in which electrons are normally present at absolute zero temperature, while the conduction band is the lowest range of vacant electronic states.

The difference of energy between conduction and valence band is called $q\phi_\mathrm{g}$. Dependence of $q\phi_\mathrm{g}$ on temperature has been experimentally investigated [12] and found to fit the equation

$$q\phi_\mathrm{g} = q\phi_\mathrm{g}(T_{0\,\mathrm{K}}) + \frac{\alpha T^2}{T+\beta} \tag{2.19}$$

where the parameters $q\phi_\mathrm{g}(T_{0\,\mathrm{K}})$, α, β are reported in table 2.1.

The effective density of states in valence and conduction band also depend on temperature, both directly and through the effective carrier masses:

$$\begin{aligned} N_\mathrm{C} &= N_\mathrm{ref}\left(\frac{m_n^*(T)}{m_0}\right)^{\frac{3}{2}}\left(\frac{T}{T_{300\,\mathrm{K}}}\right)^{\frac{3}{2}}, \\ N_\mathrm{V} &= N_\mathrm{ref}\left(\frac{m_p^*(T)}{m_0}\right)^{\frac{3}{2}}\left(\frac{T}{T_{300\,\mathrm{K}}}\right)^{\frac{3}{2}}. \end{aligned} \tag{2.20}$$

Electrons effective mass varies with temperature according to [30]:

$$\frac{m_n^*}{m_0} = a\left(\frac{q\phi_\mathrm{g}(T_{0\,\mathrm{K}})}{q\phi_\mathrm{g}(T)}\right)^{\frac{2}{3}}, \tag{2.21}$$

while holes effective mass follow the relation

$$\frac{m_p^*}{m_0} = \left(\frac{a+bT+cT^2+dT^3+eT^4}{1+fT+gT^2+hT^3+iT^4}\right)^{\frac{2}{3}}. \tag{2.22}$$

The coefficients for both formulas are reported in table 2.2.

The intrinsic carrier density can be expressed in terms of the densities of states and the band gap energy as

$$N_\mathrm{i} = \sqrt{N_\mathrm{V}N_\mathrm{C}}\exp\left(\frac{-q\phi_\mathrm{g}}{2k_\mathrm{B}T}\right). \tag{2.23}$$

A doped but non degenerate semiconductor is such that the doping atoms number density is much smaller than the host semiconductor density. In such cases, doping atoms are sufficiently far away from each other that the respective influence of the exterior orbitals can be neglected. The energy of the dopant atom orbitals

Quantity	Value	Unit
$q\phi_{\mathrm{g}}(T_{0\,\mathrm{K}})$	1.1648	J
α	4.73×10^{-4}	JK^{-1}
β	636	K
N_{ref}	2.541×10^{25}	m^{-3}

Table 2.1.: Parameters for temperature dependence of band gap (2.19), and of effective density of states (2.20)

Quantity	Equation	Value	Unit
a	(2.21)	1.0618	1
a	(2.22)	0.4435870	1
b	(2.22)	0.3609528×10^{-2}	K^{-1}
c	(2.22)	0.1173515×10^{-3}	K^{-2}
d	(2.22)	0.1263218×10^{-5}	K^{-3}
e	(2.22)	0.3025581×10^{-8}	K^{-4}
f	(2.22)	0.4683382×10^{-2}	K^{-1}
g	(2.22)	0.2286895×10^{-3}	K^{-2}
h	(2.22)	0.7469271×10^{-6}	K^{-3}
i	(2.22)	0.1727481×10^{-8}	K^{-4}

Table 2.2.: Parameters for temperature dependence of the effective mass of carriers (2.21), (2.22)

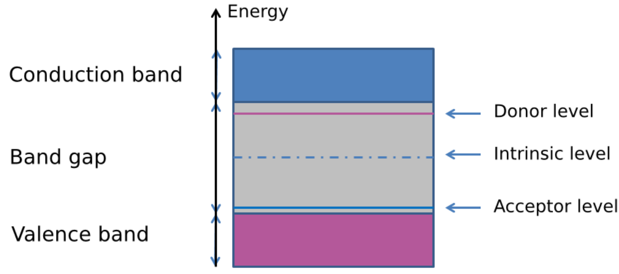

Figure 2.1.: Doped semiconductor band diagram.

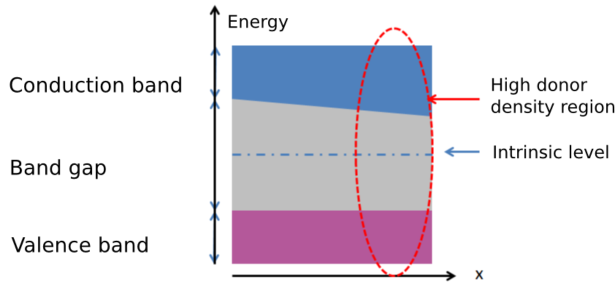

Figure 2.2.: Band gap narrowing for strongly doped regions.

is then a discrete value (equal to the one for an isolated atom) within the band gap (see fig. 2.1).

As the doping concentration grows, and dopant atoms interaction becomes non negligible, the discrete level *thickens* into a continuous energy band, which may merge with the conduction band (n-type doping, see fig. 2.2) or the valence band (p-type doping). This effect can be modeled with the increase of the densities N_{C} or N_{V}, or with an equivalent *narrowing* of the band gap $q\phi_{\mathrm{g}}$.

As per (2.23), a variation $q\phi_{\mathrm{gn}} \leq 0$ in the band gap energy reflects in the effective intrinsic density

$$N_{\mathrm{i,eff}} = \sqrt{N_{\mathrm{V}} N_{\mathrm{C}}} \exp\left(\frac{-(q\phi_{\mathrm{g}} - q\phi_{\mathrm{gn}})}{2k_{\mathrm{B}}T}\right) = N_{\mathrm{i}} \exp\left(\frac{q\phi_{\mathrm{gn}}}{2k_{\mathrm{B}}T}\right) \tag{2.24}$$

The model adopted in this thesis is due to Slotboom [16, 18, 33] and relates $q\phi_{\mathrm{gn}}$ with the total impurities density $N_{\mathrm{t}} = N_{\mathrm{A}} + N_{\mathrm{D}}$ as

Quantity	Value	Unit
E_{ref}	$4,344 \times 10^{16}$	J
N_{ref}	$1,3 \times 10^{23}$	m^{-3}

Table 2.3.: Parameters for Slotboom's band gap narrowing model (2.25)

$$q\phi_{\mathrm{gn}} = E_{\mathrm{ref}} \left[\ln\left(\frac{N_{\mathrm{t}}}{N_{\mathrm{ref}}}\right) + \sqrt{\left(\ln\left(\frac{N_{\mathrm{t}}}{N_{\mathrm{ref}}}\right)\right)^2 + 0.5} \right]. \tag{2.25}$$

Typical values for the reference energy and density in (2.25) are reported in table 2.3.

2.2.2. Charge Density and Electric Field Dependent Mobility

Mobility of a carrier u scales with the particle charge, the mean time interval between collisions τ_u, and with the inverse of the effective carrier mass $m_u^\dagger$:

$$\mu_u = \frac{q\tau_u}{m_u^\dagger}. \tag{2.26}$$

For low doping or carrier concentration, electron and hole mobilities are in a ratio of roughly 3 to 1, as $m_n^\dagger$ is smaller than $m_p^\dagger$. In such state, the interaction between carriers and lattice phonons are the dominant phenomenon affecting carrier motion. When doping or carrier concentration grows, collisions due to Coulomb interaction between carriers and fixed, ionized impurities gain importance, and mobility is further reduced.

The superimpositions of the two phenomena are accounted for with good approximation by means of Matthiessen's rule:

$$\frac{1}{\mu_u} = \frac{1}{\mu_{u,\mathrm{L}}} + \frac{1}{\mu_{u,\mathrm{C}}} \tag{2.27}$$

$\mu_{u,\mathrm{L}}$ and $\mu_{u,\mathrm{C}}$ indicating respectively effects of lattice interactions and Coulomb interactions. The former term is influenced by temperature, since thermal agitation increases the effective radius of particles and therefore the collision probability. For lower temperatures, mobility is higher, but its dependence on doping grows stronger.

A second, important contribution to the carrier mobility is given by the electric field. In fact, the linear ansatz in (2.17) is only good for low electric fields; as the field increases, velocity saturates to a maximum magnitude $|\vec{v}_{u,\max}|$, while mobility decreases, and can be then considered as a nonlinear function of the electric field.

The following treats in more detail the modeling of the different phenomena considered in this thesis.

Effects of interaction with lattice and other charged particles In order to model the mobility dependence from the various kind of interactions to which carrier are subject, we adopted in this thesis the model proposed by Klaassen, also known as the Philips Unified Mobility Model [31, 32], built to consider lattice, acceptors, donors, and free carriers scattering. A detailed description of the model follows, whereas the typically adopted parameters are reported in tables 2.4, 2.5, 2.6, and 2.7.

In Klaassen's framework, lattice interaction assumes the following, temperature dependent trend:

$$\mu_{u,\mathrm{L}} = \mu_{u,\mathrm{max}} \left(\frac{T}{T_{300\,\mathrm{K}}} \right)^{-\theta_u} . \tag{mobL}$$

The Coulomb interaction term comprises all the effects of scattering between carrier u and N_A, N_D, n, p. Each contribution is modeled as a separate mobility, and then all mobilities are recombined in a unique term through Matthiessen's rule:

$$\frac{1}{\mu_{u,\mathrm{C}}} = \frac{1}{\mu_{u,\mathrm{A}}} + \frac{1}{\mu_{u,\mathrm{D}}} + \frac{1}{\mu_{u,n}} + \frac{1}{\mu_{u,p}} \tag{2.28}$$

Expansion of the Matthiessen sum results in the following model

$$\mu_{u,\mathrm{C}} = \left[\mu_{u,\mathrm{N}} \left(\frac{N_{u,\mathrm{ref}}}{N_{u,\mathrm{sc}}} \right)^{\alpha_u} + \mu_{u,\mathrm{c}} \left(\frac{n+p}{N_{u,\mathrm{sc}}} \right) \right] \left(\frac{N_{u,\mathrm{sc}}}{N_{u,\mathrm{sc,eff}}} \right) , \tag{mobC}$$

with the first addendum in square brackets representing the effect of impurities on majority carriers, the second addendum the free carriers interaction, and the correcting factor accounts for screening. Temperature effects are considered according to the following:

$$\mu_{u,N} = \frac{\mu_{u,max}^2}{\mu_{u,max} - \mu_{u,min}} \left(\frac{T}{T_{300\,\mathrm{K}}} \right)^{3\alpha_u - 1,5} , \tag{2.29}$$

$$\mu_{u,c} = \frac{\mu_{u,max}\mu_{u,min}}{\mu_{u,max} - \mu_{u,min}} \left(\frac{T_{300\,\mathrm{K}}}{T} \right)^{0,5} . \tag{2.30}$$

Moreover, the scatterers density $N_{u,\mathrm{sc}}$ is given for electrons and holes respectively by:

$$N_{n,\mathrm{sc}} = N_D^* + N_A^* + p, \tag{2.31}$$

$$N_{p,\mathrm{sc}} = N_A^* + N_D^* + n, \tag{2.32}$$

where donors and acceptors densities are corrected to account for clustering in

Symbol	Value	Unit
a_g	0.89233	1
b_g	0.41372	1
c_g	0.005978	1
α_g	0.28227	1
β_g	0.19778	1
γ_g	0.72169	1
δ_g	1.80618	1

Table 2.4.: Philips unified mobility model: Parameters for (2.37)

ultra–high concentration:

$$N_D^* = N_{D,0} Z_D = N_{D,0}\left[1+\frac{N_{D,0}^2}{c_D N_{D,0}^2 + N_{D,\mathrm{ref}}^2}\right] \tag{2.33}$$

$$N_A^* = N_{A,0} Z_A = N_{A,0}\left[1+\frac{N_{A,0}^2}{c_A N_{A,0}^2 + N_{A,\mathrm{ref}}^2}\right] \tag{2.34}$$

Effective scatterers density in (mobC) is given by:

$$N_{n,\mathrm{sc,eff}} = N_D^* + G(P_n) N_A^* + f_n F(P_n) p, \tag{2.35}$$

$$N_{p,\mathrm{sc,eff}} = N_A^* + G(P_p) N_D^* + f_p F(P_p) n. \tag{2.36}$$

Functions $G(P_i)$ e $F(P_i)$ in (2.35) and (2.36) describe the screening effects due to minority scatterers, and moving scatterers, respectively:

$$G(P_u) = 1 - a_g\left[b_g + \left(\frac{m_0}{m_u^\dagger}\frac{T}{T_{300\,\mathrm{K}}}\right)^{\alpha_g} P_u\right]^{-\beta_g} + c_g\left[\left(\frac{m_u^\dagger}{m_0}\frac{T_{300\,\mathrm{K}}}{T}\right)^{\gamma_g} P_u\right]^{-\delta_g}, \tag{2.37}$$

$$F(P_u) = \left[P_u^{\alpha_f} + d_f - e_f\left(\frac{m_u^\dagger}{m_j^\dagger}\right)\right]\left[a_f P_u^{\alpha_f} + b_f + c_f\left(\frac{m_u^\dagger}{m_j^\dagger}\right)\right]^{-1}, \tag{2.38}$$

$m_u^\dagger$, $m_j^\dagger$ being the effective carrier masses for the two different carriers. The screening parameter P_u includes all temperature effects in (2.38), and is computed with a weighted harmonic mean of the Brooks-Herring [3] and Conwell-Weisskopf [1] models:

$$P_u = \left[\frac{f_{\mathrm{CW}}}{s_{\mathrm{CW}} N_{u,sc}^{-\frac{2}{3}}} + \frac{(n+p)\cdot f_{\mathrm{BH}}}{N_{\mathrm{BH}}}\frac{m_0}{m_u^\dagger}\right]^{-1}\left(\frac{T}{T_{300\,\mathrm{K}}}\right)^2. \tag{2.39}$$

Figure 2.3 shows the electron and hole mobility, computed at varying doping concentrations with the presented model.

Symbol	Value	Unit
a_f	0.7643	1
b_f	2.2999	1
c_f	6.5502	1
d_f	2.3670	1
e_f	-0.8552	1
α_f	0.6478	1

Table 2.5.: Philips unified mobility model: Parameters for (2.38)

Symbol	Electrons	Holes	Unit
μ_{max}	1.414×10^{-1}	4.705×10^{-2}	$\mathrm{m^2V^{-1}s^{-1}}$
μ_{min}	6.85×10^{-3}	4.49×10^{-3}	$\mathrm{m^2V^{-1}s^{-1}}$
θ	2.285	2.247	1
$N_{u,\mathrm{ref}}$	9.2×10^{22}	2.23×10^{23}	$\mathrm{m^{-3}}$
α	0.711	0.719	1

Table 2.6.: Philips unified mobility model: Parameters for (mobL), (mobC)

Symbol	Value	Unit
$\frac{m_n^\dagger}{m_0}$	1	1
$\frac{m_p^\dagger}{m_0}$	1.258	1
f_{CW}	2.459	1
s_{CW}	3.97×10^{17}	$\mathrm{m^{-2}}$
f_{BH}	3.828	1
N_{BH}	1.36×10^{26}	$\mathrm{m^{-3}}$
f_n	1	1
f_p	1	1

Table 2.7.: Philips unified mobility model: Parameters for (2.39)

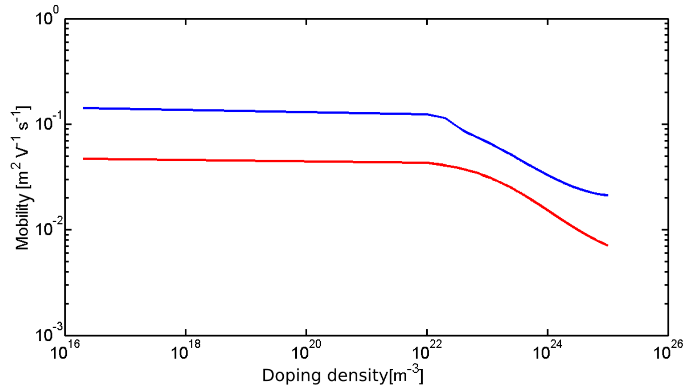

Figure 2.3.: Mobilities vs. doping. Blue line for electrons, red line for holes.

Effects of high electric fields As stated in (2.17), in low electric fields regime, electrons drift velocity is proportional to the electric field through a constant mobility. However, when electric field grows stronger then about $3 \times 10^5\,\mathrm{Vm}^{-1}$, velocity saturates to a maximum: this effect can be modeled as a decrease in mobility for high electric fields. As for the holes, velocity saturates at smaller values, but with slightly higher electric fields. All saturation effects are also slightly influenced by temeperature, according to the model of Canali [13], consisting in the following formulation:

$$\mu_u(|\vec{E}|) = \left[(a+1)\mu_{u,0}\right] \left\{ a + \left[1 + \left(\frac{(a+1)\mu_{u,0}|\vec{E}|}{|\vec{v}_{u,\mathrm{sat}}|} \right)^{\beta} \right]^{\frac{1}{\beta}} \right\}^{-1} \tag{mobE}$$

being $\mu_{u,o}$ the low–fields mobility given in our case by (2.27), while the exponent β partially includes temperature dependence:

$$\beta = \beta_0 \left(\frac{T}{T_{300\,\mathrm{K}}} \right)^{\alpha_\beta} . \tag{2.40}$$

Temperature also influences the saturation velocity, according to:

$$|\vec{v}_{u,\mathrm{sat}}| = |\vec{v}_{u,\max}| \left(\frac{T_{300\,\mathrm{K}}}{T} \right)^{\alpha_{\mathrm{sat}}} . \tag{2.41}$$

Model parameters are reported in table 2.8

2.2.3. Charge Carrier Generation and Recombination

Equations (n-balance) and (p-balance) are closed by the definition of the net recombination rate R. Three main phenomena are responsible for generation or

Symbol	Electrons	Holes	Unit
a	0	0	1
β_0	1.109	1.213	1
α_β	0.66	0.17	1
$\lvert\vec{v}_{u,\max}\rvert$	$1,07 \times 10^5$	$8,37 \times 10^4$	ms^{-1}
α_{sat}	$0,87$	$0,52$	1

Table 2.8.: Parameters for Canali's model (mobE), (2.40), (2.41)

recombination of charge carriers in silicon:

$$R = R^{\mathrm{SRH}} + R^{\mathrm{Au}} + R^{\mathrm{II}} \tag{2.42}$$

where the three contributions stem from trap–assisted recombination, direct recombination, and lattice ionizaton respectively. The three components assume the following form:

$$R^{\mathrm{SRH}} = \frac{pn - N_{\mathrm{i}}^2}{\tau_p(n + N_{\mathrm{i}}) + \tau_n(p + N_{\mathrm{i}})}, \tag{2.43}$$

$$R^{\mathrm{Au}} = (pn - N_{\mathrm{i}}^2)(C_n n + C_p p), \tag{2.44}$$

$$R^{\mathrm{II}} = -\alpha_n|\vec{J}_n| - \alpha_p|\vec{J}_p|. \tag{2.45}$$

The coefficients in (2.43), (2.44), (2.45), with more insight on the involved phenomena, are discussed in the following.

Trap assisted generation and recombination

In indirect band gap materials, such as silicon, trap–assisted recombination provides the main contribution to the net recombination rate. In the following, the Shockley-Read-Hall approach is presented (see [4]). Figure 2.4 drafts trap assisted recombination mechanisms on a band diagram: E_{c} represents conduction band, E_{v} valence band, E_{t} is an intermediate possible energy level called *deep-level trap*, due to the lattice defects. For the sake of simplicity, we assume that all N_{t} traps lie on the same energy level E_{t}. In this setting, several events could occur:

Event 1 E_{t} is empty, and an electron falls from E_{c}:

$$r_1 = \underbrace{N_{\mathrm{t}}[1 - f(E_{\mathrm{t}})]}_{\substack{\text{number of}\\ \text{free defects}}} \cdot \underbrace{n|\vec{v}_{\mathrm{th}}|\sigma_n}_{\substack{\text{capture}\\ \text{rate}}}, \tag{2.46}$$

where $|\vec{v}_{\mathrm{th}}|$ represents thermal velocity, σ_n carriers cross–section, N_{t} the number density of traps, and $f(E)$ the energy levels occupation statistic.

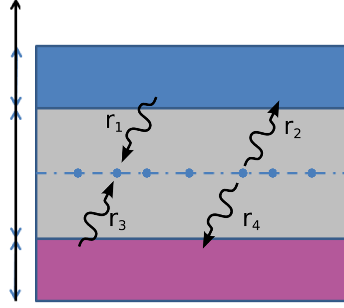

Figure 2.4.: Trap assisted recombination and generation

Event 2 E_t is occupied, and the occupying electron is released in E_c:

$$r_2 = \underbrace{N_\mathrm{t} f(E_\mathrm{t})}_{\substack{\text{number of}\\ \text{occupied}\\ \text{defects}}} \cdot \underbrace{e_n}_{\substack{\text{emission}\\ \text{rate}}} . \tag{2.47}$$

The emission rate e_n can be computed at thermal equilibrium, where $r_1 = r_2$; hence

$$e_n = n_\mathrm{eq} |\vec{v}_\mathrm{th}| \sigma_n \frac{1 - f(E_\mathrm{t})}{f(E_\mathrm{t})}. \tag{2.48}$$

Event 3 E_t is occupied, and the occupying electron is released in E_v (or E_t gains a hole from E_v)

$$r_3 = \underbrace{N_\mathrm{t} f(E_\mathrm{t})}_{\substack{\text{number of}\\ \text{occupied}\\ \text{defects}}} \cdot \underbrace{p |\vec{v}_\mathrm{th}| \sigma_p}_{\substack{\text{capture}\\ \text{rate}}} \tag{2.49}$$

Event 4 E_t is empty, and an electron rises from E_v (or E_t loses a hole to E_v)

$$r_4 = \underbrace{N_\mathrm{t}(1 - f(E_\mathrm{t}))}_{\substack{\text{number of}\\ \text{free defects}}} \cdot \underbrace{e_p}_{\substack{\text{emission}\\ \text{rate}}} \tag{2.50}$$

Once again, e_p is recovered enforcing $r_3 = r_4$ at thermal equilibrium, namely:

$$e_p = p_\mathrm{eq} |\vec{v}_\mathrm{th}| \sigma_p \frac{f(E_\mathrm{t})}{1 - f(E_\mathrm{t})}. \tag{2.51}$$

Symbol	Value	Unit
$\tau_{n,\max}$	1.0×10^{-5}	s
$\tau_{p,\max}$	3.0×10^{-6}	s
$\tau_{u,\min}$	0	s
$N_{u,\text{ref}}$	1×10^{22}	m^{-3}
γ	1	1

Symbol	Value	Unit
$(E_\text{t} - E_\text{i})$	0	J
C	2.55	1
α	1.5	1

Table 2.9.: Shockley-Read-Hall recombination model: Parameters for (2.57) on the left, and for (SRH), (2.59), (2.60) on the right.

In the hypothesis of stationary $f(E)$, $r_1 - r_2 = r_3 - r_4 = R^{\text{SRH}}$. From the first equality, $f(E_\text{t})$ can be computed. Defining carrier lifetimes τ_n and τ_p as

$$\tau_n = \frac{1}{N_\text{t}|\vec{v}_\text{th}|\sigma_n} \quad \text{and} \quad \tau_p = \frac{1}{N_\text{t}|\vec{v}_\text{th}|\sigma_p}, \tag{2.52}$$

the following relation descends:

$$f(E_\text{t}) = \frac{n\tau_n^{-1} + N_\text{t}e_p}{n\tau_n^{-1} + N_\text{t}e_p + p\tau_p^{-1} + N_\text{t}e_p}, \tag{2.53}$$

and then, since multiplying (2.48), (2.51) yelds $N_\text{t}^2 e_p e_n = p_\text{eq} n_\text{eq} \tau_p^{-1} \tau_n^{-1}$, the following holds:

$$R^{\text{SRH}} = \frac{np - N_{\text{i,eff}}^2}{\tau_p\left[n + n_\text{eq}\right] + \tau_n\left[p + p_\text{eq}\right]}. \tag{2.54}$$

An average trap energy E_t can be defined such that

$$n_\text{eq} = N_\text{i,eff} \exp\left(\frac{E_\text{t} - E_\text{i}}{k_\text{B}T}\right) \tag{2.55}$$

$$p_\text{eq} = N_\text{i,eff} \exp\left(\frac{E_\text{i} - E_\text{t}}{k_\text{B}T}\right) \tag{2.56}$$

which in turn yields the following relation, depending on only three paramters $(E_\text{t} - E_\text{i})$, τ_n, and τ_p:

$$R^{\text{SRH}} = \frac{np - N_{\text{i,eff}}^2}{\tau_p\left[n + N_\text{i,eff} \exp\left(\frac{E_\text{t}-E_\text{i}}{k_\text{B}T}\right)\right] + \tau_n\left[p + N_\text{i,eff} \exp\left(\frac{E_\text{i}-E_\text{t}}{k_\text{B}T}\right)\right]}. \tag{SRH}$$

Typical values for the three parameters are reported in table 2.9.

Carrier lifetime models

In (SRH) the carrier lifetimes τ_n and τ_p appear; they represent the characteristic time of energy relaxation of the free carriers. The lifetimes depend strongly on the production technology, and techniques exist to engineer them in order to enhance particular device characteristics. The simulator produced with this thesis allows user definition of space dependent lifetimes which encapsulate process effects. As an alternative, an implementation of Scharfetter's relation between doping and lifetimes is provided:

$$\tau_u(N_\mathrm{A} + N_\mathrm{D}) = \tau_{u,\mathrm{min}} + \frac{\tau_{u,\mathrm{max}} - \tau_{u,\mathrm{min}}}{1 + \left(\dfrac{N_\mathrm{A} + N_\mathrm{D}}{N_{u,\mathrm{ref}}}\right)^\gamma} \tag{2.57}$$

This relation derives from both experimental (e.g. [22]) and theoretical considerations (e.g. [15, 21, 23]).

Temperature dependence of lifetimes also needs o be accounted for: the choice is between two forms of multiplicative correction

$$\tau_u = \tau_u(N_\mathrm{A} + N_\mathrm{D})g(T), \tag{2.58}$$

where g can have a power law form,

$$g(T) = \left(\frac{T}{T_{300\,\mathrm{K}}}\right)^\alpha, \tag{2.59}$$

or an exponential form

$$g(T) = \exp\left(C\frac{T - T_{300\,\mathrm{K}}}{T_{300\,\mathrm{K}}}\right). \tag{2.60}$$

Direct generation and recombination

Auger's direct generation–recombination model considers three–body interaction: two carriers are generated or recombined, while a third particle absorbs or releases the necessary energy. In indirect band gap materials such as silicon, the process is assisted by phonons, which guarantee the momentum conservation in band to band transition. As for the trap–assisted process, we can highlight four possible scenarios:

Event 1 One conduction electron falls to valence band, releasing energy to a second electron in conduction band. Recombination rate is then proportional to the number of conduction band electrons n, to the number of holes p those electrons could fill, and to the number of free electrons n which could acquire the necessary energy:

$$r_1 = C_n n^2 p. \tag{2.61}$$

Event 2 One conduction electron falls to valence band, releasing energy to a hole in valence band. Recombination rate is then proportional to the number of conduction band electrons n, to the number of holes p those electrons could fill, and to the number of holes p which could acquire the necessary energy:

$$r_2 = C_p n p^2. \tag{2.62}$$

Event 3 One electron rises to conduction band, acquiring energy from an excited electron in conduction band. Generation rate is then proportional to the number of valence band electrons N_V, to the number of holes in conduction band N_C those electrons could fill, and to the number of excited electrons n^* in conduction band with sufficient extra energy:

$$r_3 = \hat{C}_n N_\mathrm{C} N_\mathrm{V} n^*. \tag{2.63}$$

As N_V, N_C are constants, we can rearrange r_3 as

$$r_3 = \overline{C}_n n, \tag{2.64}$$

with

$$\overline{C}_n = \hat{C}_n N_\mathrm{C} N_\mathrm{V} \frac{n^*}{n}, \tag{2.65}$$

which is a constant if we suppose stationary energy distribution among conduction electrons, and will come in handy later.

Event 4 One electron rises to conduction band, acquiring energy from an excited hole in valence band. Generation rate is then proportional to the number of valence band electrons N_V, to the number of holes in conduction band N_C those electrons could fill, and to the number of excited holes p^* in valence band with sufficient extra energy:

$$r_4 = \hat{C}_p N_\mathrm{C} N_\mathrm{V} p^*. \tag{2.66}$$

As for r_3, we can rearrange r_4 as

$$r_4 = \overline{C}_p p, \tag{2.67}$$

with

$$\overline{C}_p = \hat{C}_p N_\mathrm{C} N_\mathrm{V} \frac{p^*}{p}. \tag{2.68}$$

Assuming thermal equilibrium, the following holds:

$$r_1 = r_3, \quad \text{and} \quad r_2 = r_4, \tag{2.69}$$

Symbol	Electrons	Holes	Unit
a_u	6.7×10^{-44}	7.2×10^{-44}	$\mathrm{m^6s^{-1}}$
b_u	2.45×10^{-43}	4.5×10^{-45}	$\mathrm{m^6s^{-1}}$
c_u	-2.2×10^{-44}	2.63×10^{-44}	$\mathrm{m^6s^{-1}}$
H_u	3.46667	8.25688	1
N_{ref}	1.0×10^{24}	1.0×10^{24}	$\mathrm{m^{-3}}$

Table 2.10.: Auger generation and recombination: Parameters for (2.72)

or upon substitution

$$\begin{aligned} C_n n_{\mathrm{eq}}^2 p_{\mathrm{eq}} &= \hat{C}_n N_{\mathrm{C}} N_{\mathrm{V}} n^* = \overline{C}_n n_{\mathrm{eq}}; \\ C_p n_{\mathrm{eq}} p_{\mathrm{eq}}^2 &= \hat{C}_p N_{\mathrm{C}} N_{\mathrm{V}} p^* = \overline{C}_p p_{\mathrm{eq}}. \end{aligned} \tag{2.70}$$

Recalling the mass action law $n_{\mathrm{eq}} p_{\mathrm{eq}} = N_{\mathrm{i,eff}}^2$, the relations between $\overline{C}_u$ and C_u reads:

$$\begin{aligned} \overline{C}_n &= C_n N_{\mathrm{i,eff}}^2; \\ \overline{C}_p &= C_p N_{\mathrm{i,eff}}^2. \end{aligned} \tag{2.71}$$

The net rate of generation or recombination will then be expressed as

$$R^{\mathrm{Au}} = r_1 + r_2 - r_3 - r_4 = (C_n n + C_p p)(np - N_{\mathrm{i,eff}}^2). \tag{Auger}$$

The proportionality previously stated holds only roughly, and the coefficients C_u are experimentally fitted in their dependence from carrier density and temperature [19, 17, 20, 35]:

$$C_u = \left[1,0 + H_u exp\left(\frac{-u}{N_{\mathrm{ref}}}\right)\right]\left[a_u + b_u\left(\frac{T}{T_{300\,\mathrm{K}}}\right) + c_u\left(\frac{T}{T_{300\,\mathrm{K}}}\right)^2\right]. \tag{2.72}$$

Parameters for electrons and holes are shown in table 2.10

Impact Ionization

Impact ionization is a non–equilibrium phenomenon, which occurs at high electric fields. Ionization happens whenever a carrier gains enough kinetic energy, between two collisions, to promote a valence electron to conduction band (and generating the corresponding hole) upon collision.

For ionization to occur, a threshold electric field strength needs to be reached, and the space charge region needs to be long enough to allow carriers to reach the necessary kinetic energy. Whenever the space charge region is much longer

Symbol	Electrons	Holes	Electric field	Unit
a_u	7.03×10^7	1.582×10^8	up to 4×10^7	m^{-1}
	7.03×10^7	6.71×10^7	since 4 up to 6×10^7	m^{-1}
b_u	1.231×10^8	2.036×10^8	up to 4×10^7	Vm^{-1}
	1.231×10^8	1.693×10^8	since 4 up to 6×10^7	Vm^{-1}
$\hbar\omega_{op}$	3.932×10^{17}	3.932×10^{17}	-	J

Table 2.11.: Parameters for impact ionization model (2.73), (2.74)

than the mean path between ionizing impacts, an *avalanche* occurs, leading to a breakdown that can be destructive for the device. The ionization coefficients α_u represents the reciprocal of the mean free path between ionizing impacts, and the overall generation rate due to ionization can be expressed as:

$$R^{\mathrm{II}} = \alpha_n n|\vec{v}_n| + \alpha_p p|\vec{v}_p| = \alpha_n|\vec{J}_n| + \alpha_p|\vec{J}_p| \tag{Imp.}$$

Ionization coefficients depend on the carrier's driving force, and can be modeled (according to [10] and based on Chynoweth's relation [5]) as:

$$\alpha_u(F_{u,\mathrm{av}}) = \gamma(T) a_u \exp\left(-\frac{\gamma(T) b_u}{F_{u,\mathrm{av}}}\right), \tag{2.73}$$

where

$$\gamma(T) = \frac{\tanh\left(\frac{\hbar\omega_{op}}{2k_{\mathrm{B}}T_{300\,\mathrm{K}}}\right)}{\tanh\left(\frac{\hbar\omega_{op}}{2k_{\mathrm{B}}T}\right)}, \tag{2.74}$$

while $F_{u,\mathrm{av}}$ is the driving force, which is usually computed as the gradient of the quasi–Fermi potential of the related carrier. Parameters for the model are reported in table 2.11.

2.3. Boundary Conditions

Equations (Poisson), (n-balance)-(p-balance), along with constitutive relations (n-current)-(p-current), (mobL)-(mobC)-(mobE), (SRH)-(Auger)-(Imp.), provide what is usually denoted as drift–diffusion model [2, 25, 37], most commonly used in modeling transport of electrical charge in low–frequency, low–field semiconductor devices:

$$\begin{cases} -\nabla\cdot(\varepsilon\nabla\phi) + q\left(n - p - N_{\mathrm{D}} + N_{\mathrm{A}}\right) = 0 & \text{in } \Omega\times[0,T] \\ \frac{\partial n}{\partial t} - \nabla\cdot\Big(\mu_n\left(\phi_{\mathrm{th}}\nabla n - n\nabla\phi\right)\Big) + R = 0 & \text{in } \Omega\times[0,T] \\ \frac{\partial p}{\partial t} - \nabla\cdot\Big(\mu_p\left(\phi_{\mathrm{th}}\nabla p + p\nabla\phi\right)\Big) + R = 0 & \text{in } \Omega\times[0,T] \end{cases} \tag{Drift–Diffusion}$$

Two of the partial differential equations in (Drift–Diffusion) are diffusion–advection–reaction parabolic equation, while the third is an elliptic PDE. Boundary conditions are necessary to close the system, and they will be treated in the following sections.

The domain $\Omega \subset \mathbb{R}^n$ represents the device geometry. In some simple situations, it can be sufficient to take $n = 1, 2$, however for most devices of interest in this thesis this is not possible, and setting $n = 3$ cannot be avoided, even if some symmetry can be exploited to reduce the domain to only part of the whole device. Some physical effects or numerical behaviors, however, can still be studied in simplified settings, and then considered in the full–scale, 3D case.

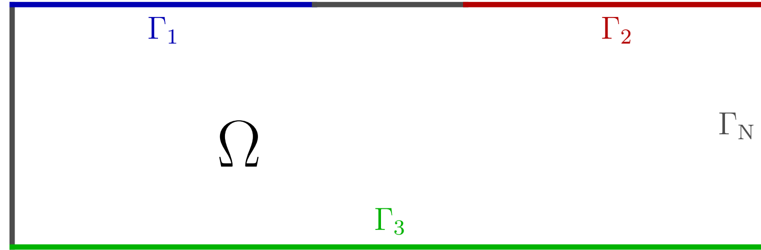

Figure 2.5.: Physical and artificial boundaries in a typical domain geometry

In fig. 2.5 the typical setup of a domain is shown, where the boundary of Ω, $\partial\Omega$, is decomposed in two subsets:

$$\partial\Omega = \Gamma_{\mathrm{D}} \cup \Gamma_{\mathrm{N}} \tag{2.75}$$

where Γ_{N} represents insulated boundaries or symmetry planes, while Γ_{D} represents the physical interface with the controlling circuit, and is itself decomposed in disjoint subsets Γ_k called *contacts*.

If the boundary conditions on Γ_{N} are usually of homogeneous Neumann type, indicating absence of normal flux for symmetry or insulation reasons, the choice of boundary conditions on Γ_{D} is subject to modeling, as normally only one integral quantity for each contact is known and controlled (e.g. voltage, or current). The model used reflects material properties, and some assumptions made in the interface modeling.

2.3.1. Ohmic contacts

The most common ways to model heterojunctions between metals and semiconductors are the ohmic contact model and the Schottky contact model. The former, which we will use throughout this thesis, is better suited to model strongly doped semiconductors joint with metal contacts, while the latter models intrinsic semiconductor–metal heterojunctions.

The ohmic contact model consists in enforcement of the following conditions:

- the surface of the metallic contact - and therefore of the junction - has uniform Fermi potential,
- silicon near the contact is at thermal equilibrium - excess carriers are absorbed by the metal,
- net space charge vanishes.

Two approaches are possible for enforcing those conditions. The first, assuming Maxwell-Boltzmann relations to hold, is to enforce equilibrium by replacing both ϕ_n and ϕ_p with imposed Fermi potential, indicated by F. The resulting nonlinear Dirichlet conditions for electron and hole densities:

$$n = N_\mathrm{i} \exp\left(\frac{F-\phi}{\phi_\mathrm{th}}\right), \tag{2.76}$$

$$p = N_\mathrm{i} \exp\left(\frac{\phi-F}{\phi_\mathrm{th}}\right), \tag{2.77}$$

and then in imposing charge neutrality through a (nonlinear and implicit) Dirichlet condition for Poisson's equation:

$$N_\mathrm{i}\left[\exp\left(\frac{F-\phi}{\phi_\mathrm{th}}\right) - \exp\left(\frac{\phi-F}{\phi_\mathrm{th}}\right)\right] = N_\mathrm{bi}. \tag{2.78}$$

A second way to enforce thermal equilibrium is through mass action law:

$$np - N_\mathrm{i}^2 = 0, \tag{2.79}$$

which can be coupled with the explicit imposition of charge neutrality:

$$n - p = N_\mathrm{bi}, \tag{2.80}$$

and upon some manipulation become

$$n = \frac{N_\mathrm{bi} \pm \sqrt{N_\mathrm{bi}^2 + 4N_\mathrm{i}^2}}{2}, \tag{2.81}$$

$$p = \frac{-N_\mathrm{bi} \pm \sqrt{N_\mathrm{bi}^2 + 4N_\mathrm{i}^2}}{2}, \tag{2.82}$$

the choice on the sign at the denominator being the obvious one that make the result positive, the sign of N_bi given. The condition for Poisson's equation can in this case be recovered by enforcing either (2.76) or (2.77), which taken in explicit form, read:

$$\begin{aligned} \phi &= F + \underbrace{\phi_\mathrm{th} \ln\left(\frac{N_\mathrm{i}}{n}\right)}_{\phi_\mathrm{bi}}, \\ \phi &= F + \overbrace{\phi_\mathrm{th} \ln\left(\frac{p}{N_\mathrm{i}}\right)}, \end{aligned} \tag{2.83}$$

where the built–in voltage ϕ_{bi}, with value independent from the definition and constant over time, actually depends only on the ratio $\frac{N_{\mathrm{bi}}}{N_{\mathrm{i}}}$.

The former approach is more general and could be easily adapted whenever the Maxwell-Boltzmann statistic should not be valid, simply substituting the correct statistic $f(\phi, \phi_u = F)$ in its place in (2.76), (2.77), (2.78). The latter approach sensibly simplifies the form of boundary conditions, and it is our method of choice. Unfortunately, it is particularly prone to numerical round–off errors for the computing of minority carrier density at the boundary, as the relative difference in magnitude of the two addenda in (2.81), (2.82) is very small. It is however possible to recover the minority carrier concentration without incurring in roundoff errors by exploiting the mass action law:

$$n = \begin{cases} \frac{N_{\mathrm{bi}}+\sqrt{N_{\mathrm{bi}}^2+4N_{\mathrm{i}}^2}}{2}, & N_{\mathrm{bi}} \geq 0 \\ \frac{2N_{\mathrm{i}}^2}{-N_{\mathrm{bi}}+\sqrt{N_{\mathrm{bi}}^2+4N_{\mathrm{i}}^2}}, & N_{\mathrm{bi}} < 0, \end{cases} \tag{n-bcs}$$

$$p = \begin{cases} \frac{-N_{\mathrm{bi}}+\sqrt{N_{\mathrm{bi}}^2+4N_{\mathrm{i}}^2}}{2}, & N_{\mathrm{bi}} \leq 0 \\ \frac{2N_{\mathrm{i}}^2}{N_{\mathrm{bi}}+\sqrt{N_{\mathrm{bi}}^2+4N_{\mathrm{i}}^2}}, & N_{\mathrm{bi}} > 0 \end{cases} \tag{p-bcs}$$

$$\phi = F + \phi_{\mathrm{bi}}. \tag{ϕ-bcs}$$

2.3.2. Contact currents

When analyzing semiconductor devices through the drift–diffusion model, integral quantities of interest are the currents flowing through the device contacts, especially since when coupling to an external circuit, it takes part in the global charge balance introduced later in section 3.1.

Customarily, we will always considered positive currents to be entering the device. With such convention, we can define the total current through contact Γ_k as:

$$I_k = -q\int_{\Gamma_k} \left(\vec{J}_p - \vec{J}_n\right) \cdot \vec{\nu}\,\mathrm{d}\gamma + \int_{\Gamma_k} \left(\varepsilon\frac{\partial(\nabla\phi)}{\partial t}\right) \cdot \vec{\nu}\,\mathrm{d}\gamma \tag{k-current}$$

$\vec{\nu}$ being the outward normal vector on the boundary $\delta\Omega$. The first addendum in (k-current) amounts to the conduction current, while the second indicates displacement current.

As far as computing currents trough Neumann boundaries, one should notice how the definition of (k-current) is a linear combination of current densities - which are imposed to vanish on Γ_{N} - and the time derivative of the electric displacement - which is constantly null.

2.4. Conditioning of the Drift–Diffusion System

In this section, we review some results on the drift diffusion system, which will be used later on to justify the choice of the algorithms. The results on conditioning are proved in [29].

2.4.1. Non–dimensional Form and Scaling

The physical quantities in system (Drift–Diffusion) have different physical dimensions and, in order to compare their orders of magnitude, these quantities have to be made dimensionless first by appropriate scalings. Following [48], we introduce for the DD system two closely related scalings, and we shall refer to these scalings as the De Mari and the Unit scalings.

1. De Mari scaling (see [6, 7, 8]):
   - Potentials scaled by ϕ_{th};
   - Concentrations scaled by the intrinsic concentration N_{i};
   - Length scaled by a characteristic Debye length $L_{\mathrm{D}} = \sqrt{\frac{\varepsilon\phi_{\mathrm{th}}}{qN_{\mathrm{i}}}}$,
2. Unit scaling (see [24, 25]):
   - Potentials scaled by ϕ_{th};
   - Concentrations scaled by $N_{\mathrm{bi}}^* = \sup_{x\in\Omega} |N_{\mathrm{bi}}(x)|$;
   - Length scaled by a characteristic device dimension l.

After any of the above scalings, the scaled dimensionless DD system reads

$$\begin{cases} -\nabla\cdot(\lambda^2\nabla\phi) + (n - p - N_{\mathrm{bi}}) = 0 & \text{in } \Omega\times[0,T] \\ \frac{\partial n}{\partial t} - \nabla\cdot\big(\mu_n(\nabla n - n\nabla\phi)\big) + R = 0 & \text{in } \Omega\times[0,T] \\ \frac{\partial p}{\partial t} - \nabla\cdot\big(\mu_p(\nabla p + p\nabla\phi)\big) + R = 0 & \text{in } \Omega\times[0,T] \end{cases} \tag{2.84}$$

where for simplicity we used the same unscaled symbols for the variables, the mobility and doping coefficients and the reaction term. For either scaling we have

$$\lambda^2 = \frac{\varepsilon\phi_{\mathrm{th}}}{qL^2C}, \quad L = L_{\mathrm{D}} \text{ or } l, \quad C = N_{\mathrm{i}} \text{ or } N_{\mathrm{bi}}^*, \tag{2.85}$$

while the thermal voltage disappears in the drift–diffusion term scales to unity. Table 2.12 reports the values used; as unit scaling actually depends on the single problem instance, some ranges for the typical power electronics problem are provided.

In the case of the De Mari scaling $\lambda^2 = 1$, whereas in the case of the Unit scaling, $\lambda^2 \ll 1$, while all the concentrations are expected to be maximally of order 1. The

scaled Debye length λ acts thus as a singular perturbation parameter; the behavior of the solution of (Drift–Diffusion) as $\lambda \to 0^+$ is called *quasi neutral limit*, and has been studied for the transient case e.g. in [28, 27, 44, 43, 42].

Scaling can be represented as the chaining of two operators: the row scaling $\mathcal{R}$, applied externally, and the column scaling $\mathcal{C}$, applied directly on the unknowns:

$$\mathcal{R}F(\mathcal{C}\mathbf{r}) \tag{2.86}$$

with:

- $\mathbf{r}$ representing the abstract vector of *nondimensional* unknowns $\begin{bmatrix}\phi & n & p\end{bmatrix}^T$
- F representing the drift–diffusion operator (Drift–Diffusion)
- the row and column scaling operators reading for the Unit scaling:

$$\mathcal{R} = \begin{bmatrix} qN^*_{\mathrm{bi}}l^{-2} & 0 & 0 \\ 0 & \phi_{\mathrm{th}}\mu_0 l^{-2} & 0 \\ 0 & 0 & \phi_{\mathrm{th}}\mu_0 l^{-2} \end{bmatrix}^{-1} \qquad \mathcal{C} = \begin{bmatrix} \phi_{\mathrm{th}} & 0 & 0 \\ 0 & N^*_{\mathrm{bi}} & 0 \\ 0 & 0 & N^*_{\mathrm{bi}} \end{bmatrix}. \tag{2.87}$$

Table 2.12.: De Mari and Unit scaling factors

Quantity	De Mari factor	value ($T = 300\,\mathrm{K}$)	Unit factor	value ($T = 300\,\mathrm{K}$)
ϕ	ϕ_{th}	$2.585 \times 10^{-2}\,\mathrm{V}$	ϕ_{th}	$2.585 \times 10^{-2}\,\mathrm{V}$
n, p	N_{i}	$1.482 \times 10^{16}\,\mathrm{m}^{-3}$	N^*_{bi}	$10^{25\pm1}\,\mathrm{m}^{-3}$
x	L_{D}	$3.357 \times 10^{-6}\,\mathrm{m}$	l	$10^{-3\pm1}\,\mathrm{m}$
μ_n, μ_p	$D_0\phi_{\mathrm{th}}^{-1}$	$3.868 \times 10^{-3}\,\mathrm{m}^2\mathrm{V}^{-1}\mathrm{s}^{-1}$	μ_0	$1 \times 10^{-1}\,\mathrm{m}^2\mathrm{V}^{-1}\mathrm{s}^{-1}$
D_n, D_p	D_0	$1 \times 10^{-4}\,\mathrm{m}^2\mathrm{s}^{-1}$	$\mu_0\phi_{\mathrm{th}}$	$2.585 \times 10^{-3}\,\mathrm{m}^2\mathrm{s}^{-1}$
$\vec{J}_n, \vec{J}_p$	$D_0N_{\mathrm{i}}L_{\mathrm{D}}^{-1}$	$4.415 \times 10^{17}\,\mathrm{m}^{-2}\mathrm{s}^{-1}$	$\phi_{\mathrm{th}}\mu_0N^*_{\mathrm{bi}}l^{-1}$	$2.585 \times 10^{25\pm2}\,\mathrm{m}^{-2}\mathrm{s}^{-1}$
R	$D_0N_{\mathrm{i}}L_{\mathrm{D}}^{-2}$	$1.314 \times 10^{23}\,\mathrm{m}^{-3}\mathrm{s}^{-1}$	$\phi_{\mathrm{th}}\mu_0N^*_{\mathrm{bi}}l^{-2}$	$2.585 \times 10^{30\pm3}\,\mathrm{m}^{-3}\mathrm{s}^{-1}$
t	$L_{\mathrm{D}}^2D_0^{-1}$	$1.127 \times 10^{-7}\mathrm{s}$	$l^2\phi_{\mathrm{th}}^{-1}\mu^{-1}$	$3.868 \times 10^{-4\pm2}\,\mathrm{s}$

2.4.2. Conditioning Analysis

Following [29], we will outline in this subsection a conditioning analysis for the linearized version of (2.84), which is the one actually solved when employing Newton's or Newton–like methods.

The operator Jacobian, in non–dimensional version, reads:

$$\mathcal{J} = \begin{bmatrix} -\nabla\cdot(\lambda^2\nabla\bullet) & \bullet & -\bullet \\ \nabla\cdot(\mu_n n\nabla\bullet) & \partial_t\bullet - \nabla\cdot(\mu_n(\nabla\bullet - \bullet\nabla\phi)) + R_n\bullet & R_p\bullet \\ -\nabla\cdot(\mu_p p\nabla\bullet) & R_n\bullet & \partial_t\bullet - \nabla\cdot(\mu_p(\nabla\bullet + \bullet\nabla\phi)) + R_p\bullet \end{bmatrix} \tag{2.88}$$

where the bullet is a placeholder, ∂_t denotes the time derivative, and R_n, R_p are the Fréchet derivatives of R with respect to n, p. The leading, second order terms have a non–diagonal stencil,

$$\begin{bmatrix} -\lambda^2\Delta & 0 & 0 \\ \mu_n n\Delta & -\mu_n\Delta & 0 \\ -\mu_p p\Delta & 0 & -\mu_p\Delta \end{bmatrix} \tag{2.89}$$

which can be avoided in different ways. One of them is the switch to quasi–Fermi potential formulation, but also the linear transformation

$$\tilde{\mathcal{J}} = \mathcal{J}\mathcal{T} = \mathcal{J}\begin{bmatrix} 1 & 0 & 0 \\ n & 1 & 0 \\ -p & 0 & 1 \end{bmatrix} \tag{2.90}$$

can change the first column of $\mathcal{J}$ in

$$\begin{bmatrix} -\nabla\cdot(\lambda^2\nabla\bullet) - (n+p)\bullet \\ \partial_t\bullet + \nabla\cdot(\mu_n n\nabla\phi\bullet) + (R_n n + R_p p)\bullet \\ \partial_t\bullet + \nabla\cdot(\mu_p p\nabla\phi\bullet) + (R_n n + R_p p)\bullet \end{bmatrix} \tag{2.91}$$

thus diagonalizing the second order part:

$$\begin{bmatrix} -\lambda^2\Delta & 0 & 0 \\ 0 & -\mu_n\Delta & 0 \\ 0 & 0 & -\mu_p\Delta \end{bmatrix}. \tag{2.92}$$

The operator $\mathcal{T}$ is well conditioned, as $\|\mathcal{T}\|_{L^\infty} = \|\mathcal{T}^{-1}\|_{L^\infty} = \max(1+\|n\|_{L^\infty}, 1+\|p\|_{L^\infty})$ which amounts to roughly 2 in the case of unit scaling.

A *regularization* of Poisson's equation takes place in $\tilde{\mathcal{J}}$, in that $-\lambda^2\Delta$ is replaced by $(-\lambda^2\Delta + n + p)$, making the transformed operator nonsingular when $\lambda = 0$. Moreover, the diagonalization of leading term allows for decoupled conditioning analysis, unless the lower order terms become extremely large.

We will summarize hereafter the results of [29], to which we refer for demonstration, regarding the decoupled conditioning analysis. These result are valid for the steady–state equations and obtained neglecting the reaction terms. However, they provide useful insights also for more general regimes.

The first, linearized equation reads

$$\begin{cases} -\lambda^2\Delta u + (n+p)u = f, \\ u|_{\Gamma_\mathrm{D}} = 0, \qquad \frac{\partial u}{\partial \vec{\nu}}|_{\Gamma_\mathrm{N}} = 0, \end{cases} \tag{2.93}$$

and by means of the maximum principle, for its solution u holds the following bound:

$$\|u\|_{L^\infty} \leq \left\| \frac{f}{n+p} \right\|_{L^\infty} \tag{2.94}$$

which results in (2.93) being well–conditioned.

The second linearized equation (and the same can be applied to the third) can be cast in self–adjoint form:

$$\begin{cases} -\nabla\cdot\delta^2\mu e^{\phi}\nabla w = g \\ w|_{\Gamma_\mathrm{D}} = 0, \qquad \frac{\partial w}{\partial \vec{\nu}}|_{\Gamma_\mathrm{N}} = 0, \end{cases} \tag{2.95}$$

through the transformation from the original variable u to w given by:

$$u = \delta^2 e^{\pm\phi} w, \tag{2.96}$$

where δ^2 is the ratio between N_i and N^*_bi.

For (2.95), it holds for the maximum principle

$$\|w\|_{L^\infty} \leq K(\Omega,\mu)\delta^{-2}e^{-\phi_\mathrm{min}}\|g\|_{L^\infty}, \tag{2.97}$$

which turning back to u leads to:

$$\|u\|_{L^\infty} \leq K(\Omega,\mu)e^{\phi_\mathrm{max}-\phi_\mathrm{min}}\|g\|_{L^\infty}, \tag{2.98}$$

meaning the conditioning in equilibrium condition scales with δ^{-4}, as can be seen by replacing $\phi_\mathrm{max} - \phi_\mathrm{min} \simeq 2\phi_\mathrm{bi}$ according to the definition in section 2.3.1. The bound is not sharp for devices where all regions defined by junctions are connected to a contact; should this occur, it can be shown that the conditioning is independent of δ^2 instead.

3. Lumped–Element Electrical Circuits

Power device testing and simulation is aimed at the investigation of the device response and behavior during usage. Therefore, it is performed in settings suited to reproduce realistic usage conditions, which are emulated by means of a controlling electric circuit, comprising static and dynamic, linear and nonlinear components, and which provide the dynamic boundary conditions needed to our system.

This chapter aims to describe the framework we use to model the behavior of electric circuits (section 3.1) and to investigate the general form of the lumped model, in order to find analogies which allow for a similar treatment of distributed models, and their coupling with circuital elements (section 3.2). After that, (section 3.3) some analytical results with respect to the coupling of distributed and lumped circuital elements are reported.

3.1. Modified Nodal Analysis

The choice for circuit modeling method in this thesis fell on Modified Nodal Analysis (MNA), a technique based on network–level charge conservation laws, which maintains the possibility of an element–by–element assembly of the overall system. Such characteristic seems not crucial at first stance, given the not excessive complexity of the circuits involved. However, the elemental approach - along with the possibility to *reduce* the continuous model - will be exploited in full when special algorithms to treat big simulation will be required.

In the following, the MNA technique is outlined on lumped–elements circuital models, the differential–algebraic equations stemming from MNA are classified, and finally proper coupling of distributed device and circuit is presented in a framework apt to exploit the structural similarities with standard, lumped–element MNA.

3.1.1. Network–level conservation laws

As stated in section 2.1.2 from a purely electrical point of view, the circuit behavior is governed by *Kirchhoff's current law*, that stands at the base of all the most important modeling paradigms is the balance of electrical currents.

At the continuous level, KCL states that the rate of loss of charge ρ within a given volume Ω is equal to the current $\vec{J}$ flowing out of the surface enclosing it,

which in integral formulation reads:

$$-\int_{\Omega} \frac{\partial \rho}{\partial t} d\mathbf{x} = \int_{\partial\Omega} \vec{J}\mathbf{n}\, d\gamma = \int_{\Omega} \mathrm{div}(\vec{J}) d\mathbf{x}. \qquad \text{(2.11, integral)}$$

Equation 2.11 is a general principle, but its multidimensional character exceeds in details the requirements for the formulation of KCL in network–level circuit analysis. In this case, the common approach is to neglect the spatial extension of physical devices and of their interconnections, providing the possibility to represent a physical circuit with a network (called *schematic*) of discrete components (*elements*) connected at certain points (*nodes*). Since each element is possibly connected to $k \geq 2$ nodes (k*–pins element*), the network can be viewed as an hypergraph, elements being the hyperedges connecting the nodes of the hypergraph. With each element, a k-dimensional current vector $\mathbf{i}$ can be associated.

In the following a conventional direction is fixed for the components of $\mathbf{i}$ in such a way that they leave the external pins and enter the element (as shown in 3.1). Notice that due to 2.11 these components are not independent, as their algebraic

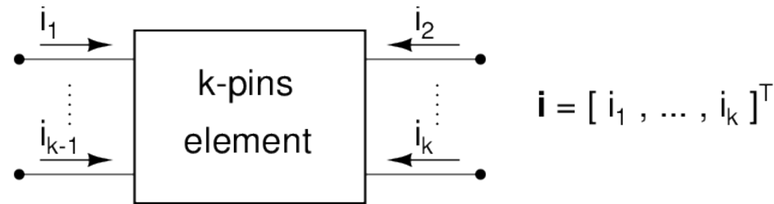

Figure 3.1.: Generic k–pins element. The components of the associated current vector are oriented so that they leave the external pins and enter the element.

sum must be zero to ensure charge conservation, that is to say:

$$\mathbf{1}^T\mathbf{i} = 0 \ , \qquad (3.1)$$

where $\mathbf{1} \in \mathbb{R}^k$ is a vector with only unit entries. A more thorough treatment of these assumptions and its implications can be found in [26]. For the purpose of this thesis, this conceptual simplifications lead to the usual nodal formulation of KCL, which constitutes the core of most circuit simulation algorithms:

The algebraic sum of currents flowing away from any given node is zero.

If a circuit schematic composed of M elements and $N+1$ nodes is being considered, it can be noticed that The KCL statement determines a set of $N+1$ relations. Anyhow, only N of these relations result to be linearly independent, and therefore a node is usually taken as reference (*ground node*) and omitted when deriving the set of balance equations to be used as a base for a mathematical model.

Numbering the nodes from 0 (the ground node) to N and assuming the m–th element of a circuit schematic to be a k–pins element, a $N \times k$ local *incidence matrix* A_m can be defined as:

$$[A_m]_{ij} = a_{ij} = \begin{cases} 1, & \text{if the } j\text{–th component of } \mathbf{i}_m \\ & \text{leaves node } i \in [1, .., N], \\ 0, & \text{otherwise.} \end{cases} \tag{3.2}$$

each matrix being associated with the m–th element itself. The ground node is left out of this computation, as the relative current balance is automatically satisfied, but is generally reported when describing the schematics. Incidence matrix are most practical in mathematically formalizing the network–level KCL, which become:

$$\sum_{m=1}^{M} A_m \mathbf{i}_m = 0. \tag{3.3}$$

The definition of incidence matrices as presented in (3.2) differ from the one usually employed in network theory, whose definition is dictated by the assumption for each k–pins element to be properly represented by an equivalent circuit (*companion model*) built upon 2–pins ideal devices. If this is the case, after the substitution of each circuit element with the corresponding companion model, a unique graph is derived from the initial schematic permitting the description of KCL in terms of *branch currents*. Nevertheless, this graph–based formalism has its main drawback in the fact that it does not allow for simple extensions when elements may not be properly described by lumped networks, which is exactly the case in 3D mixed–mode simulation.

Furthermore, considering branches as basic entities, this formalism results to be inherently based on a *flattened netlist* (i.e. on the equivalent circuit obtained *after* the substitution of physical devices with their companion models) and loses therefore the assembly–by–element structure typical of actual realization of MNA. The system in (3.3) needs to be integrated with constitutive relations, in order to complete the derivation of a closed system of equations describing the purely electrical behavior of a given circuit, as it will be shown later in 3.1.2.

The modular form that 3.3 takes thanks to the use of incidence matrices is of high importance in practice, as it allows for the assembly system of balance equations through *element–by–element inspection*. At the implementation level this consideration grants the possibility to keep the elemental constitutive relations separated from system assembly; particular practical advantages arise when adding new device models to an existing set, existing no need to affect the overall algorithm.

Attempts to run mixed–mode simulations, where both lumped and continuous element models are present, can take much advantage from this structural property, which also allows to extend with ease to the treatment of non–electrical phenomena

(e.g., thermal [51, 52] or magnetic effects[53, 49]). Any attempt to extend a purely circuital description to other physical effects should therefore take this simple but essential structure into account, if it aims to be effectively usable in an industrial environment.

3.1.2. Standard device models and MNA

A constitutive relation for an electrical device is by definition the relation between currents through an element and voltage drops across it. When companion models are used in place of more complex devices [36, 34], the component typologies appearing in a circuit can be reduced to:

1. resistors,
2. capacitors,
3. current sources,
4. inductors,
5. voltage sources,

so that only the constitutive relations of this restricted set of elements are needed to properly describe the electrical behavior of most circuits. Resistors, capacitors and current sources are *voltage controlled* elements, i.e. their current vectors can be expressed as a function of their voltage drops:

$$\mathbf{i}_{\mathrm{C}} = \frac{\mathrm{d}q}{\mathrm{d}t}, \tag{3.4a}$$

$$\text{with } q = q(v_{\mathrm{C}}, t), \tag{3.4b}$$

$$\mathbf{i}_{\mathrm{R}} = r(v_{\mathrm{R}}, t), \tag{3.4c}$$

$$\mathbf{i}_{\mathrm{I}} = i(v_{\mathrm{I}}, \dot{\mathbf{q}}, \mathbf{i}_{\mathrm{L}}, \mathbf{i}_{\mathrm{V}}, t), \tag{3.4d}$$

while inductors and voltage sources are *current controlled* elements, i.e. their voltage drops can be expressed as a function of their currents:

$$v_{\mathrm{L}} = \frac{\mathrm{d}\psi}{\mathrm{d}t}, \tag{3.5a}$$

$$\text{with } \psi = \psi(\mathbf{i}_{\mathrm{L}}, t), \tag{3.5b}$$

$$v_{\mathrm{V}} = v(\mathbf{e}, \dot{\mathbf{q}}, \mathbf{i}_{\mathrm{L}}, \mathbf{i}_{\mathrm{V}}, t). \tag{3.5c}$$

In both 3.4 and 3.5, arguments of the voltage and current source constitutive relations comprise quantities which possibly refer to other elements (*controlled sources*). For more details about these basic components, the interested reader is referred to [14, 26].

Notice that the voltage drops can be easily computed for 2–pins devices by means of the defined incidence matrices. Given the vector of node potentials $\mathbf{e} \in \mathbb{R}^N$, by left multiplication with the incidence matrices A_m^T, gives the vectors of pin voltages:

$$\mathbf{v}_m = A_m^T \mathbf{e}, \quad \forall m \in [1, .., M]. \tag{3.6}$$

from which the voltage drop is recovered by further multiplication by $\begin{bmatrix}-1 & 1\end{bmatrix}$.[1] When a device is connected to ground, (3.2) assures the respective component of $\mathbf{v}_m$ is set to zero. Classical directed incidence matrices for 2–pins elements can then be defined as

$$A_m^* = A_m \begin{bmatrix}-1 \\ 1\end{bmatrix}, \tag{3.7}$$

and express the direct relation between node voltages and voltage drops:

$$v_m = \begin{bmatrix}-1 & 1\end{bmatrix} \mathbf{v}_m = A_m^{*T} \mathbf{e}, \quad \forall m \in [1, .., M]. \tag{3.8}$$

The concept of voltage drops can also be generalized to companion models as a block by assembling the respective directed incidence matrix looping through the internal nodes. This amounts to extending (3.7) as

$$A_{\mathrm{cm}}^* = A_{\mathrm{cm}} \begin{bmatrix}-1 & \cdots & -1 \\ 1 & \cdots & 0 \\ \vdots & \ddots & \vdots \\ 0 & \cdots & 1\end{bmatrix} \tag{3.9}$$

for the companion model, and considering all branch currents to enter the model according to (3.2).

Additional equations to close the problem are provided from voltage drops by *Kirchhoff's voltage law* (KVL):

> The algebraic sum of voltage drops around any loop in the circuit is zero.

Although many modeling paradigms, like State Variable [9], Sparse Tableau [11] or Nodal Analysis [14], can be derived combining KCL, KVL and elemental constitutive relations, our choice for this thesis falls on Modified Nodal Analysis (MNA) [54] as it is best suitable for implementation in a modular framework.

Original formulation of MNA keeps the node potential vector $\mathbf{e}$, the inductor current vector $\mathbf{i}_{\mathrm{L}}$ and the voltage source current vector $\mathbf{i}_{\mathrm{V}}$ as model variables. As it can be shown that original MNA formulation does not preserve charge and magnetic flux conservation when solved numerically, we chose instead the *charge–oriented formulation* of [38, 39], where electric charges of capacitances $\mathbf{q}$ and magnetic

[1] Notice that choosing $\begin{bmatrix}-1 & 1\end{bmatrix}$ fixes the direction of voltage drops. This is fundamental for compact models of nonlinear circuit components.

fluxes of inductances $\boldsymbol{\psi}$ are added as explicit unknowns to the system, classifiable together with $\mathbf{i}_{\mathrm{L}}$, $\mathbf{i}_{\mathrm{V}}$ as *internal variables.*

Charge–oriented MNA formulation then derives a closed system of equations by:

1. enforcing KCL at every node of the circuit graph,
2. expressing the current of each voltage controllable element in terms of node potentials, internal variables, and time derivatives of the internal variables,
3. complementing the system with constitutive relations (3.4b), (3.5).

A set of *differential algebraic equations* (DAEs) stems from charge–oriented MNA formulations: this will ask for some care in the choice of the time discretization method when designing a numerical solution procedure [50]. The DAE system can be written in a notation that clearly underlines each elemental type contribution. In the most general case a charge–oriented MNA formulation reads:

$$\begin{aligned} A_{\mathrm{C}}\frac{\mathrm{d}\mathbf{q}}{\mathrm{d}t} + A_{\mathrm{R}}\mathbf{r}(A_{\mathrm{R}}^{*T}\mathbf{e}) + A_{\mathrm{L}}\mathbf{i}_{\mathrm{L}} + A_{\mathrm{V}}\mathbf{i}_{\mathrm{V}} + A_{\mathrm{I}}\mathbf{i}(A^{*T}\mathbf{e}, \frac{\mathrm{d}\mathbf{q}}{\mathrm{d}t}, \mathbf{i}_{\mathrm{L}}, \mathbf{i}_{\mathrm{V}}; t) &= 0, \\ \frac{\mathrm{d}\boldsymbol{\psi}}{\mathrm{d}t} - A_{\mathrm{L}}^{*T}\mathbf{e} &= 0 \\ A_{\mathrm{V}}^{*T}\mathbf{e} - \mathbf{v}(A^{*T}\mathbf{e}, \frac{\mathrm{d}\mathbf{q}}{\mathrm{d}t}, \mathbf{i}_{\mathrm{L}}, \mathbf{i}_{\mathrm{V}}; t) &= 0, \\ \mathbf{q} - \mathbf{q}_{\mathrm{C}}(A_{\mathrm{C}}^{*T}\mathbf{e}) &= 0, \\ \boldsymbol{\psi} - \boldsymbol{\psi}_{\mathrm{L}}(\mathbf{i}_{\mathrm{L}}) &= 0. \end{aligned} \tag{3.10}$$

It should be noticed, for the sake of completeness, that controlled sources cannot be prescribed arbitrarily in 3.10 but are instead subject to some constraints (see [41] for a deeper treatment of the subject) in order to limit the index of the overall system to be minor than or equal to 2.

3.2. Coupling Lumped-Element Circuit and Distributed Devices

As we aim to produce a complete set of equations describing distributed device and circuit behavior, we will need a framework into which all elements are coupled. In section 3.1, we introduced KCL current balance (3.3), defined some constitutive relations (3.4),(3.5), and finally built a generic form (3.10) of the DAE system regulating circuit behavior.

Here we formalize the *element–wise* description implied in the previous section. Each element can be thought of as described by a (possibly empty, as for resistors) set of internal variables $\mathbf{r}_m \in \mathbb{R}^{I_m}$ plus the voltage drops $A_m^{*T}\mathbf{e}$ across its pins. Equations defining the *current vector* related to each element, depend on the

internal variables and on the voltage drops, and only linearly on time derivatives of internal variables:

$$\mathbf{i}_m = D_m \dot{\mathbf{r}}_m + \mathbf{J}(A_m^{*T}\mathbf{e}, \mathbf{r}_m; t), \tag{3.11}$$

where $D_m \in \mathbb{R}^{k \times I_m}$ and $\mathbf{J}(\cdot; t) : \mathbb{R}^{k-1} \times \mathbb{R}^{I_m} \to \mathbb{R}^k$ for k–pins elements. For example, the equations for a capacitor would read:

$$\mathbf{i}_\mathrm{C} = \begin{bmatrix} -\dot{q}_\mathrm{C} \\ \dot{q}_\mathrm{C} \end{bmatrix} = \begin{bmatrix} -1 \\ 1 \end{bmatrix} \dot{\mathbf{r}}_\mathrm{C}, \tag{3.12}$$

with $D_\mathrm{C} = \begin{bmatrix} -1 & 1 \end{bmatrix}^T$ and $\mathbf{J}_\mathrm{C} = \begin{bmatrix} 0 & 0 \end{bmatrix}^T$, and the only internal variable being the capacitor charge q_C.

Constitutive equations share the same form, and we will indicate them as

$$B_m \dot{\mathbf{r}}_m + \mathbf{Q}(A_m^{*T}\mathbf{e}, \mathbf{r}_m; t) = 0, \tag{3.13}$$

with $B_m \in \mathbb{R}^{I_m \times I_m}$ and $\mathbf{Q}(\cdot; t) : \mathbb{R}^{k-1} \times \mathbb{R}^{I_m} \to \mathbb{R}^{I_m}$. Carrying on with the capacitor example, $B_\mathrm{C} = \begin{bmatrix} 0 \end{bmatrix}$, while according to (3.10) and assuming a linear relation,

$$\mathbf{Q}_\mathrm{C}(\mathbf{x}, \mathbf{r}_\mathrm{C}; t) = \mathbf{r}_\mathrm{C} - C\mathbf{x} = q_\mathrm{C} - C\mathbf{x}, \tag{3.14}$$

which becomes the familiar $q_\mathrm{C} = Cv_\mathrm{C}$ relation when the voltage drop $v_\mathrm{C} = A_\mathrm{C}^{*T}\mathbf{e}$ is plugged in.

This reformulation leads to the following compact expression:

$$\sum_{m=1}^{M} [A_m D_m \dot{\mathbf{r}}_m + A_m \mathbf{J}_m(A_m^{*T}\mathbf{e}, \mathbf{r}_m; t)] = 0 \tag{3.15a}$$

$$B_m \dot{\mathbf{r}}_m + \mathbf{Q}_m(A_m^{*T}\mathbf{e}, \mathbf{r}_m; t) = 0 \qquad \forall m = [1, .., M] \tag{3.15b}$$

which allows to approach the assembly of (3.10) in an element–wise fashion:

For every circuit element m in $[1, .., M]$,

1. sum the contribution $A_m\big(b_m \dot{\mathbf{r}}_m + \mathrm{J}(A_m^{*T}\mathbf{e}, \mathbf{r}_m; t)\big)$ to the current balance (3.15a),
2. add the constitutive relation $B_m \dot{\mathbf{r}}_m + \mathbf{Q}_m(A_m^{*T}\mathbf{e}, \mathbf{r}_m; t) = 0$ to the system.

Notice that the assumption that only time derivatives of internal variables appear, and that terms involving such derivatives are linear, does not impose restrictions on the applicability of the model, as both assumptions could be easily fulfilled by addition of new internal variables.

In order to couple the continuous, distributed device with the circuit, we need to recast the drift–diffusion equations in a form analogue to (3.11),(3.13), to obtain an

abstract differential algebraic system (see [46]), whose form reads for S distributed K_s–pins devices $M+1, M+2..., M+S$:

$$D_{M+s}\dot{\mathbf{r}}_{M+s} = 0, \tag{3.16a}$$

$$\mathbf{J}_{M+s}(\mathbf{r}_{M+s}) = \begin{bmatrix} I_1(\mathbf{r}_{M+s}) \\ I_2(\mathbf{r}_{M+s}) \\ \vdots \\ I_{K_s}(\mathbf{r}_{M+s}) \end{bmatrix}, \tag{3.16b}$$

$$\mathcal{B}_{M+s}\dot{\mathbf{r}}_{M+s} = \begin{bmatrix} 0 \\ 0 \\ \dot{n} \\ 0 \\ \dot{p} \\ 0 \end{bmatrix}, \tag{3.16c}$$

$$\boldsymbol{\mathcal{Q}}_{M+s}(A_m^{*T}\mathbf{e}, \mathbf{r}_{M+s}) = \begin{bmatrix} q(n-p-N_{\mathrm{bi}}) - \nabla\cdot(\varepsilon\nabla\phi) \\ \Psi_\phi(A_{M+s}^{*T}\mathbf{e}, \phi, n, p) \\ \nabla\cdot \vec{J}_n(\nabla\phi, n, p) + R \\ \Psi_n(A_{M+s}^{*T}\mathbf{e}, \phi, n, p) \\ \nabla\cdot \vec{J}_p(\nabla\phi, n, p) + R \\ \Psi_p(A_{M+s}^{*T}\mathbf{e}, \phi, n, p) \end{bmatrix}, \tag{3.16d}$$

where:

- D_{M+s} is defined on an appropriate function space $\mathcal{H}$, and to $\mathbb{R}^{K_s}$,
- each I_k is defined as in (k-current) as a functional on $\mathcal{H}$,
- $\mathcal{B}_{M+s}$ and $\boldsymbol{\mathcal{Q}}_{M+s}$ are defined on $\mathcal{H}$ and $\mathcal{H}\times\mathbb{R}^{K_s}$ respectively, to an appropriate space $\hat{\mathcal{H}}$
- Ψ_ϕ, Ψ_n, Ψ_p enforce the proper boundary conditions (ϕ-bcs), (n-bcs),(p-bcs).

The final, mixed–mode system reads then:

$$\sum_{l=1}^{M+S} [A_l D_l \dot{\mathbf{r}}_l + A_l \mathbf{J}_l(A_l^{*T}\mathbf{e}, \mathbf{r}_l; t)] = 0 \tag{mixed.a}$$

$$B_m\dot{\mathbf{r}}_m + \mathbf{Q}_m(A_m^{*T}\mathbf{e}, \mathbf{r}_m; t) = 0 \qquad \forall m = [1, .., M] \tag{mixed.b}$$

$$\mathcal{B}_s\dot{\mathbf{r}}_s + \boldsymbol{\mathcal{Q}}_s(A_s^{*T}\mathbf{e}, \mathbf{r}_s; t) = 0 \qquad \forall s = M + [1, .., S] \tag{mixed.c}$$

Going into further detail is out of the scope of this work, as in our case the abstract system is only an intermediate step, and we will show later on that after space discretization the exact form of (3.13) will be recovered.

3.3. Analytical Results for the Coupled System

The first analytical results on the well posedness of systems of the form (mixed) is presented in [45] for the coupling of generic circuits and the steady–state drift–diffusion system. Successive works extended the treatment to the parabolic problem (e.g. [47, 46]); we summarize here the results from [47] which, albeit being restricted to 1D semiconductor devices, highlight the functional setting in which the solution of our problem can be searched for.

We denote with $\mathcal{L}^2_\Omega$ and $\mathcal{H}^2_\Omega$ the spaces of square integrable functions on Ω and the respective first order Sobolev space. The symbol $\mathcal{L}^2_+$ denotes the subset of $\mathcal{L}^2$ of all almost everywhere positive functions. Given a time interval $I_T = [0, T]$, and a Banach space V, then we define with $C(I_T; V)$ the space of continuous functions on I_T with values in V, and with $\mathcal{L}^2(I_T; V)$ the space of square integrable functions, and with $\mathcal{H}^2(I_T; V)$ the related Sobolev space. Then:

$$X = \{u \in \mathcal{H}^2_\Omega : u|_{\Gamma_\mathrm{D}} = 0\} \tag{3.18}$$

$$Y = C(I_T; \mathcal{L}^2_\Omega) \cap \mathcal{L}^2(I_T; X) \cap \mathcal{H}^2(I_T; X^*) \tag{3.19}$$

$$C_\mathrm{D} = C(I_T, \mathbb{R}^{n_\mathrm{D}}) \tag{3.20}$$

$$C_\mathrm{A} = C(I_T, \mathbb{R}^{n_\mathrm{A}}) \tag{3.21}$$

where X^* is the dual space of X, and n_D, n_A are the dimensions of the differential part $\mathbf{y}$ and the algebraic part $\mathbf{z}$ of the circuit state vector $[\mathbf{e}, \mathbf{r}_1, \ldots \mathbf{r}_M]^T$ (see [40]). Finally, the tuple $[\mathbf{y}, \mathbf{z}, \phi, n, p]^T$ is defined to be a solution of the problem if

- $\mathbf{z}(t) \in C_\mathrm{A}$ satisfies the algebraic constraints in the circuital equations,
- $\mathbf{y}(t) \in C_\mathrm{D}$ satisfies properly defined initial conditions, and the differential circuital equations,
- n and p belong to $C(I_T; \mathcal{L}^2_+)$, and if relieved of the equilibrium components n_eq, p_eq, belong to Y,
- n and p satisfy the continuity equation in the sense of $\mathcal{H}^2(I_T; X^*)$,
- ϕ, relieved of boundary conditions depending on $\mathbf{y}$, satisfies Poisson's equation in the sense of X^*.

Theorem 5.5 of [47], then, states that

- letting the power sources be continuous in time,
- letting the network matrices related to passive components be symmetric, positive definite,
- letting some proper topological conditions enforcing physical consistency be fulfilled,

- assuming constant diffusivity and mobility,

the coupled problem admits a unique solution on the time interval I_T for any $T \in (0, \infty)$.

References

[1] E. M. Conwell and V. F. Weisskopf. “Theory of impurity scattering in semiconductors”. In: *Physics Review* 77 (1950), p. 388.

[2] W. van Roosbroeck. “Theory of the flow of electrons and holes in Germanium and other semiconductors”. In: *Bell System Technical Journal* 29 (1950), pp. 560–607.

[3] H. Brooks and Herring. “Scattering by ionized impurities in semiconductors”. In: *Physics Review* 83 (1951), p. 879.

[4] W. Shockley and W. T. Read. “Statistics of the Recombinations of Holes and Electrons”. In: *Phys. Rev.* 87.5 (Sept. 1952), pp. 835–. DOI: 10.1103/PhysRev.87.835.

[5] A.G. Chynoweth. “Ionization Rates for Electrons and Holes in Silicon”. In: *Physical Review* 109 (1958), pp. 1537–1540.

[6] Andrea De Mari. “Accurate numerical steady-state and transient one-dimensional solutions of semiconductor devices”. PhD thesis. California Institute of Technology, 1967. URL: http://resolver.caltech.edu/CaltechETD:etd-09262002-154912.

[7] Andrea De Mari. “An accurate numerical one-dimensional solution of the p-n junction under arbitrary transient conditions”. In: *Solid-State Electronics* 11.11 (1968), pp. 1021–1053. ISSN: 0038-1101. DOI: 10.1016/0038-1101(68)90126-3.

[8] Andrea De Mari. “An accurate numerical steady-state one-dimensional solution of the P-N junction”. In: *Solid-State Electronics* 11.1 (1968), pp. 33–58. ISSN: 0038-1101. DOI: 10.1016/0038-1101(68)90137-8.

[9] C. A. Desoer and E. S. Kuh. *Basic Circuit Theory*. Chapter 12. New York: McGraw-Hill, 1969.

[10] R. van Overstraeten and H. de Man. “Measurement fo the Ionization Rates in Diffused Silicon p-n Junctions”. In: *Solid-State Electronics* 13 (1970), pp. 583–608.

[11] G. Hachtel, R. Brayton, and F. Gustavson. “The Sparse Tableau Approach to Network Analysis and Design”. In: *Circuit Theory, IEEE Transactions on* 18.1 (Jan. 1971), pp. 101–113. ISSN: 0018-9324.

[12] W Bludau, A Onton, and W Heinke. “Temperature dependence of the band gap of silicon”. In: *Journal of Applied Physics* 45.4 (1974), pp. 1846–1848.

[13] C Canali, G Majni, et al. “Electron and hole drift velocity measurements in silicon and their empirical relation to electric field and temperature”. In: *Electron Devices, IEEE Transactions on* 22.11 (1975), pp. 1045–1047.

[14] L. O. Chua and P. M. Lin. *Computer-Aided Analysis for Electronic Circuits.* Englewood Cliffs: Prentice Hall, 1975.

[15] Jerry G. Fossum. "Computer-aided numerical analysis of silicon solar cells". In: *Solid-State Electronics* 19.4 (1976), pp. 269–277. ISSN: 0038-1101. DOI: 10.1016/0038-1101(76)90022-8.

[16] J W Slotboom and H C De Graaff. "Measurements of bandgap narrowing in Si bipolar transistors". In: *Solid-State Electronics* 19.10 (1976), pp. 857–862.

[17] J. Dziewior and W. Schmid. "Auger coefficients for highly doped and highly excited silicon". In: *Applied Physics Letters* 31.5 (1977), pp. 346–348. DOI: 10.1063/1.89694.

[18] J W Slotboom and H C De Graaff. "Bandgap narrowing in silicon bipolar transistors". In: *Electron Devices, IEEE Transactions on* 24.8 (1977), pp. 1123–1125.

[19] L Huldt, N G Nilsson, and K G Svantesson. "The temperature dependence of band-to-band Auger recombination in silicon". In: *Applied Physics Letters* 35.10 (1979), pp. 776–777.

[20] W Lochmann and A Haug. "Phonon-assisted Auger recombination in Si with direct calculation of the overlap integrals". In: *Solid State Communications* 35.7 (1980), pp. 553–556.

[21] J.G. Fossum and D.S.Lee. "A Physical Model for the Dependence of Carrier Lifetime on Doping Density in Nondegenerate Silicon". In: *Solid-State Electronics* 25 (1982), pp. 741–747.

[22] D.J Roulston, N.D. Arora, and S.G. Chamberlain. "Modeling and Measurement of Minority-Carrier Lifetime versus Doping in Diffused Layers of n+-p Silicon Diodes". In: *IEEE Transactions on Electron Devices* ED-29 (1982), pp. 284–291.

[23] J.G. Fossum, R.P. Mertens, et al. "Carrier recombination and lifetime in highly doped silicon". In: *Solid-State Electronics* 26.6 (1983), pp. 569–576. ISSN: 0038-1101. DOI: 10.1016/0038-1101(83)90173-9.

[24] Siegfried Selberherr. *Analysis and Simulation of Semiconductor Devices.* Springer Verlag Wien New York, 1984.

[25] Peter A. Markowich. *The stationary semiconductor device equations.* Vol. 1. Springer Science & Business Media, 1986.

[26] L.A. Chua, C.A. Desoer, and E.S. Kuh. *Linear ad Nonlinear Circuits.* Ed. by Mc Graw-Hill. New York: Mc Graw-Hill, 1987.

[27] Christian Ringhofer. "A Singular Perturbation Analysis for the Transient Semiconductor Device Equations in One Space Dimension". In: *IMA Journal of Applied Mathematics* 39.1 (1987), pp. 17–32. DOI: 10.1093/imamat/39.1.17.

[28] Christian Ringhofer. "An Asymptotic Analysis of a Transient p-n-Junction Model". In: *SIAM Journal on Applied Mathematics* 47.3 (1987), pp. 624–642. ISSN: 00361399.

[29] Uri M. Ascher, Peter A. Markowich, et al. “Conditioning of the steady state semiconductor device problem”. In: *SIAM Journal on Applied Mathematics* 49.1 (1989), pp. 165–185.

[30] Martin A Green. “Intrinsic concentration, effective densities of states, and effective mass in silicon”. In: *Journal of Applied Physics* 67.6 (1990), pp. 2944–2954.

[31] D B M Klaassen. “A unified mobility model for device simulation–I. Model equations and concentration dependence”. In: *Solid-State Electronics* 35.7 (1992), pp. 953–959.

[32] D.B.M. Klaassen. “A unified mobility model for device simulation—II. Temperature dependence of carrier mobility and lifetime”. In: *Solid-State Electronics* 35.7 (1992), pp. 961–967. ISSN: 0038-1101. DOI: 10.1016/0038-1101(92)90326-8.

[33] D.B.M. Klaassen, J.W. Slotboom, and H.C. de Graaf. “Unified Apparent Bandgap Narrowing in n- and p-Type Silicon”. In: *Solid-State Electronics* 35 (1992), pp. 125–129.

[34] G. Massobrio and P. Antognetti. *Semiconductor Device Modeling with SPICE*. 2nd. Mc Graw-Hill, Apr. 1993.

[35] Rolf Häcker and Andreas Hangleiter. “Intrinsic upper limits of the carrier lifetime in silicon”. In: *Journal of Applied Physics* 75.11 (1994), pp. 7570–7572. DOI: 10.1063/1.356634.

[36] T. Quarles, D. Pederson, et al. *SPICE3 Version 3F5 Users Guide*. Tech. rep. EECS Department, University of California, Berkeley, 1994.

[37] J.W. Jerome. *Analysis of Charge Transport*. Berlin Heidelberg: Springer-Verlag, 1996.

[38] M. Günther and U. Feldmann. “CAD-based electric-circuit modeling in industry. I. Mathematical structure and index of network equations”. In: *Surveys Math. Indust.* 8.2 (1999), pp. 97–129. ISSN: 0938-1953.

[39] M. Günther and U. Feldmann. “CAD-based electric-circuit modeling in industry. II. Impact of circuit configurations and parameters”. In: *Surveys Math. Indust.* 8.2 (1999), pp. 131–157. ISSN: 0938-1953.

[40] C. Tischendorf. “Topological index calculation of differential-algebraic equations in circuit simulation”. In: *Surv. Math. Ind.* 8 (1999), pp. 187–199.

[41] Diana Estévez Schwarz and Caren Tischendorf. “Structural analysis of electric circuits and consequences for MNA”. In: *International Journal of Circuit Theory and Applications* 28 (2000), pp. 131–162.

[42] Ingenuin Gasser. “The initial time layer problem and the quasineutral limit in a nonlinear drift diffusion model for semiconductors”. English. In: *Nonlinear Differential Equations and Applications NoDEA* 8.3 (2001), pp. 237–249. ISSN: 1021-9722. DOI: 10.1007/PL00001447.

[43] Ingenuin Gasser, C. David Levermore, et al. "The initial time layer problem and the quasineutral limit in the semiconductor drift-diffusion model". In: *European Journal of Applied Mathematics* null (04 Aug. 2001), pp. 497–512. ISSN: 1469-4425. DOI: 10.1017/S0956792501004533.

[44] Ingenuin Gasser, Ling Hsiao, et al. "Quasi-neutral Limit of a Nonlinear Drift Diffusion Model for Semiconductors". In: *Journal of Mathematical Analysis and Applications* 268.1 (2002), pp. 184–199. ISSN: 0022-247X. DOI: 10.1006/jmaa.2001.7813.

[45] G Alì, A Bartel, et al. "Elliptic partial differential-algebraic multiphysics models in electrical network design". In: *Mathematical Models and Methods in Applied Sciences* 13.09 (2003), pp. 1261–1278.

[46] Caren Tischendorf. "Coupled systems of differential algebraic and partial differential equations in circuit and device simulation. Modeling and numerical analysis". Habilitationsschrift. Humboldt-Univ. zu Berlin, 2004.

[47] Giuseppe Alì, Andreas Bartel, and Michael Günther. "Parabolic differential-algebraic models in electrical network design". In: *Multiscale Modeling & Simulation* 4.3 (2005), pp. 813–838.

[48] F. Brezzi, L.D. Marini, et al. "Discretization of Semiconductor Device Problems (I)". In: *Numerical Methods in Electromagnetics*. Vol. 13. Handbook of Numerical Analysis. Elsevier, 2005, pp. 317–441. DOI: 10.1016/S1570-8659(04)13004-4.

[49] A.J.H. Wachters and W.H.A. Schilders. "Simulation of EMC Behaviour". In: *Numerical Methods in Electromagnetics*. Vol. 13. Handbook of Numerical Analysis. Elsevier, 2005, pp. 661–753. DOI: 10.1016/S1570-8659(04)13007-X.

[50] Steffen Voigtmann. "General linear methods for integrated circuit design". PhD thesis. Humboldt-Universität zu Berlin, Mathematisch-Naturwissenschaftliche Fakultät II, 2006. URL: http://edoc.hu-berlin.de/docviews/abstract.php?id=27556.

[51] Massimiliano Culpo. "Numerical Algorithms for System Level Electro-Thermal Simulation". PhD thesis. Bergische Universität Wuppertal, 2009.

[52] Giuseppe Alì, Andreas Bartel, et al. "Analysis of a PDE Thermal Element Model for Electrothermal Circuit Simulation". English. In: *Scientific Computing in Electrical Engineering SCEE 2008*. Ed. by Janne Roos and Luis R.J. Costa. Vol. 14. Mathematics in Industry. Springer Berlin Heidelberg, 2010, pp. 273–280. ISBN: 978-3-642-12293-4. DOI: 10.1007/978-3-642-12294-1_35.

[53] Giuseppe Alì, Massimiliano Culpo, et al. "PDAE Modeling and Discretization". In: *Coupled Multiscale Simulation and Optimization in Nanoelectronics*. Ed. by Michael Günther. Vol. 21. Mathematics in Industry. Springer Berlin Heidelberg, 2015, pp. 15–102. ISBN: 978-3-662-46671-1. DOI: 10.1007/978-3-662-46672-8_2.

[54] Chung Wen Ho, A. Ruehli, and P. Brennan. "The modified nodal approach to network analysis". In: *Circuits and Systems, IEEE Transactions on* 22.6 (Jun 1975), pp. 504–509. ISSN: 0098-4094.

Part II.

Numerical algorithms

4. Time Discretization

In order to obtain a numerical approximation to the solution of (mixed), it is customary to discretize the system of equation in both time and space. With parabolic PDEs, when the time variable is discretized first, leading to a stationary elliptic equation at each time step that is then solved using appropriate techniques, then Rothe's method is being employed. In our case, where also the ordinary and algebraic equations are present, Rothe's method amounts to work the time discretization on the abstract system (mixed).

This chapter is structured as follows: first, section 4.1 addresses the choice of the time discretization scheme; following, section 4.2 discusses the time adaptation strategy employed in the final algorithm.

4.1. Implicit Schemes for DAE

For the choice of the numerical scheme to be adopted, the peculiar properties of DAE systems must be taken into account. The *backward differentiation formulae* are a family of linear, implicit, multi–step discretization schemes for differential equations, which are usually applied on stiff problems. When applied to a DAE system of the form

$$B\dot{\mathbf{u}} + F(\mathbf{u}; t) = 0, \tag{4.1}$$

which can in some sense be considered an *infinitely stiff problem*, the general BDF-K scheme takes the following form:

$$B \sum_{j=0}^{K} \alpha_{n,j} \mathbf{u}^{(n-j)} + F(\mathbf{u}^{(n)}; t_n) = 0. \tag{4.2}$$

In (4.1) and (4.2):

- $t_n \in [t_0, t_{\max}]$ indicates the n–th discrete time instant; the time step $t_n - t_{n-1}$ will be called δt_n hereon,
- $\mathbf{u}^{(n)} \in \mathbb{R}^D$ indicates the numerical approximation of the solution $\mathbf{u}(t_n)$
- $B \in \mathbb{R}^{D \times D}$ is a *singular* matrix; the dimension of $\ker B$ corresponds to the number of algebraic constraints,
- $F : \mathbb{R}^{D+1} \to \mathbb{R}^D$ is the forcing term, requiring some regularity,

- $\alpha_{n,j}$ are the scheme coefficients, depending on δt_n, δt_{n-1}, $\ldots \delta t_{n-K+1}$, and built so to maximize the truncation error order.

With few constraints (namely, passive circuital components and regular constitutive relations), it is possible to show that the DAE systems stemming from MNA are of index 1, or index 2 [14, 15] and this results in BDF schemes to be stable in the former case, or weakly unstable in the latter (see [16], section 1.2.4), with the source for instabilities coming from the errors of the nonlinear solver on determining some unknowns in the system. In the cited reference, estimates for such errors are also provided, further suggesting the choice of BDF methods.

In this thesis, the phenomena of interest show steep variations in time, and therefore adaptivity of time step is required to follow the solution's behavior without too much effort when it is smoother, but with the required accuracy when a fast transient is triggered. To simplify the definition of α_n, j with non uniform δt_n, the choice falls on the simplest method in the family, the BDF-1 or backward Euler method, where $\alpha_{n,0} = \delta t_n^{-1} = -\alpha_{n,1}$. Applying this scheme to the abstract system in (mixed) results in the semi-discrete problem:

$$\sum_{l=1}^{M+S} [A_l D_l \delta t_n^{-1} (\mathbf{r}_l^{(n)} - \mathbf{r}_l^{(n-1)}) + A_l \mathbf{J}_l (A_l^{*T} \mathbf{e}^{(n)}, \mathbf{r}_l^{(n)}; t_n)] = 0 \quad (4.3a)$$

$$B_m \delta t_n^{-1} (\mathbf{r}_m^{(n)} - \mathbf{r}_m^{(n-1)}) + \mathbf{Q}_m (A_m^T \mathbf{e}^{(n)}, \mathbf{r}_m^{(n)}; t_n) = 0 \qquad \forall m \quad (4.3b)$$

$$\mathcal{B}_s \delta t_n^{-1} (\mathbf{r}_s^{(n)} - \mathbf{r}_s^{(n-1)}) + \boldsymbol{\mathcal{Q}}_s (A_s^T \mathbf{e}^{(n)}, \mathbf{r}_s^{(n)}; t_n) = 0 \qquad \forall s \quad (4.3c)$$

or reformulating:

$$\sum_{l=1}^{M+S} A_l \widetilde{\mathbf{J}}_l (A_l^{*T} \mathbf{e}^{(n)}, \mathbf{r}_l^{(n)}; t_n, \delta t_n, \mathbf{r}_l^{(n-1)}) = 0 \quad (4.4a)$$

$$\widetilde{\mathbf{Q}}_m (A_m^T \mathbf{e}^{(n)}, \mathbf{r}_m^{(n)}; t_n, \delta t_n, \mathbf{r}_l^{(n-1)}) = 0 \qquad \forall m \quad (4.4b)$$

$$\widetilde{\boldsymbol{\mathcal{Q}}}_s (A_s^T \mathbf{e}^{(n)}, \mathbf{r}_s^{(n)}; t_n, \delta t_n, \mathbf{r}_l^{(n-1)}) = 0 \qquad \forall s \quad (4.4c)$$

which, given the approximate solution $\mathbf{r}^{(n-1)}$ at time step t_{n-1}, provides $\mathbf{r}^{(n)}$ by solving a nonlinear, coupled PDE-algebraic problem. In section 4.2 we will discuss how to choose the time step, while in chapter 5 we will present the method adopted to solve the nonlinear problem.

4.2. Time–step Adaptivity

In this subsection, we present the strategy adopted for time adaptivity in our algorithm, which is based on the extrapolation of the numerical solution from older time steps. Such extrapolation is also used in order to provide an initial guess for

the nonlinear algorithm: especially when Newton's or Newton–like methods are employed, a good starting guess is vital to achieve convergence.

Suppose $\mathbf{u}(t)$ is the solution of the generic DAE (4.1). If $\mathbf{u}$ is regular, then once defined

$$\gamma_{n+1} = \frac{\delta t_{n+1}}{\delta t_n}, \tag{4.5}$$

the first order approximation

$$\mathbf{u}(t_{n+1}) = (1+\gamma_{n+1})\mathbf{u}(t_n) - \gamma_{n+1}\mathbf{u}(t_{n-1}) + \mathcal{O}(\delta t_{n+1}^2), \tag{4.6}$$

is valid for δt_n, δt_{n+1} small enough, and such that γ_{n+1} is positive and bounded. Translated in the discretized setting of (4.2), we can regard the extrapolation

$$\mathbf{u}_0^{(n+1)} = (1+\gamma_{n+1})\mathbf{u}^{(n)} - \gamma_{n+1}\mathbf{u}^{(n-1)} \tag{4.7}$$

as a first guess for $\mathbf{u}^{(n+1)}$.

Suppose now we employ an iterative nonlinear solver to get to the next time step. We could then start from $\mathbf{u}_0^{(n+1)}$, and iterate until we obtain the numerical solution $\mathbf{u}^{(n+1)}$ which approximates $\mathbf{u}(t_{n+1})$. We can therefore assume

$$\left\|\mathbf{u}^{(n+1)} - \mathbf{u}_0^{(n+1)}\right\| \simeq C\delta t_{n+1}^2 \tag{4.8}$$

for some real constant C, thanks to (4.6). This relation allows to conveniently impose the next time step δt_{n+2}, since

$$\left\|\mathbf{u}^{(n+2)} - \mathbf{u}_0^{(n+2)}\right\| \simeq C\delta t_{n+2}^2 \simeq \left\|\mathbf{u}^{(n+1)} - \mathbf{u}_0^{(n+1)}\right\| \gamma_{n+2}^2. \tag{4.9}$$

If we want the extrapolation to give a good guess, i.e. limited by a tolerance τ^2:

$$\left\|\mathbf{u}^{(n+2)} - \mathbf{u}_0^{(n+2)}\right\| \leq \tau^2 \tag{4.10}$$

then we can choose the new time step according to

$$\delta t_{n+2} = \delta t_{n+1}\overline{\gamma}_{n+2} \tag{4.11}$$

where $\overline{\gamma}_{n+2}$ is defined as

$$\overline{\gamma}_{n+2} = \begin{cases} \gamma_{\min} & \text{if} \quad \gamma_{\min} > \alpha\tau \left\|\mathbf{u}^{(n+2)} - \mathbf{u}_0^{(n+2)}\right\|^{-\frac{1}{2}}, \\ \gamma_{\max} & \text{if} \quad \alpha\tau \left\|\mathbf{u}^{(n+2)} - \mathbf{u}_0^{(n+2)}\right\|^{-\frac{1}{2}} > \gamma_{\max}, \\ \alpha\tau \left\|\mathbf{u}^{(n+2)} - \mathbf{u}_0^{(n+2)}\right\|^{-\frac{1}{2}} & \text{otherwise,} \end{cases} \tag{4.12}$$

with $\gamma_{\min} < 1 < \gamma_{\max}$, and $\alpha = 0.616$ being a conservative parameter used to avoid excessive time step increment.

A remark needs to be made on the use of (4.11) for actual time step calculation. In general, the nonlinear solver may not guarantee convergence, which means $\|\mathbf{u}_k^{(n+1)} - \mathbf{u}_0^{(n+1)}\|$ either diverges or does not decrease with k, making (4.9) uncomputable. When such divergence occurs, time step can be used as a relaxation parameter of sorts: all computations in the current step are discarded, and the step is reinitialized with $\delta t_{n+1}^{\text{new}} = \gamma_{\min}\delta t_{n+1}^{\text{old}}$. The introduction of α and $\gamma_{\max}$ has thus the additional function of avoiding, as much as possible, the useless computation effort which is discarded after a non convergent nonlinear solve.

Reinterpretation as a predictor–corrector method It is possible to reinterpret the combination of (4.7) and (4.2) as a predictor–corrector method. In particular, if we fix the number of iterations m of some fixed point algorithm employed in the solution of (4.2), the described method takes the form of a two–step *predictor–multicorrector*, or $P(EC)^m$, scheme [20, 7]:

$$\mathbf{u}_0^{(n+1)} = (1+\gamma_{n+1})\mathbf{u}_m^{(n)} - \gamma_{n+1}\mathbf{u}_m^{(n-1)} \tag{P}$$

$$F_k^{(n+1)} = F(\mathbf{u}_{k-1}^{(n+1)}; t_{n+1}), \quad \forall k = 1,2,..,m \tag{E}$$

$$\mathbf{u}_k^{(n+1)} = \mathbf{u}_{k-1}^{(n+1)} - (B\alpha_{n,0} + F_k')^{-1}\left(B\alpha_{n,0}\mathbf{u}_{k-1}^{(n+1)} + B\sum_{j=1}^{K}\alpha_{n,j}\mathbf{u}_m^{(n-j)} + F_k^{(n+1)}\right), \quad \forall k = 1,2,..,m \tag{C}$$

In such framework, in fact, (4.7) takes the role of the predictor, while the fixed point iteration (Newton's method in the case of (C)) used in solving (4.2) is the corrector. It can be shown that the characteristic polynomial linked to the $P(EC)^m$ method depends mainly on the corrector, as the terms deriving from the predictor vanish when m grows, and in our case, the convergence properties depend only on the backward Euler method if $m > 1$ [see 20, pp. 511-].

5. Nonlinear Iterations

In this chapter, the two most common approaches for the linearization of the drift–diffusion equations are presented: Gummel's map, a functional iteration technique which beyond being employed in deriving analytical results is also often used in numerical simulations, and Newton's method, a variant of which our simulation tool relies on.

5.1. The Gummel Map

After time discretization as presented in chapter 4, the parabolic PDE system (Drift–Diffusion) can be rewritten as a sequence of elliptic systems of the form

$$\begin{cases} -\nabla\cdot\left(\varepsilon\nabla\phi^{(n)}\right) + q\left(n^{(n)} - p^{(n)} - N_{\mathrm{D}} + N_{\mathrm{A}}\right) = 0 & \text{in } \Omega, \\ -\nabla\cdot\left(\mu_n\left(\phi_{\mathrm{th}}\nabla n^{(n)} - n^{(n)}\nabla\phi^{(n)}\right)\right) + R^{(n)} + \delta t_n^{-1}\left(n^{(n)} - n^{(n-1)}\right) = 0 & \text{in } \Omega, \\ -\nabla\cdot\left(\mu_p\left(\phi_{\mathrm{th}}\nabla p^{(n)} + p^{(n)}\nabla\phi^{(n)}\right)\right) + R^{(n)} + \delta t_n^{-1}\left(p^{(n)} - p^{(n-1)}\right) = 0 & \text{in } \Omega. \end{cases} \tag{5.1}$$

Gummel's map is a scheme of functional iterations where the equations in 5.1 are decoupled, and then solved for in a loop, considering the other unknowns as data, until convergence conditions are not satisfied. The scheme can be seen as a nonlinear form of the Gauß–Seidel method.

The passages defining the algorithm are the following, where each map iteration is indicated by subscript k:

1. set the quasi–Fermi potentials according to

$$\begin{aligned} \phi_{n_{k-1}} &= \phi_{k-1} - \phi_{\mathrm{th}} \ln\left(\frac{n_{k-1}}{N_{\mathrm{i}}}\right) \\ \phi_{p_{k-1}} &= \phi_{k-1} + \phi_{\mathrm{th}} \ln\left(\frac{p_{k-1}}{N_{\mathrm{i}}}\right) \end{aligned} \tag{5.2}$$

2. solve the arising nonlinear Poisson equation for ϕ_k:

$$-\nabla\cdot(\varepsilon\nabla\phi_k) + q\left(N_{\mathrm{i}}\exp\left(\frac{\phi_k - \phi_{n_{k-1}}}{\phi_{\mathrm{th}}}\right) - N_{\mathrm{i}}\exp\left(\frac{-\phi_k + \phi_{p_{k-1}}}{\phi_{\mathrm{th}}}\right) - N_{\mathrm{bi}}\right) = 0 \tag{5.3}$$

3. solve for n_k

$$
\begin{aligned}
&- \nabla\cdot \big(\mu_n \left(\phi_{\mathrm{th}} \nabla n_k - n_k \nabla \phi_k\right)\big) + \\
&\qquad + \frac{n_k}{\delta t^n} + \frac{n_k p_{k-1}}{\tau_p(n_{k-1}+N_{\mathrm{i}}) + \tau_n(p_{k-1}+N_{\mathrm{i}})} + \\
&\qquad + (n_k p_{k-1})(C_n n_{k-1} + C_p p_{k-1}) = \\
&\qquad \frac{n^{(n-1)}}{\delta t_n} + \frac{N_{\mathrm{i}}^2}{\tau_n(p_{k-1}+N_{\mathrm{i}}) + \tau_p(n_{k-1}+N_{\mathrm{i}})} + \\
&\qquad + N_{\mathrm{i}}^2(C_n n_{k-1} + C_p p_{k-1}) + R^{\mathrm{II}}_{k-1}
\end{aligned}
\tag{5.4}
$$

4. solve for p_k

$$
\begin{aligned}
&- \nabla\cdot \big(\mu_p \left(\phi_{\mathrm{th}} \nabla p_k + p_k \nabla \phi_k\right)\big) + \\
&\qquad + \frac{p_k}{\delta t^n} + \frac{n_k p_k}{\tau_p(n_k+N_{\mathrm{i}}) + \tau_n(p_{k-1}+N_{\mathrm{i}})} + \\
&\qquad + (n_k p_k)(C_n n_k + C_p p_{k-1}) = \\
&\qquad \frac{n^{(n-1)}}{\delta t_n} + \frac{N_{\mathrm{i}}^2}{\tau_n(p_{k-1}+N_{\mathrm{i}}) + \tau_p(n_k+N_{\mathrm{i}})} + \\
&\qquad + N_{\mathrm{i}}^2(C_n n_k + C_p p_{k-1}) + R^{\mathrm{II}}_{k-1}
\end{aligned}
\tag{5.5}
$$

5. Update boundary conditions and impact ionization term R^{II}_k.

It is also possible to express Gummel's map with the help of either the quasi-Fermi potentials or the Slotboom variables. If the quasi-Fermi potential approach is taken, step 1. in the iteration is skipped, while step 3. of the iteration is transformed in:

3'. solve for ϕ_{nk}

$$
\begin{aligned}
&\nabla\cdot(\mu_n n_{k-1} \nabla \phi_{nk}) + \\
&\qquad + \frac{n_{k-1}}{\phi_{\mathrm{th}} \delta t^n}(\phi_k - \phi_{nk}) + \frac{p_{k-1} N_{\mathrm{i}} \exp\left(\frac{\phi_k - \phi_{nk}}{\phi_{\mathrm{th}}}\right)}{\tau_p(n_{k-1}+N_{\mathrm{i}}) + \tau_n(p_{k-1}+N_{\mathrm{i}})} + \\
&\qquad + \left(p_{k-1} N_{\mathrm{i}} \exp\left(\frac{\phi_k - \phi_{nk}}{\phi_{\mathrm{th}}}\right)\right)(C_n n_{k-1} + C_p p_{k-1}) = \\
&\qquad \frac{n_{k-1}}{\phi_{\mathrm{th}} \delta t_n}\left(\phi^{(n-1)} - \phi_n{}^{(n-1)}\right) + \frac{N_{\mathrm{i}}^2}{\tau_n(p_{k-1}+N_{\mathrm{i}}) + \tau_p(n_{k-1}+N_{\mathrm{i}})} + \\
&\qquad + N_{\mathrm{i}}^2(C_n n_{k-1} + C_p p_{k-1}) + R^{\mathrm{II}}_{k-1}
\end{aligned}
\tag{5.6}
$$

and then set

$$
n_k = N_{\mathrm{i}} \exp\left(\frac{\phi_k - \phi_{nk}}{\phi_{\mathrm{th}}}\right). \tag{5.7}
$$

while step 4. can be transformed similarly to compute $\phi_{p_k} and p_k$. This alternative formulation, while being possibly very useful as long as the analysis goes, becomes less attractive from a numerical standpoint, transforming the highly asymmetric but linear equations (5.4),(5.5) in symmetric, quasi-linear equations, with very sharply varying, almost discontinuous diffusion coefficients $\mu_n n$, $\mu_p p$.

The second option relies on introducing the *Slotboom variables* [8] which are defined in terms of electron and hole densities as:

$$n := u_n \exp(\tfrac{\phi}{\phi_{\text{th}}}), \qquad p := u_p \exp(\tfrac{-\phi}{\phi_{\text{th}}}). \tag{5.8}$$

Again, step 1. is skipped, and the continuity equation in step 3. transforms accordingly to

3". solve for u_{nk}

$$\begin{aligned}
&-\nabla\cdot\left(\mu_n \exp(\tfrac{\phi_{k-1}}{\phi_{\text{th}}})\nabla u_{nk}\right)+\\
&\quad+\frac{n_{k-1}\phi_k + u_{nk}\exp(\frac{\phi_k}{\phi_{\text{th}}})}{\phi_{\text{th}}\delta t^n}+\frac{p_{k-1}u_{nk}\exp(\frac{\phi_k}{\phi_{\text{th}}})}{\tau_p(n_{k-1}+N_{\text{i}})+\tau_n(p_{k-1}+N_{\text{i}})}+\\
&\quad+\left(p_{k-1}u_{nk}\exp(\tfrac{\phi_k}{\phi_{\text{th}}})\right)(C_n n_{k-1}+C_p p_{k-1}) =\\
&+\frac{n_{k-1}\phi^{(n-1)} + u_n{}^{(n-1)}\exp(\frac{\phi_k}{\phi_{\text{th}}})}{\phi_{\text{th}}\delta t^n}+\frac{N_{\text{i}}^2}{\tau_n(p_{k-1}+N_{\text{i}})+\tau_p(n_{k-1}+N_{\text{i}})}+\\
&\quad+N_{\text{i}}^2(C_n n_{k-1}+C_p p_{k-1})+R_{k-1}^{\text{II}}
\end{aligned} \tag{5.9}$$

and then set

$$n_k = u_{nk}\exp\left(\frac{\phi_k}{\phi_{\text{th}}}\right), \tag{5.10}$$

and similarly again for step 4. and the computation of p_k. Slotboom formulation provides linear and symmetric equations, but holds mainly theoretical interest (see section 6), as the coefficients and variables themselves are very often not computable, with the exponential functions rapidly exceeding machine representable quantities.

Experimentally, Gummel's map in ϕ-n-p form shows good global convergence properties in low injection regimes, independently from initial values, even if no general analytical result on its convergence is known besides for the zero recombination case. However, in high injection regimes the convergence rate slumps (see [see 17, pp. 333-]) and even if suitable acceleration techniques [12] could be used, Gummel's map is normally avoided in favor of a fully coupled Newton method, which we will discuss in the following section.

5.2. Newton's Method

This section has a twofold purpose. First, in subsection 5.2.1, it will introduce in abstract terms some numerical methods for root approximation stemming from

Newton's method. Those variations have different purposes, varying from the increase of reliability and robustness, to the reduction of computational cost, which are both strongly valued for our target application.

In second instance, in subsection 5.2.2, the application of the combined variations previously discussed will be put into practice on the coupled problem (4.4), and details on the implementation will be provided.

5.2.1. Newton–like methods

Newton's or Newton–Raphson's method is one of the most general algorithm for the approximation of roots of differentiable nonlinear functions

$$F(\mathbf{u}) = 0 \tag{5.11}$$

relying only on the local regularity of F which can be represented as

$$F(\mathbf{u}) = F(\mathbf{u} + \mathrm{d}\mathbf{u}) + J_{\mathbf{u}+\mathrm{d}\mathbf{u}}\,\mathrm{d}\mathbf{u} + \mathcal{O}(\|\,\mathrm{d}\mathbf{u}\|^2), \tag{5.12}$$

$J_{\mathbf{u}+\mathrm{d}\mathbf{u}}$ being the Jacobian of F evaluated in $\mathbf{u} + \mathrm{d}\mathbf{u}$. The conventional Newton method can then be defined as the iterative procedure

$$\mathrm{d}\mathbf{u}_k = -J_{\mathbf{u}_k}^{-1} F(\mathbf{u}_k) = -J_k^{-1}\mathbf{z}_k, \tag{5.13a}$$

$$\mathbf{u}_{k+1} = \mathbf{u}_k + \mathrm{d}\mathbf{u}_k, \tag{5.13b}$$

where $\mathbf{z}_k$ denotes the residual $F(\mathbf{u}_k)$ based on the k–th approximation, and an initial guess $\mathbf{u}_0$, needs be provided.

Newton's method can provide a *quadratic* convergence rate, in the following sense:

$$\|\mathbf{u}_{k+1} - \mathbf{u}\| \simeq C\|\mathbf{u}_k - \mathbf{u}\|^2, \tag{5.14}$$

for some real value C, but on the flip side, has limitations in that:

- the initial guess needs to be in a neighborhood of the exact solution, otherwise the algorithm may diverge or converge to a different root, should it exist,
- computing the Jacobians J_k and solving the respective linear systems may require huge computational cost,
- if $J_{\mathbf{u}}$ is singular or very ill–conditioned, the convergence rate decreases, even if convergence is not lost.

To remedy those issues, many possible variants of the algorithm can be introduced. In the following, we only deal with the ones relevant to our implementation.

Damped Newton method and Clamped Newton method

Especially when the Jacobian matrices are ill–conditioned, the conventional Newton method of (5.13) can produce big increments, and therefore move the approximate solution out of the neighborhood where convergence is achieved, or worse assume physically unacceptable values (e.g. a negative concentration, as we will see later on).

What is normally done in such cases is to artificially limit the increments at every step, in order to avoid too big oscillations. In formulas:

$$\mathrm{d}\mathbf{u}_k = -J_{\mathbf{u}_k}^{-1} F(\mathbf{u}_k) = -J_k^{-1}\mathbf{z}_k, \tag{5.15a}$$

$$\mathbf{u}_{k+1} = \mathbf{u}_k + \theta_k(\mathbf{u}_{k-1}, \mathrm{d}\mathbf{u}_k, k)\,\mathrm{d}\mathbf{u}_k, \tag{5.15b}$$

where the damping or relaxation coefficient θ_k may:

- be a constant parameter in $(0, 1]$; in this case, oscillations of the approximate solution are damped, but the quadratic convergence rate is lost;
- be a sequence such that $\lim_{k\to\infty} \theta_k = 1$. This is a necessary requirement for the method to maintain local quadratic convergence. Both those choices lead to the so called *damped Newton method.* It is also possible to devise expressions for $\theta_k(\mathbf{u}_{k-1}, \mathrm{d}\mathbf{u}_k, k)$, such that the damped Newton method converges globally under certain restrictions on F [3, 2, 1].
- it is also possible to impose that each increment does not produce a variation of the estimated solution greater than a certain threshold:

  $$\|\mathbf{g}(\mathbf{u}_k) - \mathbf{g}(\mathbf{u}_{k-1})\| \leq c \tag{5.16}$$

  where $\mathbf{g}$ is some continuous transformation of $\mathbf{u}_k$, devised in order for the components of the increment to be comparable, and involving scaling or other nonlinear transformations; thanks to the continuity of $\mathbf{g}$, moreover, $\theta_k \to 1$ upon convergence. This choice for the definition of θ_k leads to what is called *clamped Newton method.*

Modified Newton method

The main computational effort in one step of either conventional or damped Newton method, lies in the solution of the linear systems (5.13a) or (5.15a). However, it is usually possible to save much of the computations if the same linear system is solved more than once: think of the direct linear solvers, where factors can be stored and reused, but also iterative methods where complex preconditioners can be computed only once.

The *modified Newton method* allows for this recycling to occur, as it consists in iterating without updates on the Jacobian for a certain number of steps, with only the residual $\mathbf{z}_k$ (and hence, the source term in the linear system) changing.

Two basic patterns for updating J can be described, from which many possible variations could be derived:

- *Periodic updates*, meaning that every m steps, the Jacobian is recomputed and factorized:

$$\mathrm{d}\mathbf{u}_k = -J_{\bar{k}}^{-1}\mathbf{z}_k, \qquad \text{with } \bar{k} = m\left\lfloor \frac{k}{m} \right\rfloor \tag{5.17a}$$

$$\mathbf{u}_{k+1} = \mathbf{u}_k + \mathrm{d}\mathbf{u}_k, \tag{5.17b}$$

- *Convergence monitoring*, meaning that every l steps, *if* the residual or increment is not vanishing, the Jacobian is recomputed and factorized.

Approximate Newton method

Evaluation of Jacobian matrices is often difficult or computationally expensive. Moreover, linear systems of huge dimension are never solved exactly, even when direct methods are employed, let alone when iterative solvers need to be used (e.g. to comply with memory requirements).

All these factors result in every practical implementation of Newton–like methods to actually be an *approximate Newton method*, where the exact Jacobian matrix at each algorithmic step is approximated by a linear operator M_k. As long as the M_k approximate well enough the actual Jacobian matrix J_k (see [3] for a more precise definition) then the convergence properties of Newton's method (and its variants) can be preserved.

The generic approximate Newton method reads:

$$\mathrm{d}\mathbf{u}_k = -M_k^{-1}\mathbf{z}_k, \qquad \text{with } M_k \simeq J_k \tag{5.18a}$$

$$\mathbf{u}_{k+1} = \mathbf{u}_k + \mathrm{d}\mathbf{u}_k, \tag{5.18b}$$

and can be specialized in many forms:

- the modified Newton method can be viewed as an approximate Newton method, in the sense that $J_{\bar{k}} \simeq J_k$,
- *inexact Newton methods*, where iterative solvers are employed to approximate $J_k^{-1}\mathbf{z}_k$ up to a certain tolerance, depending on estimates of the linearization error, is also a form of approximate Newton method,
- methods stemming from discretization of PDEs, and possibly involving nonlinear stabilizations, where linearization is performed at the continuous level rather than the discretized level, can be viewed as approximate Newton methods for the discretized equations.

Same as for the previously presented methods, the algorithm implemented for this thesis features some characteristics of all of the classes discussed, and will be presented in the following subsection in further detail.

5.2.2. Implementation of the nonlinear solver

The present section is devoted to a more detailed description of the method implemented in the computational tool developed within the work for this thesis. First, the assembly strategy on the residual and the approximated Jacobian in our algorithm, together with a device-oriented decomposition, are defined; then the stopping and clamping criteria enforced are discussed in more detail.

Assembly of the system Jacobian and residual

As stated in section 3.2, the formulation of (mixed) is inherently modular, and therefore the system Jacobian and residual can be assembled with element–by–element *evaluation*. To this end, we can imagine what is usually called an *element evaluator*, namely an entity which for the given element, given the element internal variables and the pin voltages, can provide without information on the rest of the circuit the *element stamp* for the m–th element:

$$\left[\begin{array}{cc|c} \mathbb{J}_{m,\mathbf{e}}(A_m^{*T}\mathbf{e}_k,\mathbf{r}_{mk}) & \mathbb{J}_{m,\mathbf{r}_m}(A_m^{*T}\mathbf{e}_k,\mathbf{r}_{mk}) & \widetilde{\mathbf{J}}_m(A_m^{*T}\mathbf{e}_k,\mathbf{r}_{mk}) \\ \mathbb{Q}_{m,\mathbf{e}}(A_m^{*T}\mathbf{e}_k,\mathbf{r}_{mk}) & \mathbb{Q}_{m,\mathbf{r}_m}(A_m^{*T}\mathbf{e}_k,\mathbf{r}_{mk}) & \widetilde{\mathbf{Q}}_m(A_m^{*T}\mathbf{e}_k,\mathbf{r}_{mk}) \end{array}\right] \tag{5.19}$$

where the time step superscript $^{(n)}$ along with the parameters t_n, δt_n, $\mathbf{r}_l^{(n-1)}$ from (4.4) have been neglected for the sake of clarity. In (5.19), the symbols $\mathbb{J}_{m,\mathbf{e}}$, $\mathbb{J}_{m,\mathbf{r}_m}$ denote the Jacobian matrices of $\widetilde{\mathbf{J}}_m$ with respect to the pin voltages, and the internal variables respectively; in the same way $\mathbb{Q}_{m,\mathbf{e}}$, $\mathbb{Q}_{m,\mathbf{r}_m}$ denote the Jacobian matrices of $\widetilde{\mathbf{Q}}_m$. Subscript $_k$, in $\mathbf{e}_k$ and $\mathbf{r}_{mk}$, denotes the current Newton step, consistently with the notation of section 5.2.1.

The stamps, as defined in (5.19), can be assembled in the global Jacobian and residual, which are first filled "top to bottom" and "left to right" in block fashion:

$$\mathbb{J} = \begin{bmatrix} \sum_l A_l \mathbb{J}_{l,\mathbf{e}} A_l^{*T} & A_1 \mathbb{J}_{1,\mathbf{r}_1} & A_2 \mathbb{J}_{2,\mathbf{r}_2} & \cdots & A_m \mathbb{J}_{m,\mathbf{r}_m} \\ \mathbb{Q}_{1,\mathbf{e}} A_1^{*T} & \mathbb{Q}_{1,\mathbf{r}_1} & & & \\ \mathbb{Q}_{2,\mathbf{e}} A_2^{*T} & & \mathbb{Q}_{2,\mathbf{r}_2} & & \\ \vdots & & & \ddots & \\ \mathbb{Q}_{m,\mathbf{e}} A_m^{*T} & & & & \mathbb{Q}_{m,\mathbf{r}_m} \end{bmatrix}, \tag{5.20}$$

$$\mathbf{Z} = \begin{bmatrix} \sum_l A_l \widetilde{\mathbf{J}}_l(A_l^{*T}\mathbf{e}_k,\mathbf{r}_{mk}) \\ \widetilde{\mathbf{Q}}_1(A_1^{*T}\mathbf{e}_k,\mathbf{r}_{1k}) \\ \widetilde{\mathbf{Q}}_2(A_2^{*T}\mathbf{e}_k,\mathbf{r}_{2k}) \\ \vdots \\ \widetilde{\mathbf{Q}}_m(A_m^{*T}\mathbf{e}_k,\mathbf{r}_{mk}) \end{bmatrix}, \tag{5.21}$$

and then fed to the Newton–like algorithm of choice. In such framework, the element evaluator related to the distributed devices would provide the rightmost columns and bottom rows of $\mathbb{J}$ and $\mathbf{Z}$.

We will now examine in more detail the element evaluators linked to the distributed devices. Without any loss of generality, we will assume only one distributed device is present. As its internal variables, we will consider the contact currents vector $\mathbf{i}_{M+1}$, which we will denote simply by $\mathbf{i}$ in the following, and the distributed variables ϕ, n, p for which the drift–diffusion system provides constitutive relations. For the sake of brevity, the remaining circuital unknowns will be collected in the vector $\mathbf{w}$.

Moreover, as after discretization the bulk of the system state will be made of the variables representing the distributed device, and especially the carrier densities need to respect particular constraints (i.e. positivity), it makes sense to represent them in a more specialized fashion. To this regard, we can decompose the global Jacobian matrix and the residual as:

$$\mathbb{J} = \begin{bmatrix} \mathbb{J}_{\mathbf{ww}} & \mathbb{J}_{\mathbf{wi}} & \mathbb{J}_{\mathbf{w}\phi} & \mathbb{J}_{\mathbf{w}n} & \mathbb{J}_{\mathbf{w}p} \\ \mathbb{J}_{\mathbf{iw}} & \mathbb{J}_{\mathbf{ii}} & \mathbb{J}_{\mathbf{i}\phi} & \mathbb{J}_{\mathbf{i}n} & \mathbb{J}_{\mathbf{i}p} \\ \mathbb{J}_{\phi\mathbf{w}} & \mathbb{J}_{\phi\mathbf{i}} & \mathbb{J}_{\phi\phi} & \mathbb{J}_{\phi n} & \mathbb{J}_{\phi p} \\ \mathbb{J}_{n\mathbf{w}} & \mathbb{J}_{n\mathbf{i}} & \mathbb{J}_{n\phi} & \mathbb{J}_{nn} & \mathbb{J}_{np} \\ \mathbb{J}_{p\mathbf{w}} & \mathbb{J}_{p\mathbf{i}} & \mathbb{J}_{p\phi} & \mathbb{J}_{pn} & \mathbb{J}_{pp} \end{bmatrix}, \quad \mathbf{Z} = \begin{bmatrix} \mathbf{Z}_{\mathbf{w}} \\ \mathbf{Z}_{\mathbf{i}} \\ \mathbf{Z}_{\phi} \\ \mathbf{Z}_{n} \\ \mathbf{Z}_{p} \end{bmatrix}. \tag{5.22}$$

It is worth noting that many of the blocks of $\mathbb{J}$ in (5.22) are null, thanks to the definition of the distributed constitutive relation operator $\widetilde{\boldsymbol{\mathcal{Q}}}$, namely $\mathbb{J}_{\mathbf{w}\phi}$, $\mathbb{J}_{\mathbf{w}n}$, $\mathbb{J}_{\mathbf{w}p}$, $\mathbb{J}_{\mathbf{iw}}$, $\mathbb{J}_{n\mathbf{w}}$, $\mathbb{J}_{p\mathbf{w}}$, $\mathbb{J}_{\phi\mathbf{i}}$, $\mathbb{J}_{n\mathbf{i}}$, and $\mathbb{J}_{p\mathbf{i}}$. Moreover, upon discretization, if e.g. a basis of compact support functions is chosen in a Galerkin framework, the extra-diagonal blocks on the first column and on the second row are very sparse, containing nonzero entries only in the spots corresponding to the Dirichlet boundary.

The remaining nonzero elements on the second column consist into the device incidence matrix, as (3.3) is linear in the current, and into the identity matrix, as the contact currents are defined explicitly in (k-current). The blocks ranging from $\mathbb{J}_{\phi\phi}$ to $\mathbb{J}_{pp}$ pertain to the differential operators in space, defining (Drift–Diffusion), and boundary conditions:

- $\mathbb{J}_{\phi\phi}$ is based on the Laplace operator $-\lambda^2\Delta$, stemming from (Poisson) upon scaling; on the subspace related to Dirichlet boundaries, it enforces (ϕ-bcs) together with $\mathbb{J}_{\phi\mathbf{w}}$, which maps each pin to the corresponding contact subspace;
- $\mathbb{J}_{\phi n}$ and $\mathbb{J}_{\phi p}$ derive from the mass operator, stemming from the right hand side in (Poisson); coefficients amount to 1 and -1 upon scaling;
- $\mathbb{J}_{nn}$, stemming from (n-balance), collects both the diffusion–advection term

$$\mathbb{K}_n = -\mu_n(\phi_{\text{th}}\Delta + \nabla\phi \cdot \nabla),$$

  and reaction terms (δt^{-1} stemming from the time discretization, and R_n stemming from the Fréchet derivative of generation–recombination rates – derivatives of the mobility are neglected in our algorithm);

- $\mathbb{J}_{n\phi}$, neglecting the derivatives of mobility and impact ionization, reduces to the operator $\mu_n n\Delta$, which is self–adjoint, albeit with an extremely nonuniform diffusion coefficient;
- $\mathbb{J}_{np}$ is a reaction operator stemming from the Fréchet derivative R_p of the generation–recombination rates;
- $\mathbb{J}_{pp}$, $\mathbb{J}_{p\phi}$, $\mathbb{J}_{pn}$ in the last row stem from (p-balance), and follow the same pattern as the blocks described just above.

In the end, we will have a Jacobian matrix similar to the one analyzed in section 2.4:

$$\mathbb{J} = \begin{bmatrix} \mathbb{J}_{\mathbf{ww}} & A_{M+1} & 0 & 0 & 0 \\ 0 & \mathbb{I} & \mathbb{J}_{\mathbf{i}\phi} & \mathbb{J}_{\mathbf{i}n} & \mathbb{J}_{\mathbf{i}p} \\ \mathbb{J}_{\phi\mathbf{w}} & 0 & -\lambda^2\Delta & 1 & -1 \\ 0 & 0 & \mu_n n\Delta & \mathbb{K}_n & R_p \\ 0 & 0 & \mu_p p\Delta & R_n & \mathbb{K}_p \end{bmatrix}, \tag{5.23}$$

where we left the boundary conditions hidden for the sake of brevity.

Once defined the quasi-Jacobian $\mathbb{J}$ and the residual $\mathbf{Z}$, we can apply the procedure of (5.18), which consists in computing the variation

$$\mathrm{d}\mathbf{u}_k = \begin{bmatrix} \mathrm{d}\mathbf{w}_k & \mathrm{d}\mathbf{i}_k & \mathrm{d}\phi_k & \mathrm{d}n_k & \mathrm{d}p_k \end{bmatrix}^T \tag{5.24}$$

which satisfies:

$$\mathbb{J}_k \,\mathrm{d}\mathbf{u}_k = -\mathbf{Z}_k \tag{5.25}$$

and then applying it, with the necessary damping coefficient. The iterations stop when some criteria on either $\|\mathrm{d}\mathbf{u}_k\|$ or $\|\mathbf{Z}_k\|$ is satisfied. Computation of damping parameters and stopping criteria are the focus of next section.

Increment clamping and convergence checks

Chapters 6 and 7 are devoted to the discretization and solution of (5.25), while this subsection describes in abstract way the other component of the approximate Newton algorithm, namely:

$$\mathbf{u}_{k+1} = \mathbf{u}_k + \theta_k \,\mathrm{d}\mathbf{u}_k, \tag{5.26}$$

as well as the conditions upon which the loop is terminated.

The clamping parameter θ_k has several functions, which will be described by computing different $\theta_k^{\bullet}$, each one targeting a specific function, and then applying the minimum parameter computed. As we want to avoid over–relaxation in order to enhance robustness, the first parameter we introduce is $\theta_k^1 = 1$.

At every Newton step, we need to enforce both carriers positivity, namely $n_{k+1}, p_{k+1} > 0$. Our algorithm enforces this condition by defining

$$\theta_k^{n,0} = 0.9 \min_{\chi_{n,0}} \left(\frac{n_k}{|\,\mathrm{d}n_k|} \right), \qquad \text{with } \chi_{n,0} = \{x \in \Omega \mid n_k(x) + \mathrm{d}n_k(x) < 0\} \tag{5.27}$$

$$\theta_k^{p,0} = 0.9 \min_{\chi_{p,0}} \left(\frac{p_k}{|\,\mathrm{d}p_k|} \right), \qquad \text{with } \chi_{p,0} = \{x \in \Omega \mid p_k(x) + \mathrm{d}p_k(x) < 0\} \tag{5.28}$$

where the 0.9 factor is arbitrary. These two clamping factors are particularly important when fast depletion arises, as densities decrease fast but meet an inferior bound.

After enforcing positivity, we also deal with the "maximum step" type of constraints. The increment in electric potential $\mathrm{d}\phi_k$ at each Newton step is supposed not to exceed a fixed clamping voltage ϕ_{cl}, and thus

$$\theta_k^{\phi} = \phi_{\mathrm{cl}} \|\,\mathrm{d}\phi_k\|_{\infty}^{-1}, \tag{5.29}$$

where the clamping voltage is normally in the range of the thermal voltage ϕ_{th}.

A similar approach is taken with the quasi–Fermi potentials ϕ_n,ϕ_p defined in (2.18), which in turn need a less straightforward approach. In fact, the change in ϕ_n due to $\theta_k^n\,\mathrm{d}n_k$ is given by

$$\phi_n(n_k) - \phi_n(n_k + \theta_k^n\,\mathrm{d}n_k) = \phi_{\mathrm{th}} \ln \frac{n_k + \theta_k^n\,\mathrm{d}n_k}{n_k}, \tag{5.30}$$

and thus the absolute variation is smaller than the clamping parameter $\phi_{n\mathrm{cl}}$ if

$$\left| \ln \frac{n_k + \theta_k^n\,\mathrm{d}n_k}{n_k} \right| \leq \frac{\phi_{n\mathrm{cl}}}{\phi_{\mathrm{th}}}. \tag{5.31}$$

This results in different parameters according to the sign of $\mathrm{d}n_k$, as the logarithm in (5.31) takes the same sign as the variation, being $n_k > 0$:

$$\begin{cases} \dfrac{\theta_k^{n+}\,\mathrm{d}n_k}{n_k} \leq e^{\frac{\phi_{n\mathrm{cl}}}{\phi_{\mathrm{th}}}} - 1, & \mathrm{d}n_k > 0, \\ \dfrac{-\theta_k^{n-}\,\mathrm{d}n_k}{n_k} \leq 1 - e^{-\frac{\phi_{n\mathrm{cl}}}{\phi_{\mathrm{th}}}}, & \mathrm{d}n_k < 0, \end{cases} \tag{5.32}$$

and finally, taking the maximum norm on the left hand side of (5.32), we can guarantee (5.31) by clamping with both.

$$\theta_k^{n+} = \left(e^{\frac{\phi_{n\mathrm{cl}}}{\phi_{\mathrm{th}}}} - 1 \right) \left\| \frac{\mathrm{d}n_k^+}{n_k} \right\|_{\infty}^{-1}, \tag{5.33}$$

$$\theta_k^{n-} = \left(1 - e^{-\frac{\phi_{n\mathrm{cl}}}{\phi_{\mathrm{th}}}} \right) \left\| \frac{\mathrm{d}n_k^-}{n_k} \right\|_{\infty}^{-1}, \tag{5.34}$$

being $\mathrm{d}n_k^+$ and $\mathrm{d}n_k^-$ the positive and negative part of $\mathrm{d}n_k$ respectively. An analogous argument yields for $\mathrm{d}p_k^+$ and $\mathrm{d}p_k^-$, which are then defined as

$$\theta_k^{p+} = \left(e^{\frac{\phi_{n\mathrm{cl}}}{\phi_{\mathrm{th}}}} - 1\right) \left\| \frac{\mathrm{d}p_k^+}{p_k} \right\|_\infty^{-1}, \tag{5.35}$$

$$\theta_k^{p-} = \left(1 - e^{-\frac{\phi_{n\mathrm{cl}}}{\phi_{\mathrm{th}}}}\right) \left\| \frac{\mathrm{d}p_k^-}{p_k} \right\|_\infty^{-1}. \tag{5.36}$$

Finally for the currents and circuit variables, some clamping constants are provided, and the clamping factors are defined accordingly as:

$$\theta_k^{\mathbf{i}} = \mathbf{i}_{\mathrm{cl}} \| \, \mathrm{d}\mathbf{i}_k \|_\infty^{-1}, \tag{5.37}$$

$$\theta_k^{\mathbf{w}} = \mathbf{w}_{\mathrm{cl}} \| \, \mathrm{d}\mathbf{w}_k \|_\infty^{-1}, \tag{5.38}$$

with the final, global clamping factor being set to:

$$\theta_k = \min \left[\theta_k^1 \quad \theta_k^{n,0} \quad \theta_k^{p,0} \quad \theta_k^{\phi} \quad \theta_k^{n+} \quad \theta_k^{n-} \quad \theta_k^{p+} \quad \theta_k^{p-} \quad \theta_k^{\mathbf{i}} \quad \theta_k^{\mathbf{w}}\right]. \tag{clamping}$$

After defining the clamping, we need to introduce stopping criteria; both residual–based and increment–based stopping criteria are implemented in our algorithm. Both of them are built in a hybrid fashion, automatically switching from relative to absolute criteria. The residual measure, e.g., is built in the following way:

$$z_k = \max_{\alpha \in \{\phi, n, p, \mathbf{i}, \mathbf{w}\}} \|\mathbf{Z}_{\alpha k}\|_\infty (s_\alpha + \|\mathbf{Z}_{\alpha 0}\|_\infty)^{-1}, \tag{5.39}$$

where s_α can be either 1, if non–dimensional equations are considered, or a suitable scaling factor, when considering dimensional equations (see section 2.4.1), with the function of transforming the measure to absolute whenever the initial residual may be already small.

Measuring the increment is performed with the same hybrid structure, but with a slightly different approach for carrier densities. Moreover, both a single step and a cumulative increment are computed, which we will call $\delta_{k,k+1}$ and $\delta_{k,0}$. The use for the latter will be clarified later. For electric potential, currents, and circuital variables, the form of the increment is the following:

$$\delta_{k,l}^{\alpha} = \|\alpha_k - \alpha_l\|_\infty (\alpha_{\mathrm{cl}} + \beta \|\alpha_k\|_\infty)^{-1}, \quad \alpha \in \{\phi, \mathbf{i}, \mathbf{w}\} \tag{5.40}$$

with $l = 0$ and $\beta = 1$ for the cumulative increment, while $l = k + 1$ and $\beta = \theta_k$ for the single step increment. For the carrier concentrations, coherently with the clamping definition, the increment is based on quasi–Fermi potentials:

$$\delta_{k,l}^{\alpha} = \phi_{\mathrm{th}} \| \ln \alpha_k - \ln \alpha_l \|_\infty (\phi_{\alpha \mathrm{cl}} + \beta \|\phi_{\alpha k}\|_\infty)^{-1}, \quad \alpha \in \{n, p\} \tag{5.41}$$

with the same conventions for l, β. Finally, the increment measure is given as

$$\delta_{k,l} = \max_{\alpha \in \{\phi, n, p, \mathbf{i}, \mathbf{w}\}} \delta_{k,l}^{\alpha}. \tag{5.42}$$

Implemented algorithm

All the ingredients of the approximated Newton method now defined, our algorithm will be now presented.

Given the initial guess $\mathbf{u}_0 = \begin{bmatrix}\mathbf{w}_0 & \mathbf{i}_0 & \phi_0 & n_0 & p_0\end{bmatrix}^T$ obtained through extrapolation as per (4.7), set $k = 0$ and enter the Newton method loop:

1. compute the residual
$$\mathbf{Z}_k = \begin{bmatrix}\mathbf{Z}_{\mathbf{w}k} & \mathbf{Z}_{\mathbf{i}k} & \mathbf{Z}_{\phi k} & \mathbf{Z}_{nk} & \mathbf{Z}_{pk}\end{bmatrix}^T$$
and the residual measure z_k;
2. compute the Jacobian $\mathbb{J}(\mathbf{u}_k)$;
3. factorize the Jacobian (or build preconditioners);
4. compute the increment
$$\mathrm{d}\mathbf{u}_k = \begin{bmatrix}\mathrm{d}\mathbf{w}_k & \mathrm{d}\mathbf{i}_k & \mathrm{d}\phi_k & \mathrm{d}n_k & \mathrm{d}p_k\end{bmatrix}^T$$
5. compute the clamping parameter θ_k
6. apply the clamped increment, and compute the next estimate:
$$\mathbf{u}_{k+1} = \mathbf{u}_k + \theta_k \, \mathrm{d}\mathbf{u}_k$$
7. compute the cumulative increment measure $\delta_{k+1,0}$;
8. **IF** ($\delta_{k+1,0} > \delta_{\mathrm{max}}$), decrease the current time step and restart;
9. compute the current increment measure $\delta_{k+1,k}$;
10. **IF** ($k \geq k_{\mathrm{c}}$) and ($\delta_{k+1,k} > \delta_{k-k_{\mathrm{c}}+1,k-k_{\mathrm{c}}}$) and ($z_k > z_{k-k_{\mathrm{c}}}$), the loop is diverging: decrease the current time step and restart;
11. **IF** ($\delta_{k+1,k} \leq \delta_{\mathrm{th}}$), the algorithm converged: compute the next time step, and move on;
12. **IF** ($z_k \leq z_{\mathrm{th}}$), the algorithm converged: compute the next time step, and move on;
13. set $l = 0$, $\mathbf{u}_{k,0} = \mathbf{u}_k$, and enter the modified Newton method loop:
    a) compute the residual
    $$\mathbf{Z}_{k,l} = \begin{bmatrix}\mathbf{Z}_{\mathbf{w}k,l} & \mathbf{Z}_{\mathbf{i}k,l} & \mathbf{Z}_{\phi k,l} & \mathbf{Z}_{nk,l} & \mathbf{Z}_{pk,l}\end{bmatrix}^T$$
    and the residual measure $z_{k,l}$;

b) compute the increment

$$d\mathbf{u}_{k,l} = \begin{bmatrix} d\mathbf{w}_{k,l} & d\mathbf{i}_{k,l} & d\phi_{k,l} & dn_{k,l} & dp_{k,l} \end{bmatrix}^T$$

c) compute the clamping parameter $\theta_{k,l}$

d) apply the clamped increment, and compute the next estimate:

$$\mathbf{u}_{k,l+1} = \mathbf{u}_{k,l} + \theta_{k,l}\, d\mathbf{u}_{k,l}$$

e) compute the current increment measure $\delta_{l+1,l}$;

f) **IF** $(l \geq k_c)$ and $(\delta_{l+1,l} > \delta_{l-k_c+1,l-k_c})$ and $(z_l > z_{l-k_c})$, the loop is diverging: discard the modified Newton loop;

g) **IF** $(\delta_{l+1,l} \leq \delta_{th})$, the algorithm converged: compute the next time step, and move on;

h) **IF** $(z_l \leq z_{th})$, the algorithm converged: compute the next time step, and move on;

i) **IF** $(l = l_{max})$, exit the loop, **ELSE**, set $l = l + 1$;

14. set $\mathbf{u}_{k+1} = \mathbf{u}_{k,l+1}$;

15. **IF** $(k = k_{max})$, issue a warning, then compute the next time step and move on, **ELSE**, set $k = k + 1$;

In the the algorithm exposition, we introduced the following quantities, which are algorithm parameters:

- δ_{max} is the maximum allowed increment per time step; if the cumulative increment outweighs δ_{max}, then either the Newton method is diverging, or insufficient time accuracy is assumed – either case leading to a reduction of the time step;
- k_c is the minimum number of steps – experience suggests to use 3 to 5 – before divergence is assumed;
- δ_{th}, z_{th} are the convergence thresholds, or tolerances;
- l_{max}, k_{max} are the maximum number of modified Newton and Newton steps.

6. Space Discretization

After decoupling the Drift-Diffusion equations with the Gummel map, or defining a Newton–like method to approximate the coupled system of equations, we need to discretize a sequence of Diffusion–Advection–Reaction linear operators with strongly spatially-dependent variable coefficients such that in some regions inside the device the drift term is dominant on the diffusion term.

For this kind of problems specific discretization techniques are necessary to avoid the presence of strong oscillations in numerical solutions. Examples of these techniques are upwind finite volume methods [6], streamline diffusion finite volume methods [5] or the Streamline–Upwind Pertrov–Galerkin (SUPG) formulation [4].

In simulating semiconductor devices it is possible to exploit the particular form of the convection term to symmetrize the diffusion and convection differential operators with an opportune change of variables reducing it to a diffusion operator. The method considered in this thesis uses this expression of the convection term to construct multidimensional extension of the classical Exponential Fitting Finite Difference method in one spacial dimension [9, 10, 13].

In section 6.1 we introduce the scalar Diffusion–Advection–Reaction model problem and we show that both linearized Poisson equation and continuity equations can be rewritten in this form with an opportune identification of the coefficients. In section 6.2 we perform the discretization of the model problem in two dimensions with the classical Galerkin/Finite Element method with piecewise linear function. In section 6.3, with Edge Averaged Finite Element (EAFE) method [13] we highlight the relation between the terms of the local matrix of EAFE discretization and the geometric properties of the triangulations. Finally in section 6.5 we introduce two possible extensions of the EAFE method for three-dimensional problems with tetrahedral meshes.

6.1. The Diffusion–Reaction Problem

Let us consider the following model problem:

$$\begin{cases} \mathrm{div}J(u) + \sigma\ u = f & \text{in } \Omega \\ J(u) = -a(x)\nabla u & \text{in } \Omega \\ \underline{J}(u)\ \underline{n} = 0 & \text{in } \Gamma_N \subset \partial\Omega \\ u = \overline{u} & \text{in} \Gamma_D \subset \partial\Omega \end{cases} \tag{6.1}$$

where $\Omega \in \mathbb{R}^d, d = 2,3$, $\partial\Omega = \overline{\Gamma_D \cup \Gamma_N}$, $0 < \underline{a} \leq a(x) \leq \overline{a}$, and $\sigma \geq 0$. The problem (6.1) is a typical *Diffusion–Reaction* Problem with a non vanishing source term, in which $a(x)$ represents the *diffusion coefficient*, $\sigma(x)$ is the *reaction coefficient* and $f(x)$ is the *source term*. Both the Poisson equation and the charge continuity equations may be cast to the form of (6.1), exploiting the Slotboom variables which we introduced in section 5.1. Thanks to this change of variables, we may rewrite the continuity equation for electrons as:

$$\begin{cases} -\mathrm{div}J(u_n) = U & \text{in } \Omega \\ J(u_n) = \mu_n\ V_{th} e^{\frac{\phi}{V_{th}}} \nabla(u_n) & \text{in } \Omega \end{cases} \tag{6.2}$$

and analogously for holes

$$\begin{cases} -\mathrm{div}J(u_p) = U & \text{in } \Omega \\ J(u_p) = \mu_p V_{th} e^{\frac{-\phi}{V_{th}}} \nabla(u_p) & \text{in } \Omega. \end{cases} \tag{6.3}$$

Equation (6.2) corresponds to (6.1) if we let $a(x) = \mu_n V_{th} e^{\frac{\phi}{V_{th}}}$, $\sigma = 0$ and $f = U$. Analogously, the (linearized) Poisson equation, takes the form (6.1) by letting

$$u = \delta\phi^{(k)},$$

$$f = +\mathrm{div}(\epsilon\nabla\phi^{(k)}) + q(n^{(k)} - p^{(k)} - N_d + N_a),$$

$$\sigma = -\frac{q}{V_{th}}(n^{(k)} + p^{(k)}).$$

6.2. The Galerkin/Finite Element Method

In order to introduce the discretization by means of the Galerkin/Finite Element method of the model problem (6.1) in two space dimensions, let us suppose from now on that $\overline{u} \equiv 0$. The latter assumption does not hinder the generality of the discussion as (6.1) can be easily reduced to an homogeneous problem by introducing a suitable *lifting* of the boundary datum. Under the simplifying assumption just introduced, the weak formulation of (6.1) reads:
Find $u \in V$ such that:

$$(J(u), \nabla v) + (\sigma u, v) = (f, v), \qquad \forall v \in V \tag{6.4}$$

where $V \equiv H^1_{0,\Gamma_D} \equiv \{v \in H^1(\Omega)|\ v|_{\Gamma_D} = 0\}$. The discrete formulation of (6.4) by the Galerkin method is obtained by introducing a family of subspaces $V_h \subset V$ of finite dimension and rewriting (6.4) as
Find $u_h \in V_h$ such that:

$$(J(u_h), \nabla v_h) + (\sigma u_h, v_h) = (f, v_h), \qquad \forall v_h \in V_h \tag{6.5}$$

Introducing a basis $\{\varphi_i\}_{i=1}^{N_h}$ for the space V_h, (6.5) becomes:
Find $u_i,\ i = 1, \ldots, N_h,\ u_i \in \mathbb{R}$ such that:

$$\sum_{j=1}^{N_a} u_j (J(\varphi_j), \nabla\varphi_i) + \sum_{j=1}^{N_h} u_j (\sigma\varphi_j, \varphi_i) = (f, \varphi_i) \qquad \forall \varphi_i,\ i = 1, \ldots, N_h \tag{6.6}$$

Equation (6.6) is an algebraic linear system with the unknowns $u_i,\ i = 1, \ldots, N_h$, $N_h = dim(V_h)$ which may be expressed in the form

$$[A + M]\underline{u} = \underline{f} \tag{6.7}$$

where the *stiffness matrix* A is defined as

$$A = [a_{ij}], \qquad a_{ij} = (J(\varphi_j), \nabla\varphi_i)$$

and the *mass matrix* M is defined as

$$M = [m_{ij}], \qquad m_{ij} = (\sigma\varphi_j, \varphi_i).$$

The vectors $\underline{u}$ and $\underline{f}$, are defined as

$$\underline{u} = [u_i]; \tag{6.8}$$

$$\underline{f} = [f_i], \qquad f_i = (f, \varphi_i). \tag{6.9}$$

In order to describe the method of (piece–wise linear, continuous) *Finite Elements* we need to introduce a *triangulation* $\mathcal{T}_h$ of the domain $\Omega \in \mathbb{R}$, *e.g.*, a partition of the domain Ω into triangular subdomains K such that:

$$\overline{\Omega} = \bigcup_{K \in \mathcal{T}_h} K \tag{6.10}$$

and

- $\mathrm{int}(K) \not\equiv \emptyset \forall K \in \mathcal{T}_h$;
- $\mathrm{int}(K_1) \cap \mathrm{int}(K_2) = \emptyset \qquad \forall K_1, K_2 \in \mathcal{T}_h$;
- If $F = K_1 \cap K_2 \not\equiv \emptyset, K_1 \not\equiv K_2 \in \mathcal{T}_h$ then F is either a common edge or a common vertex between K_1 and K_2;
- $\mathrm{diam}(K) \leq h \qquad \forall K \in \mathcal{T}_h$.

Definition A triangulation with n vertices of a domain in $\mathbb{R}^2$ is said to be a *Delaunay triangulation* if the circumcircle of each triangle does not contain any vertices of the triangulation in its interior (see figure6.1). A Delaunay triangulation

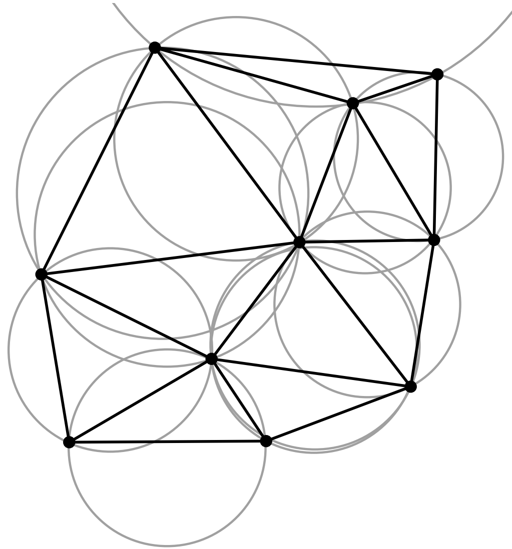

Figure 6.1.: Delaunay Triangulation (image from [21]).

enjoys the following properties:

- given a set of point, the Delaunay triangulation having those points as vertices is unique, unless M points ($M > 3$) lie on the same circumference;
- among all possible triangulations with the same set of vertices, the Delaunay maximizes the minimum angle of the triangles;
- the union of all triangles in a Delaunay triangulation is the minimal area convex polygon containing all vertices of the triangulation.

Let us introduce the space piece–wise linear continuous Finite Elements on $\mathcal{T}_h$ as

$$X_h^1 \equiv \left\{ v_h \in C^0(\Omega) |\ v_h|_K \in \mathbb{P}_1\ \forall K \in \mathcal{T}_h \right\} \tag{6.11}$$

and let

$$X^1_{h,\Gamma} \equiv \left\{ v_h \in X^1_h(\mathcal{T}_h) |\ v_h|_{\Gamma_D} = 0 \right\} \tag{6.12}$$

A basis for the space $X^1_{h,\Gamma}$ is given by the so called *hat functions* φ_i defined as

$$\varphi_i \in X^1_{h,\Gamma},\ \varphi_i(v_j) = \delta_{ij} \tag{6.13}$$

where v_j is the j–th vertex in the triangulation $\mathcal{T}_h$ and δ_{ij} is the Kronecker symbol. The functions φ_i defined in (6.13) are shown graphically in figure 6.2. With this

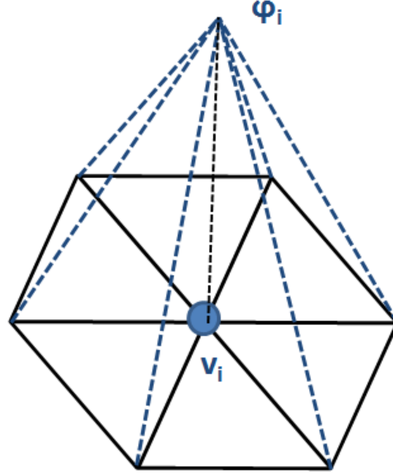

Figure 6.2.: Base function

definition it is possible to state the Finite Element method applied to problem (6.4) by choosing as the finite dimensional space V_h the space $X^1_{h,\Gamma}(\mathcal{T}_h)$ and using the functions (6.13) as a basis for V_h. In such a way the stiffness matrix A in (6.7) becomes:

$$\begin{aligned} A_{ij} = (J(\varphi_j), \nabla\varphi_i) = \sum_{K\in\mathcal{T}_h} \int_K J(\varphi_j)\nabla\varphi_i = \\ = \sum_K \int_K a(x)\nabla\varphi_j|_K \nabla\varphi_i|_K = \\ = \sum_K \int_K \underbrace{(\nabla\varphi_j|_K \nabla\varphi_i|_K)}_{\mathcal{L}^{(K)}_{ij}}\ \overline{a}^{(K)} = \sum_K A^{(K)}_{ij} \end{aligned} \tag{6.14}$$

where

$$\overline{a}^{(K)} = \frac{\int_K a(x)}{|K|} \qquad \text{e} \qquad \mathcal{L}^{(K)}_{ij} = \int_K (\nabla\varphi_j|_K \nabla\varphi_i|_K) = \nabla\varphi_j|_K \nabla\varphi_i|_K |K|. \tag{6.15}$$

In (6.14)–(6.15) the property that the gradients of the affine functions φ_j are constant on each triangle K has been exploited in the computation of the integrals. For computing the elements of the mass matrix M and of the right–hand–side vector f it is customary to resort to the well known technique of *mass–lumping* (described, *e.g.*, in [19]).

6.3. The Edge Averaged Finite Element (EAFE) Method

In the computational code which is the topic of this thesis a variant of the method of piece–wise linear continuous Finite Elements presented in the previous chapter has been used. Such variant is known as the method of *Edge Averaged Finite Element* (EAFE) [13], and is especially well suited for problems with rapidly varying (in space) coefficients. In the EAFE method the simple average $\overline{a}^K$ appearing in formula (6.14) for the coefficient $a(x)$ is replaced by an average along each edge of the triangulation $\mathcal{T}_h$, so that the stiffness matrix is computed via

$$A_{EAFE} = [A_{ij,EAFE}]; \qquad A_{ij,EAFE} = \sum_{K \in \mathcal{T}_h} \mathcal{L}_{ij}^{(K)} \overline{a}_{ij}^{(K)} \tag{6.16}$$

where $\overline{a}_{ij}^{(K)}$ is defined by

$$\overline{a}_{ij}^{(K)} = \left(\frac{1}{l_{ij}} \int_{e_{ij}} a^{-1}|_K \, de_{ij} \right)^{-1} \tag{6.17}$$

e_{ij} denoting the edge in the triangulation $\mathcal{T}_h$ connecting the i-th vertex to the j-th vertex and l_{ij} being its length. An interesting geometric interpretation is possible for the EAFE method, to explain which, we need to introduce some notation for the geometric entities on the triangle K. Referring to the schematic in figure 6.3 where, for sake of simplicity, the first three vertices in the triangulation v_i, $i = 1, 2, 3$ are considered, oriented in counter clockwise order, we define by e_{ij} the edge connecting the i-th vertex to the j-th vertex, we let l_{ij} denote the length of e_{ij} and t_{ij} denote the unit tangent vector to e_{ij} directed as e_{ij}. Let, finally, n_{ij} be the normal outwards–directed unit vector to e_{ij}, and let s_{ij} be the segment connecting the midpoint of e_{ij} to the intersection of the edge axes. Noticing that for each triangle K the following relations hold [6]:

$$|K| = \frac{1}{2} h_{ij} \; l_{ij} \tag{6.18}$$

$$l_{12} \; t_{12} + l_{23} \; t_{23} + l_{31} \; t_{31} = 0 \tag{6.19}$$

$$\nabla \varphi_i = - \frac{n_{(i+1)(i-1)}}{h_{(i+1)(i-1)}} \tag{6.20}$$

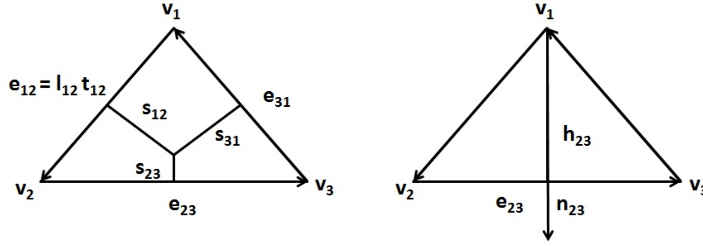

Figure 6.3.: Notation for triangles

$$l_{(i+1)(i-1)}\ t_{(i+1)(i-1)}\nabla\varphi_i = 0, \qquad l_{i(i\pm1)}\ t_{i(i\pm1)})\nabla\varphi_i = \pm 1 \tag{6.21}$$

$$s_{ij} = -|K|\ l_{ij}\ \nabla(\varphi_i)\ \nabla(\varphi_j) \tag{6.22}$$

it is easy to verify the following relation

$$\mathcal{L}_{ij}^{(K)} = \frac{-s_{ij}}{|e_{ij}||K|}. \tag{6.23}$$

Let us, furthermore, introduce the difference operator along e_{ij} which, for any continuous function η, is defined as

$$\partial_{ij}(\eta) := \eta(v_i) - \eta(v_j). \tag{6.24}$$

Using the relations (6.18)–(6.24) and proceeding as shown in [9], it is possible to introduce a piece–wise constant representation $\underline{J}_{h,EAFE}(u_h)$ for the flux $\underline{J}(u)$ appearing in (6.1) over the triangulation $\mathcal{T}_h$, defined as:

$$\underline{J}_{h,EAFE}(u_h)|_K = \underline{J}_{h,EAFE}(u_h)^{(K)} = \sum_{i,j\in v_k} \underline{j}_{ij}^{(K)}(u_h)\frac{l_{ij}s_{ij}}{|K|} \tag{6.25}$$

where i, j denote the vertices of the triangle K

$$\underline{j}_{ij}^{(K)}(u_h) := a_{ij}^{(K)}\frac{\partial_{ij}(u_h)}{l_{ij}}\underline{t}_{ij}. \tag{6.26}$$

From (6.25)–(6.26) it immediately follows that the representation $\underline{J}_{h,EAFE}(u_h)$ given by the EAFE method for the flux $\underline{J}(u)$ will have a continuous tangential component along each internal edge of the triangulation $\mathcal{T}_h$. Moreover $\underline{J}_{h,EAFE}(u_h)$ has a continuous normal component along the Voronoi cell [19] relative to each interior vertex of the triangulation $\mathcal{T}_h$ (see figure 6.4). The considerations given above allow to reinterpret the EAFE method as a Finite Volume method where the control volumes are the Voronoi cells, *i.e.*, it is equivalent to the method known as *Box Integration Method* (BIM) as shown in [9].

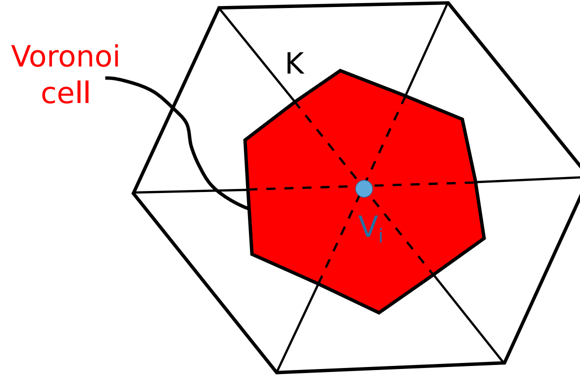

Figure 6.4.: Voronoi cell

Property 1 *If the triangulation $\mathcal{T}_h$ is Delaunay, the stiffness matrix A_{EAFE} is an M-matrix.*

Property 1, whose proof is given in [9], is of fundamental importance because it allows to guarantee the strict positivity of the Slotboom variables resulting from the solution of (6.7) which, in turn, is necessary in order to invert the relations defining the Slotboom variables and compute the carrier densities.

6.4. Exponential Fitting

Although the change of variables (5.8) is useful for the derivation of the EAFE method, it presents a major disadvantage which make its practical use unfeasible. Indeed, the computation of the coefficient $e^{\frac{\varphi}{V_{th}}}$ appearing in (5.8) may lead to numerical overflows when the ratio $\frac{\varphi}{V_{th}}$ becomes even moderately large. To work around this disadvantage one may perform an additional change of variable at the discrete level. Let us, as an example, consider below the case of the continuity equation for electrons; completely analogous arguments would hold in the case of holes. Let us consider the product of the stiffness matrix A_{EAFE} by the vector of unknowns $\underline{u}_h$ whose elements represent, in the present case, the nodal values of the variable u_n.

$$A_{EAFE}\ \underline{u} = \left(\sum_{K \in \mathcal{T}_h} A^{(K)}_{EAFE} \right) \underline{u} = \left(\sum_{K \in \mathcal{T}_h} A^{(K)}_{EAFE} \underline{u} \right) = \sum_{K \in \mathcal{T}_h} \left(\sum_{i,j \in v_K} \mathcal{L}_{ij} \overline{a}^{(K)}_{ij,EAFE} u_j \right). \quad (6.27)$$

If we apply for each vertex the inverse transformation of (5.8), then (6.27) may be rewritten as

$$\sum_{K \in \mathcal{T}_h} \sum_{i,j \in v_K} \mathcal{L}^{(K)}_{ij} \overline{a}^{(K)}_{ij,EAFE} \exp\left(\frac{-\phi_j}{V_{th}} \right) n_j = \sum_{K \in \mathcal{T}_h} \sum_{i,j \in v_K} \mathcal{L}^{(K)}_{ij} \tilde{a}^{(K)}_{ij} n_j \quad (6.28)$$

where ϕ_j denotes the nodal values of the electrical potential and n_j denotes the nodal values of the electron density. The coefficients $\tilde{a}_{ij}^{(K)}$ introduce in (6.28) are given by

$$\tilde{a}_{ij}^{(K)} = \mathcal{B}e \left(\delta_{ij} \left(\frac{\phi}{V_{th}} \right) \right) \tag{6.29}$$

where

$$\mathcal{B}e(x) = \frac{x}{e^x - 1}. \tag{6.30}$$

As a consequence, equation (6.27) may be written as

$$A_{EAFE}\ \underline{u} = \tilde{A}_{EAFE}\ \underline{n} = \sum_{K \in \mathcal{T}_h} \sum_{i,j \in v_K} \mathcal{L}_{ij}^{(K)} \tilde{a}_{ij}^{(K)} n_j. \tag{6.31}$$

The latter reformulation of the discrete problem is referred to as Exponentially Fitted Finite Element (EFFE). The stiffness matrix for the EFFE method is no more symmetric as for the EAFE method, but it enjoys the very important property that

Property 2 *The stiffness matrix $\tilde{A}_{EFFE}$ is an M-matrix whenever the triangulation $\mathcal{T}_h$ is Delaunay.*

6.5. 3D Extension of the EAFE Method

The steps that lead to the derivation of the EFFE discretization method, as shown in the preceding sections for the 2D case, can be reproduced exactly to obtain a 3D formulation of the problem, as long as the triangular partition of the 2D domain is substituted by a partition into tetrahedra. In the 3D case, though, unlike in the two-dimensional case, the Delaunay condition on the domain partition is not sufficient to guarantee that $\mathcal{L}_{i,j}^{(K)}$ be an M-matrix. In order to guarantee that $\mathcal{L}_{i,j}^{(K)}$ be an M-matrix one may adopt the Orthogonal Subdomain Collocation (OSC) [11] method for the construction of the the discrete Laplace operator. Without delving into the technical details of the OSC method, it is worth noting that such method can be interpreted as a correction of the 3D extension of the 2D EAFE method previously discussed. Such correction, involving the computation of the cross–sections for the stiffness matrix, results in relaxing the sufficient conditions on the grid needed to guarantee $A_{i,j}^{(K)}$ being an M-matrix for the 3D case.

7. Solution of the Linearized System

After linearization and discretization, approximating the solution of (mixed) ultimately results in the successive solution of a number of linear systems. This chapter discusses the choice of linear solvers suitable for the specific problems at hand, trying to exploit some peculiarities stemming from the form of the original problem.

7.1. LU Factorization and Fill–in

In the matrices arising from the discretized and linearized version of (mixed), the preponderant blocks normally arise from the discretized system of PDEs; system dimensions depends obviously on the number of mesh nodes, but also conditioning properties are driven in essence by the drift–diffusion block [22]. As for the continuous system (as seen in section 2.4), the discretized one happens to be badly scaled (see figure 7.1) and ill–conditioned. Standard iterative methods with generic preconditioning techniques are less suitable than sparse direct solver in these cases.

A typical sparse direct solver, in order to approximate the solution of the system $Ax = b$, works through four distinct phases, namely:

- *Analysis*, comprising reordering and symbolic factorization; for matrices stemming from 3D discretization, the computational complexity of the analysis phase is $O(r^{\frac{4}{3}})$, r being the number of rows in the system (see [18, p. 757]),
- *Numerical Factorization* of the sparse coefficient matrix A into triangular factors L and U using Gaussian elimination with or without partial pivoting;

Table 7.1.: Memory occupation for the assembled Jacobian, its LU factors, and for the factors involved in Gummel's map when direct methods are employed.

Mesh		S1	S2	S3	H1	H2	U
Growth rate α	Jacobian	1.02	1.02	1.03	0.97	1.02	1.06
	full LU	1.59	1.63	1.63	1.63	1.59	1.61
	Gummel	1.50	1.46	1.30	1.44	1.51	1.40
Memory usage $M(10^6)$	Jacobian [MB]	504.9	479.9	507.0	549.7	797.3	1120
	full LU [GB]	454.2	271.2	102.4	476.0	555.0	402.2
	Gummel [GB]	70.00	40.28	10.28	56.75	101.0	57.77

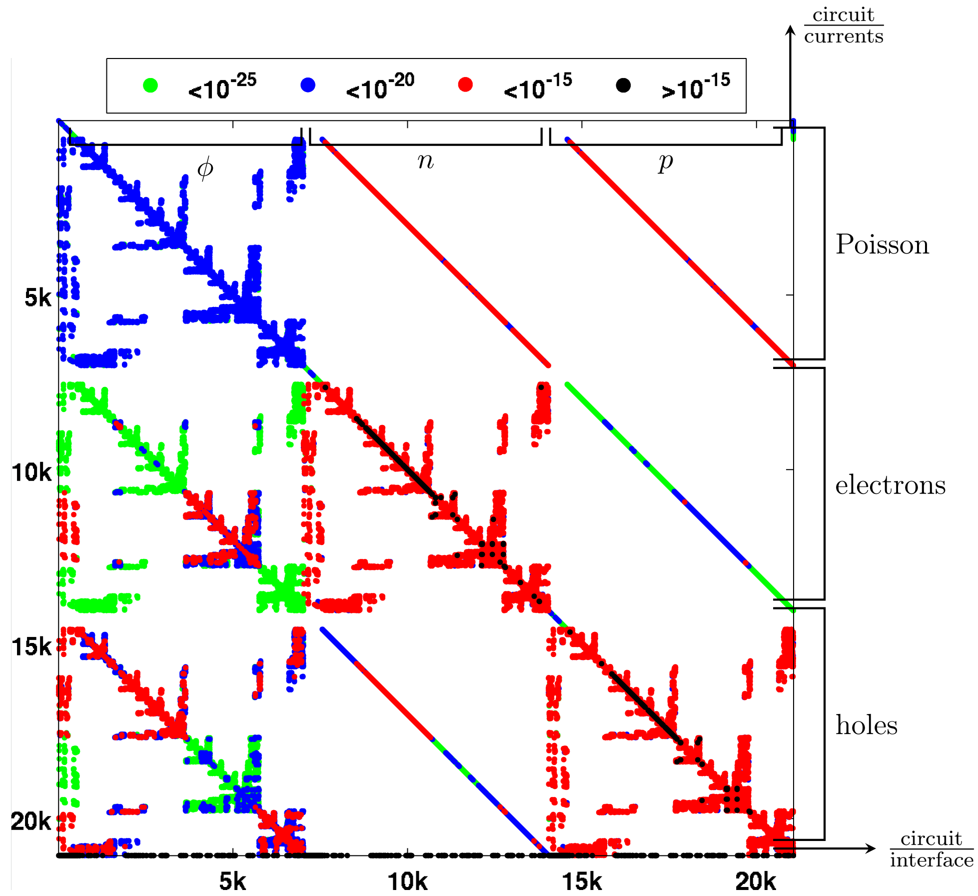

Figure 7.1.: Sparsity pattern of the Jacobian matrix for a *p*-*i*-*n* diode discretized over roughly 7000 nodes and coupled to a resistive circuit (see section9.2).

this phase is the most computationally demanding, with complexity $O(r^2)$ for 3D problems,

- *Forward and Backward Elimination* to solve for the unknown using the triangular factors L and U and the right hand side vector b; elimination phase also takes $O(r^{\frac{4}{3}})$ time.
- *Iterative Refinement* of the computed solution, with complexity $O(r)$.

The main issue when targeting with a direct solver problems discretized over big meshes with order of 10^6 nodes, however, is not the computational complexity but rather the memory consumption of the resulting LU factorization, because of the phenomenon known as *fill–in*: the number of nonzero entries in the factors L and U, is normally grater than the number of nonzero entries in A. This is-

sue is partially taken care of at the reordering phase, but cannot be completely eliminated.

A sparse matrix, by definition, has a number of nonzero entries which scales with r. If we define the memory occupation M of the sparse matrix as a function of the number of mesh nodes e, then

$$M(e) = O(e^{\alpha}). \tag{7.1}$$

If one of the many *ad hoc* formats to store sparse matrices is used, then the growth exponent α roughly equals one, as $r \simeq 3e$ for problems with big meshes and relatively simple circuits. The fill–in, however, results in a memory occupation for the factors which is not asymptotically linear.

Table 7.1 reports the results of an experiment devised to understand the behavior of α for the memory occupation of LU factors. Six different 3D meshes were taken:

- three structured meshes of a *p-i-n* diode, indicated with S1, S2, S3. The meshes were taken with different ratios of spatial step in the three directions, and are ordered from the more isotropic to the more anisotropic one;
- one unstructured mesh of the same device, indicated with U;
- two hybrid meshes, indicated with H1 and H2. The former, representing a bipolar junction transistor, was obtained through the combination of structured grids in the neighborhood of contacts and junctions, and unstructured grid in the remaining part of the domain. The latter, H2, representing a simplified thyristor (see chapter 10.2), was obtained through octree localized refinement.

For each mesh, starting from a coarse version, several uniform refinements were taken, the Jacobian matrix related to our problem was computed and factorized. The trends for all the different instances were found to fit very well the power law implied by (7.1), with the reported values for α.

The results in table 7.1 indicate that the memory occupation growth rate for the LU factors is very slightly dependent on the chosen type of mesh, and stays roughly constant at 1.6 for all six experiments. More concerning, on the other hand, is the estimation of the required memory for the target mesh dimensions, which makes performing simulations borderline unfeasible. In the same table, results for an analogue experiment performed on LU factors arising from a step of Gummel's map are reported. Confrontation with those data suggests that if a decoupled method could be found, such that the limitations of Gummel's map in high injection are overcome, not only the memory cost for a fixed mesh would be improved but also the growth rate α would be nearer to the theoretical $\frac{4}{3}$ mark.

7.2. Block Gauß–Seidel Iterations

In this section we propose a block–iterative approach to solve the linear systems associated with the Newton method iterations for (mixed). As already stated, for our target application the preponderant part of the system stems from the discretization of (Drift–Diffusion), thus we will concentrate on such part of the system before, and then consider how to couple the system with the controlling circuit. This approach is equivalent to restricting the external circuit to a set of ideal voltage sources: the sources constitutive relations could be easily removed, and the KCL and device currents become a post-processing step.

Then, one step of the Newton method for the restricted case consists essentially in solving a linear system where the coefficients matrix takes the form of the bottom-right blocks in (5.23):

$$\begin{cases} \mathbb{J}_{\phi\phi}\,\mathrm{d}\phi + \mathbb{J}_{\phi n}\,\mathrm{d}n + \mathbb{J}_{\phi p}\,\mathrm{d}p = -\mathbf{Z}_\phi, \\ \mathbb{J}_{n\phi}\,\mathrm{d}\phi + \mathbb{J}_{nn}\,\mathrm{d}n + \mathbb{J}_{pp}\,\mathrm{d}p = -\mathbf{Z}_n, \\ \mathbb{J}_{p\phi}\,\mathrm{d}\phi + \mathbb{J}_{pn}\,\mathrm{d}n + \mathbb{J}_{pp}\,\mathrm{d}p = -\mathbf{Z}_p. \end{cases} \tag{7.2}$$

The block Gauß–Seidel method consists in iterating over the lines of (7.2) one at a time, in the following way:

$$\begin{cases} \mathbb{J}_{\phi\phi}\,\mathrm{d}\phi^{[s+1]} + \mathbb{J}_{\phi n}\,\mathrm{d}n^{[s]} + \mathbb{J}_{\phi p}\,\mathrm{d}p^{[s]} = -\mathbf{Z}_\phi \\ \mathbb{J}_{n\phi}\,\mathrm{d}\phi^{[s+1]} + \mathbb{J}_{nn}\,\mathrm{d}n^{[s+1]} + \mathbb{J}_{np}\,\mathrm{d}p^{[s]} = -\mathbf{Z}_n \\ \mathbb{J}_{p\phi}\,\mathrm{d}\phi^{[s+1]} + \mathbb{J}_{pn}\,\mathrm{d}n^{[s+1]} + \mathbb{J}_{pp}\,\mathrm{d}p^{[s+1]} = -\mathbf{Z}_p \end{cases} \tag{BGS}$$

where the indexes in square brackets denote the in–solver iteration.

If this approach is taken, then only the diagonal blocks need to be factorized, leading to the same memory requirements of Gummel's map. Alternatively, the block–diagonals could also be "inverted" by means of iterative methods, with linear memory requirements, if necessary. Unlike with Gummel's map, however, the coupling between the variations $\mathrm{d}\phi$, $\mathrm{d}n$, $\mathrm{d}p$ are retained through the extra–diagonal blocks.

Being a stationary iterative method, however, the convergence of (BGS) is guaranteed for a generic source term only if its update operator, defined as

$$\mathbb{U} = \begin{bmatrix} \mathbb{J}_{\phi\phi} & 0 & 0 \\ \mathbb{J}_{n\phi} & \mathbb{J}_{nn} & 0 \\ \mathbb{J}_{p\phi} & \mathbb{J}_{pn} & \mathbb{J}_{pp} \end{bmatrix}^{-1} \begin{bmatrix} 0 & \mathbb{J}_{\phi n} & \mathbb{J}_{\phi p} \\ 0 & 0 & \mathbb{J}_{pp} \\ 0 & 0 & 0 \end{bmatrix} \tag{7.3}$$

has spectral radius $\rho_{\mathrm{BGS}} = \max_{\|x\|_2=1} \|\mathbb{U}x\|_2 < 1$.

Unfortunately, the plain application of the BGS solver, leads to spectral radii several orders of magnitude bigger than unity, due to the very bad scaling of the Jacobian when λ is small. An experiment over a *p-i-n* diode (see chapter 9.2 for more details) is reported in figure 7.2, which shows how the straightforward

appclication of the BGS produces spectral radii of over 10^5 for the range of λ which we target (spanning around the 10^{-5} mark).

Looking back at the conditioning analysis of section 2.4.2, and recalling that the standard Gauß–Seidel algorithm is guaranteed to converge if the matrix of coefficients is diagonally dominant, we can introduce the discretized counterpart of (2.90), and propose the change of variables

$$T = \begin{bmatrix} \mathbb{I} & 0 & 0 \\ n & \mathbb{I} & 0 \\ -p & 0 & \mathbb{I} \end{bmatrix}. \tag{7.4}$$

which enhances the decoupling of the equations. Employing this right preconditioner proves very effective, at least at thermal equilibrium, as can be seen in figure 7.3. Even when the spectral radius approaches unity, the convergence of the BGS solver can be enhanced by introducing vector extrapolation techniques.

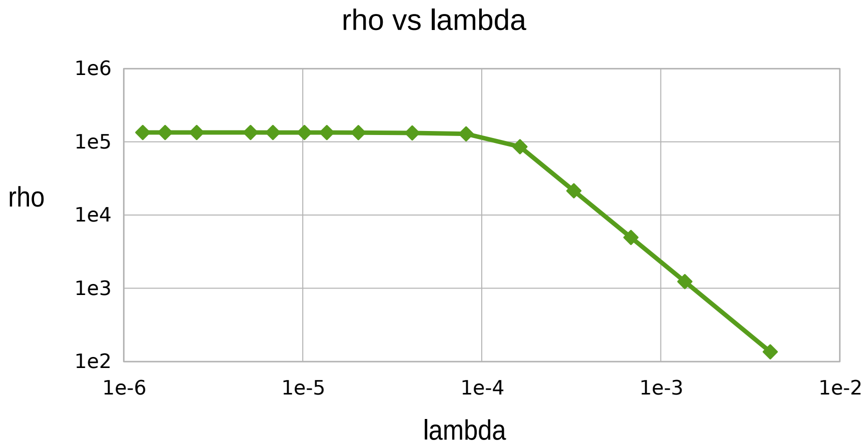

Figure 7.2.: Spectral radius in equilibrium conditions.

7.2.1. Device–circuit coupling

We will now address the matter of proper coupling between the circuital part in the framework of a block Gauß-Seidel method for the solution of a linear system. Three approaches have been analyzed to this end:

- coupling circuit variables and currents with the electric potential,
- device–driven simulation: eliminating the circuit trough static condensation,
- circuit–driven simulation: eliminating the device trough static condensation.

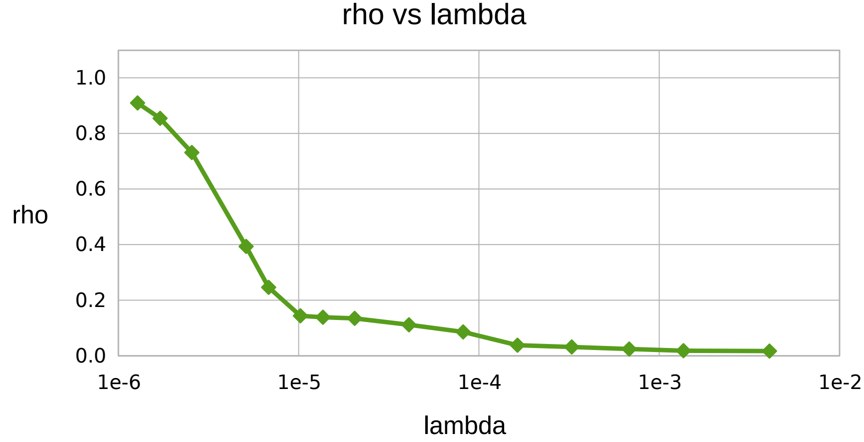

Figure 7.3.: Spectral radius in equilibrium conditions, after right preconditioning.

All three methods are described in the following.

Looking at the structure of (5.23), we can notice that there is no direct influence of the circuital variables $\mathbf{w}$ and the contact current $\mathbf{i}$ on the last two rows:

$$\begin{cases} \mathbb{J}_{\mathbf{ww}}\,\mathrm{d}\mathbf{w} & + & \mathbb{J}_{\mathbf{wi}}\,\mathrm{d}\mathbf{i} & + & 0 & + & 0 & + & 0 & = -\mathbf{Z}_{\mathbf{w}} \\ 0 & + & \mathbb{J}_{\mathbf{ii}}\,\mathrm{d}\mathbf{i} & + & \mathbb{J}_{\mathbf{i}\phi}\,\mathrm{d}\phi & + & \mathbb{J}_{\mathbf{i}n}\,\mathrm{d}n & + & \mathbb{J}_{\mathbf{i}p}\,\mathrm{d}p & = -\mathbf{Z}_{\mathbf{i}} \\ \mathbb{J}_{\phi\mathbf{w}}\,\mathrm{d}\mathbf{w} & + & 0 & + & \mathbb{J}_{\phi\phi}\,\mathrm{d}\phi & + & \mathbb{J}_{\phi n}\,\mathrm{d}n & + & \mathbb{J}_{\phi p}\,\mathrm{d}p & = -\mathbf{Z}_{\phi} \\ 0 & + & 0 & + & \mathbb{J}_{n\phi}\,\mathrm{d}\phi & + & \mathbb{J}_{nn}\,\mathrm{d}n & + & \mathbb{J}_{np}\,\mathrm{d}p & = -\mathbf{Z}_{n} \\ 0 & + & 0 & + & \mathbb{J}_{p\phi}\,\mathrm{d}\phi & + & \mathbb{J}_{pn}\,\mathrm{d}n & + & \mathbb{J}_{pp}\,\mathrm{d}p & = -\mathbf{Z}_{p} \end{cases} \tag{7.5}$$

It seems then natural to couple the circuit and current equations with the block corresponding to Poisson's equation, in order to minimize the nonzero extra–diagonal blocks. We will refer to this strategy of coupling the circuit with Poisson equation as (CCP-BGS):

$$\begin{cases} \mathbb{J}_{\mathbf{ww}}\,\mathrm{d}\mathbf{w}^{[s+1]} & + & \mathbb{J}_{\mathbf{wi}}\,\mathrm{d}\mathbf{i}^{[s+1]} & + & 0 & + & 0 & + & 0 & = -\mathbf{Z}_{\mathbf{w}} \\ 0 & + & \mathbb{J}_{\mathbf{ii}}\,\mathrm{d}\mathbf{i}^{[s+1]} & + & \mathbb{J}_{\mathbf{i}\phi}\,\mathrm{d}\phi^{[s+1]} & + & \mathbb{J}_{\mathbf{i}n}\,\mathrm{d}n^{[s]} & + & \mathbb{J}_{\mathbf{i}p}\,\mathrm{d}p^{[s]} & = -\mathbf{Z}_{\mathbf{i}} \\ \mathbb{J}_{\phi\mathbf{w}}\,\mathrm{d}\mathbf{w}^{[s+1]} & + & 0 & + & \mathbb{J}_{\phi\phi}\,\mathrm{d}\phi^{[s+1]} & + & \mathbb{J}_{\phi n}\,\mathrm{d}n^{[s]} & + & \mathbb{J}_{\phi p}\,\mathrm{d}p^{[s]} & = -\mathbf{Z}_{\phi} \\ 0 & + & 0 & + & \mathbb{J}_{n\phi}\,\mathrm{d}\phi^{[s+1]} & + & \mathbb{J}_{nn}\,\mathrm{d}n^{[s+1]} & + & \mathbb{J}_{np}\,\mathrm{d}p^{[s]} & = -\mathbf{Z}_{n} \\ 0 & + & 0 & + & \mathbb{J}_{p\phi}\,\mathrm{d}\phi^{[s+1]} & + & \mathbb{J}_{pn}\,\mathrm{d}n^{[s+1]} & + & \mathbb{J}_{pp}\,\mathrm{d}p^{[s+1]} & = -\mathbf{Z}_{p} \end{cases} \tag{CCP-BGS}$$

With this approach, instead of the $\mathbb{J}_{\phi\phi}$ block, an enriched block comprising the circuit equations is solved in first place at every block Gauß–Seidel iteration. As the external circuit presents normally a much smaller number of degrees of freedom than the discretized potential, also the size of the *LU* factors for this enriched block is similar to the size for standard BGS.

A similar approach, which would maintain the balance between the three blocks, is inspired to the *device–driven simulation* approach, hence it will be called (DDS-BGS). The equations stemming from the external circuit are eliminated, through static condensation, and the Jacobian in the standard BGS is replaced by its Schur complement. If we cluster together the blocks related to $\mathbf{w}$ and $\mathbf{i}$, we have

$$\begin{bmatrix} \mathrm{d}\mathbf{w} \\ \mathrm{d}\mathbf{i} \end{bmatrix} = - \begin{bmatrix} \mathbb{J}_{\mathbf{ww}} & \mathbb{J}_{\mathbf{wi}} \\ 0 & \mathbb{J}_{\mathbf{ii}} \end{bmatrix}^{-1} \begin{bmatrix} \mathbf{Z}_{\mathbf{w}} \\ \mathbf{Z}_{\mathbf{i}} + \mathbb{J}_{\mathbf{i}\phi}\,\mathrm{d}\phi + \mathbb{J}_{\mathbf{i}n}\,\mathrm{d}n + \mathbb{J}_{\mathbf{i}p}\,\mathrm{d}p \end{bmatrix} \tag{DDS-BGS.a}$$

which yields, if $\mathbb{J}_{\mathbf{ww}}$ is nonsingular,

$$\begin{aligned} \mathrm{d}\mathbf{i} &= -\mathbf{Z}_{\mathbf{i}} - \mathbb{J}_{\mathbf{i}\phi}\,\mathrm{d}\phi - \mathbb{J}_{\mathbf{i}n}\,\mathrm{d}n - \mathbb{J}_{\mathbf{i}p}\,\mathrm{d}p \\ \mathrm{d}\mathbf{w} &= \underbrace{-\mathbb{J}_{\mathbf{ww}}^{-1}(\mathbf{Z}_{\mathbf{w}} - A_{M+1}\mathbf{Z}_{\mathbf{i}})}_{\mathbf{Z}_{\mathbf{w}}^{*}} + \underbrace{\mathbb{J}_{\mathbf{ww}}^{-1}A_{M+1}(\mathbb{J}_{\mathbf{i}\phi}\,\mathrm{d}\phi + \mathbb{J}_{\mathbf{i}n}\,\mathrm{d}n + \mathbb{J}_{\mathbf{i}p}\,\mathrm{d}p)}_{\mathbb{J}_{\mathbf{w}\phi}^{*},\mathbb{J}_{\mathbf{w}n}^{*},\mathbb{J}_{\mathbf{w}p}^{*}} \end{aligned}$$

and in turn by plugging everything in the device blocks:

$$\begin{cases} \widetilde{\mathbb{J}}_{\phi\phi}\,\mathrm{d}\phi^{[s+1]} + \widetilde{\mathbb{J}}_{\phi n}\,\mathrm{d}n^{[s]} + \widetilde{\mathbb{J}}_{\phi p}\,\mathrm{d}p^{[s]} = -\widetilde{\mathbf{Z}}_{\phi} \\ \mathbb{J}_{n\phi}\,\mathrm{d}\phi^{[s+1]} + \mathbb{J}_{nn}\,\mathrm{d}n^{[s+1]} + \mathbb{J}_{np}\,\mathrm{d}p^{[s]} = -\mathbf{Z}_{n} \\ \mathbb{J}_{p\phi}\,\mathrm{d}\phi^{[s+1]} + \mathbb{J}_{pn}\,\mathrm{d}n^{[s+1]} + \mathbb{J}_{pp}\,\mathrm{d}p^{[s+1]} = -\mathbf{Z}_{p} \end{cases} \tag{DDS-BGS.b}$$

where the modified source is $\widetilde{\mathbf{Z}}_{\phi} = \mathbf{Z}_{\phi} - \mathbb{J}_{\phi\mathbf{w}}\mathbf{Z}_{\mathbf{w}}^{*}$, and the Schur complements are given as $\widetilde{\mathbb{J}}_{\phi\alpha} = \mathbb{J}_{\phi\mathbf{w}}\mathbb{J}_{\mathbf{w}\alpha}^{*} = \mathbb{J}_{\phi\mathbf{w}}\mathbb{J}_{\mathbf{ww}}^{-1}A_{M+1}\mathbb{J}_{\mathbf{i}\alpha}$ for $\alpha = \phi, n, p$. The increments in current and circuit variables are recovered after the iterations, exploiting (DDS-BGS.a). Differently from (CCP-BGS), the blocks in (DDS-BGS.b) all maintain the original dimensions. Thanks to the structure of $\mathbb{J}_{\phi\mathbf{w}}$, the static condensation results in transforming the boundary conditions imposed on the electric potential increment to Robin type.

Finally, the *circuit–driven simulation* approach (CDS-BGS) consists in the static condensation of the device block, rather than the circuit block. It grants the possibility of using the standard BGS algorithm on one hand, but on the other hand, the bulk of the system needs to be solved for more than once. In fact, in the circuit-currents block

$$\begin{bmatrix} \mathbb{J}_{\mathbf{ww}} & \mathbb{J}_{\mathbf{wi}} \\ 0 & \mathbb{J}_{\mathbf{ii}} \end{bmatrix} \begin{bmatrix} \mathrm{d}\mathbf{w} \\ \mathrm{d}\mathbf{i} \end{bmatrix} = - \begin{bmatrix} \mathbf{Z}_{\mathbf{w}} \\ \mathbf{Z}_{\mathbf{i}} + \mathbb{J}_{\mathbf{i}\phi}\,\mathrm{d}\phi(\mathrm{d}\mathbf{w}) + \mathbb{J}_{\mathbf{i}n}\,\mathrm{d}n(\mathrm{d}\mathbf{w}) + \mathbb{J}_{\mathbf{i}p}\,\mathrm{d}p(\mathrm{d}\mathbf{w}) \end{bmatrix} \tag{DDS-BGS.a}$$

the relations $\mathrm{d}\alpha(\mathrm{d}\mathbf{w})$ need to be made explicit, meaning the system needs to be complemented with the following:

$$\begin{bmatrix} \mathrm{d}\phi \\ \mathrm{d}n \\ \mathrm{d}p \end{bmatrix} = - \underbrace{\begin{bmatrix} \mathbb{J}_{\phi\phi} & \mathbb{J}_{\phi n} & \mathbb{J}_{\phi p} \\ \mathbb{J}_{n\phi} & \mathbb{J}_{nn} & \mathbb{J}_{np} \\ \mathbb{J}_{p\phi} & \mathbb{J}_{pn} & \mathbb{J}_{pp} \end{bmatrix}^{-1}}_{\mathbb{J}_{[\phi,n,p][\phi,n,p]}} \left(\begin{bmatrix} \mathbf{Z}_{\phi} \\ \mathbf{Z}_{n} \\ \mathbf{Z}_{p} \end{bmatrix} + \begin{bmatrix} \mathbb{J}_{\phi\mathbf{w}} \\ 0 \\ 0 \end{bmatrix} \mathrm{d}\mathbf{w} \right) \tag{CDS-BGS.b}$$

The relations in (CDS-BGS.b) are implicit, but the BGS algorithm can be used to approximate the estimated increment

$$\begin{bmatrix} \widetilde{\mathrm{d}\phi} \\ \widetilde{\mathrm{d}n} \\ \widetilde{\mathrm{d}p} \end{bmatrix} = -\mathbb{J}^{-1}_{[\phi,n,p][\phi,n,p]} \begin{bmatrix} \mathbf{Z}_\phi \\ \mathbf{Z}_n \\ \mathbf{Z}_p \end{bmatrix} \tag{7.8}$$

as well as the response to the boundary conditions

$$\mathbb{G}_{[\phi,n,p]\mathbf{w}} = -\mathbb{J}^{-1}_{[\phi,n,p][\phi,n,p]} \begin{bmatrix} \mathbb{J}_{\phi\mathbf{w}} \\ 0 \\ 0 \end{bmatrix}. \tag{7.9}$$

It is worth noting that:

- (7.9) involves a limited BGS applications, as only the columns of $\mathbb{J}_{\phi\mathbf{w}}$ corresponding to a pin potential contain nonzero coefficients;
- as $\mathbb{G}_{[\phi,n,p]\mathbf{w}}$ only depends on the Jacobian blocks, it can be reused when a modified Newton method is employed;
- also when the Jacobian is recomputed, as the right hand side on (7.9) does not vary, the latest computation often provides a good initial guess for the BGS iterations.

Once $\mathbb{G}_{[\phi,n,p]}$ and the estimated increments are computed, they can be plugged back in (DDS-BGS.a), to obtain the condensed system:

$$\begin{bmatrix} \mathbb{J}_{\mathbf{ww}} & \mathbb{J}_{\mathbf{wi}} \\ \mathbb{J}_{\mathbf{i}[\phi,n,p]}\mathbb{G}_{[\phi,n,p]\mathbf{w}} & \mathbb{J}_{\mathbf{ii}} \end{bmatrix} \begin{bmatrix} \mathrm{d}\mathbf{w} \\ \mathrm{d}\mathbf{i} \end{bmatrix} = - \begin{bmatrix} \mathbf{Z}_{\mathbf{w}} \\ \mathbf{Z}_{\mathbf{i}} + \mathbb{J}_{\mathbf{i}[\phi,n,p]} \left[\widetilde{\mathrm{d}\phi}, \widetilde{\mathrm{d}n}, \widetilde{\mathrm{d}p}\right]^T \end{bmatrix} \tag{7.10}$$

The linear system in (7.10) is normally small, and can be solved directly. The resulting circuital increment $\mathrm{d}\mathbf{w}$ is finally employed in (CDS-BGS.b) in order to obtain the corrected increment.

The three presented approaches to coupling the block Gauß–Seidel algorithm with the circuital equations have been tested on a simple benchmark: a (distributed) power diode controlled by a voltage source through a (lumped) resistor. Figure 7.4 shows the variations in the spectral radius at equilibrium when the resistance is changed. As can be seen from the graph, the first and second approach highlight a “resonance” effect in a very similar fashion, and the spectral radius grows to be greater than unity. On the contrary, the latest presented method, (CDS-BGS), besides being in principle computationally more demanding, is always stable with a very low spectral radius. We thus conclude with (CDS-BGS) as our method of choice, to which we will refer in the following simply as BGS.

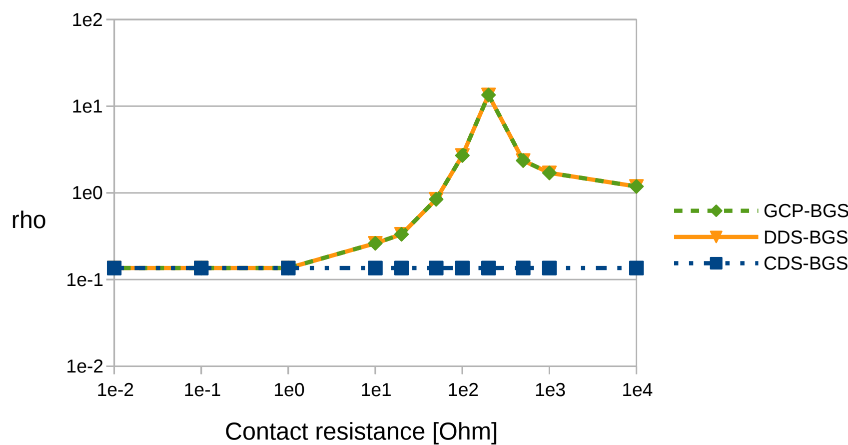

Figure 7.4.: Spectral radius in equilibrium conditions, for different coupling paradigms.

References

[1] J. E. Dennis and Jorge J Moré. "A characterization of superlinear convergence and its application to quasi-Newton methods". In: *Mathematics of computation* 28.126 (1974), pp. 549–560. DOI: 10.1090/S0025-5718-1974-0343581-1.

[2] J. E. Dennis and Jorge J. Moré. "Quasi-Newton Methods, Motivation and Theory". In: *SIAM Review* 19.1 (1977), pp. 46–89. DOI: 10.1137/1019005.

[3] R.E. Bank and D.J. Rose. "Global approximate Newton methods". English. In: *Numerische Mathematik* 37.2 (1981), pp. 279–295. ISSN: 0029-599X. DOI: 10.1007/BF01398257.

[4] A.N Brooks and T.J.R. Hughes. "Streamline upwind/Petrov-Galerkin formulation for convection dominated flows with particular emphasis on the incompressible Navier-Stokes equation". In: *Computer methods in applied mechanism and engineering* 32 (1982), pp. 199–259.

[5] C. Jhonson. "Numerical solution of partial differential equations by the finite element method". In: *Cambridge university press Cambrige* 32 (1987).

[6] R.E. Bank, J.F. Burgler, et al. "Some upwinding techniques for finite element approximations of convection-diffusion equation". In: *Numerische Mathematik* 58(1) (1990), pp. 185–202.

[7] J. D. Lambert. *Numerical Methods for Ordinary Differential Systems: The Initial Value Problem*. 1st ed. Wiley, 1991, p. 304. ISBN: 978-0-471-92990-1.

[8] J.W. Jerome. *Analysis of Charge Transport*. Berlin Heidelberg: Springer-Verlag, 1996.

[9] Randolph E. Bank, Jr. W.M. Coughran, and Lawrence C. Cowsar. "The Finite Volume Scharfetter-Gummel method for steady convection diffusion equations". In: *Computing and Visualization in Science* 1 (3 1998), pp. 123–136. ISSN: 1432-9360. DOI: 10.1007/s007910050012.

[10] E. Gatti, S. Micheletti, and R. Sacco. "A new Galerkin framework for the drift-diffusion equation in semiconductors". In: *East West Journal of Numerical Mathematics* 6 (1998), pp. 101–136. ISSN: 0928-0200.

[11] Mario Putti and Christian Cordes. "Finite element approximation of the diffusion operator on tetrahedra". In: *SIAM Journal on Scientific Computing* 19.4 (1998), pp. 1154–1168.

[12] A. Sidi. "Extrapolation vs. projection methods for linear system of equations". In: *Journal of Computational and Applied Mathematics* 22 (1998), pp. 71–88.

[13] J. Xu and L. Zikatanov. "A monotone finit element scheme for convenction-diffusion equations". In: *Math. Comp.* 68 (1999), pp. 1429–1446.

[14] Diana Estévez Schwarz and Caren Tischendorf. "Structural analysis of electric circuits and consequences for MNA". In: *International Journal of Circuit Theory and Applications* 28 (2000), pp. 131–162.

[15] Roswitha März, Diana Estv́ez Schwarz, et al. "Finding Beneficial DAE Structures in Circuit Simulation". In: *Mathematics — Key Technology for the Future*. Ed. by Willi Jäger and Hans-Joachim Krebs. Springer Berlin Heidelberg, 2003, pp. 413–428. ISBN: 978-3-642-62914-3. DOI: 10.1007/978-3-642-55753-8_34.

[16] Caren Tischendorf. "Coupled systems of differential algebraic and partial differential equations in circuit and device simulation. Modeling and numerical analysis". Habilitationsschrift. Humboldt-Univ. zu Berlin, 2004.

[17] F. Brezzi, L.D. Marini, et al. "Discretization of Semiconductor Device Problems (I)". In: *Numerical Methods in Electromagnetics*. Vol. 13. Handbook of Numerical Analysis. Elsevier, 2005, pp. 317–441. DOI: 10.1016/S1570-8659(04)13004-4.

[18] A.J.H. Wachters and W.H.A. Schilders. "Simulation of EMC Behaviour". In: *Numerical Methods in Electromagnetics*. Vol. 13. Handbook of Numerical Analysis. Elsevier, 2005, pp. 661–753. DOI: 10.1016/S1570-8659(04)13007-X.

[19] A. Quarteroni. *Modellistica numerica per problemi differenziali*. Springer, 2006. ISBN: 88-470-0493-4.

[20] A. Quarteroni, R. Sacco, and F. Saleri. *Numerical Mathematics*. 2nd Edition. Springer - Applied mathematics. Springer-Verlag, 2006.

[21] *Wikipedia*. 2013. URL: https://it.wikipedia.org (visited on 2013).

[22] A. J. Wathen. "Preconditioning". In: *Acta Numerica* 24 (May 2015), pp. 329–376. ISSN: 1474-0508. DOI: 10.1017/S0962492915000021.

Part III.

Test cases

8. Validation of the Physical Models

In order to check and calibrate the physical models described in chapter 2, some simulations on very simple devices were run. As the many necessary experimental data are difficult to source, our results were compared with simulations performed with a commercial semiconductor simulator, Sentaurus Device, which is among the most widespread software tool for simulation of semiconductor devices.

8.1. Band gap narrowing model

In the following, we will calibrate the band gap narrowing model, allowing an accurate reproduction of the carrier densities inside the device. To calibrate the model, we examined a silicon resistor with a longitudinal doping profile (uniform over the device section). The simulated structure is an abstraction and is not linked to a realistic device, but it allows us to isolate the physical effects we aim to investigate.

The n type doping profile is built with a Gaussian shape, and shown in figure 8.1. The device dimensions are $(1 \times 1 \times 50)\,\mu$m.

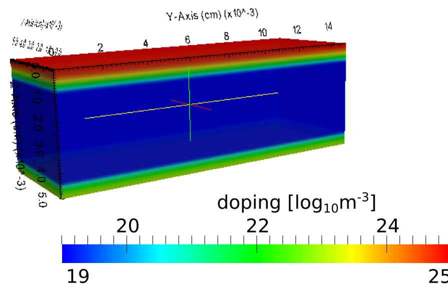

Figure 8.1.: Net doping profile ($N_{\mathrm{bi}} = N_{\mathrm{D}} - N_{\mathrm{A}}$) for the investigated resistor.

To calibrate the band gap narrowing model of section 2.2.1, it suffices to analyze charge density in equilibrium conditions. Estimation of the carriers densities with values of N_{i} taken from literature leads to incorrect minority carrier approximation, as shown in figures 8.2 and 8.3. Figure 8.3 shows how electron density is correctly reproduced, as its value is driven by the doping profile: $n \simeq N_{\mathrm{D}}$. Holes density

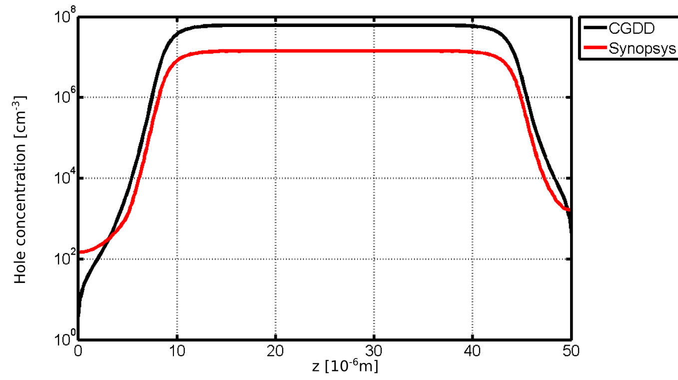

Figure 8.2.: Holes density along z axis, with uniform N_{i}.

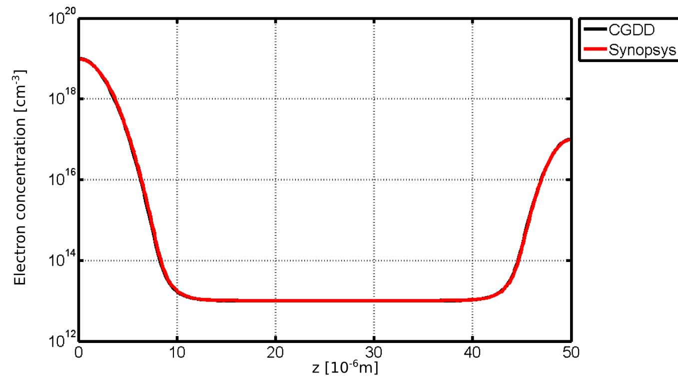

Figure 8.3.: Electron density along z axis, with uniform N_{i}.

from figure 8.2 is instead unrelated to the reference value. Differences in the central portion can be ascribed to differences in the base N_{i} value, while at the edges, effects of high doping density need to be accounted for.

Enforcing a base value for N_{i} of $1.29419510402271 \times 10^{16}\,\mathrm{m}^{-3}$ and using the band gap narrowing model of section 2.2.1, provides the correct estimate for the minority carriers as shown in figures 8.4 and 8.5.

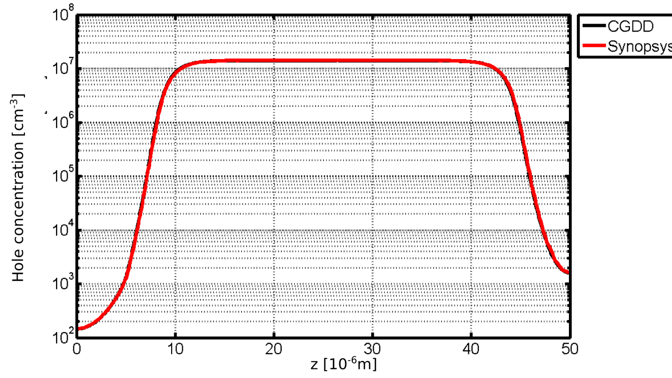

Figure 8.4.: Holes density along z axis, with band gap narrowing model.

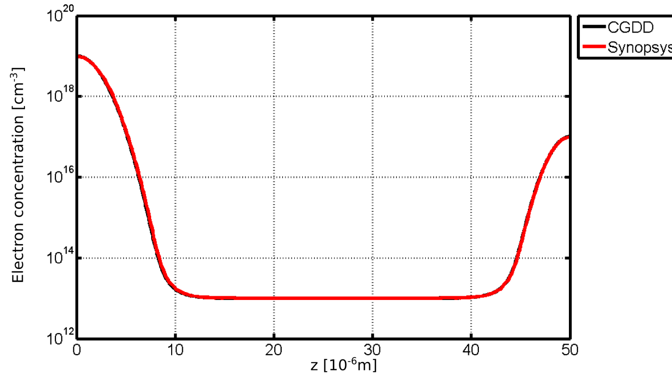

Figure 8.5.: Electron density along z axis, with band gap narrowing model.

8.2. Carrier lifetimes model

Once calibrated the band gap narrowing model, correct carriers densities are available in the stationary case. Other parameters independent on bias conditions but only on the total doping concentrations are the carriers lifetime. To calibrate the lifetimes models of section 2.2.3, we employ once again the Gaussian resistor.

A first model implemented in our code came from [2], and describes lifetimes as:

$$\tau_n = \frac{\tau_{n0}}{1 + \left(\frac{N_{\mathrm{A}}}{N_{\mathrm{ref}}}\right)} \qquad \tau_p = \frac{\tau_{p0}}{1 + \left(\frac{N_{\mathrm{D}}}{N_{\mathrm{ref}}}\right)} \tag{8.1}$$

with $\tau_{n0} 30 \times 10^{-6}\,\mathrm{s}$, $\tau_{p0} 10 \times 10^{-6}\,\mathrm{s}$, and $N_{\mathrm{ref}} = 10^{23}\,\mathrm{m}^{-3}$. A stationary simulation with the model from (8.1), resulted in the graphs of figure 8.6 and 8.7.

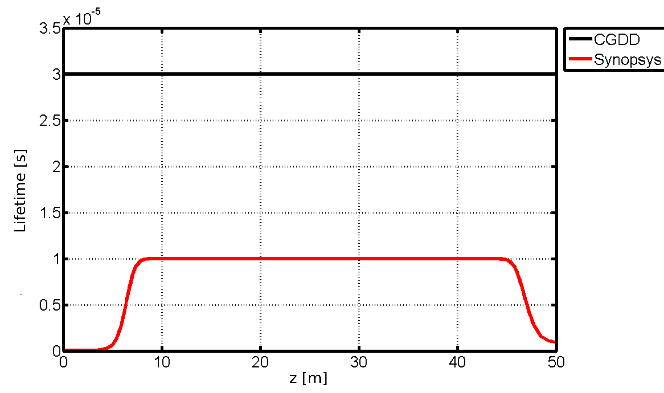

Figure 8.6.: Electrons lifetimes along z axis, with the model from (8.1).

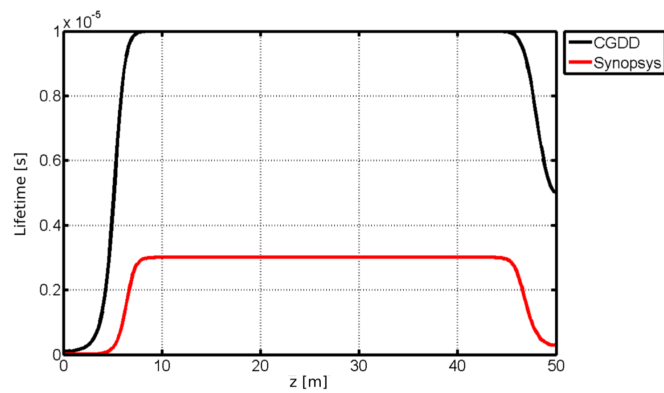

Figure 8.7.: Holes lifetimes along z axis, with the model from (8.1).

Successively, the model exposed in section 2.2.3 brought to the correct estimation of lifetimes as per figure 8.8 and 8.9.

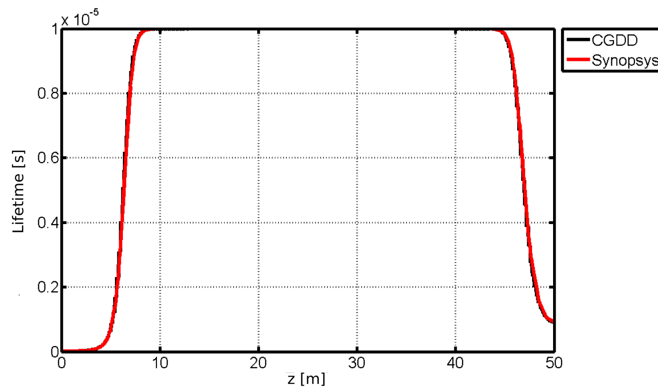

Figure 8.8.: Electrons lifetimes along z axis, with the model from section 2.2.3.

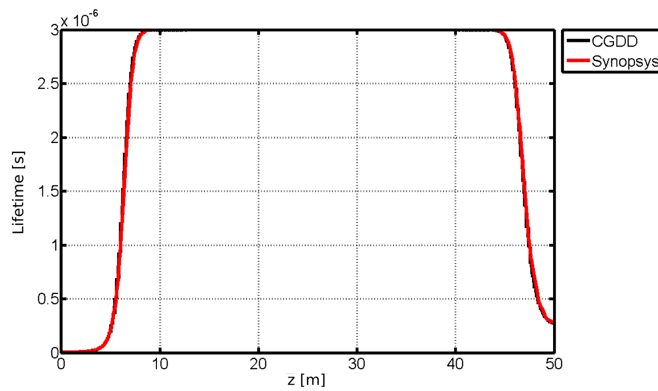

Figure 8.9.: Holes lifetimes along z axis, with the model from section 2.2.3.

8.3. Mobility models

In the following section we will compare the results obtained with the Philips unified mobility model which is implemented in our code, with the results from Sentaurus Device. We complete the Philips mobility with a velocity saturation model that relates the mobility to the electric field. To control the correctness of the model we analyze the carriers mobility inside the Gaussian resistor for a bias value of 100 V. We will also see how calibration was necessary to reach an exact evaluation of the model parameters.

The simulations were obtained by quasi–static ramping of the voltage, from 0 V to 100 V in 100s. A first simulation including parameters from scientific literature with Philips model provided the results of figure 8.10, 8.11.

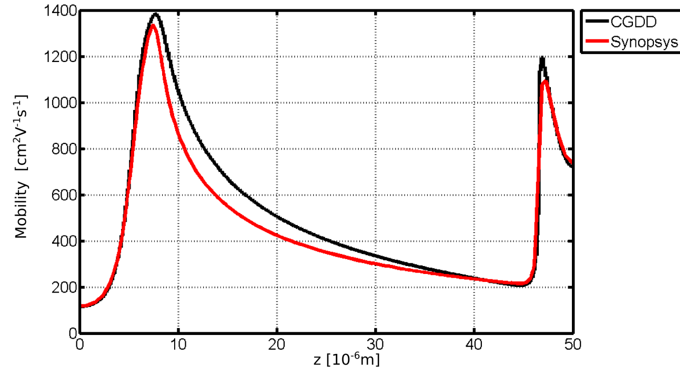

Figure 8.10.: Electrons mobility along z axis, literature parameters.

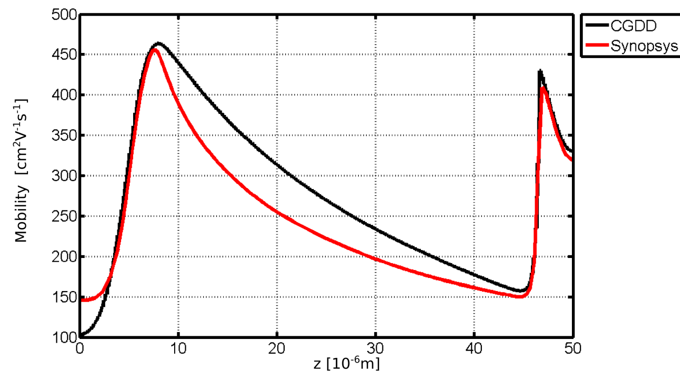

Figure 8.11.: Holes mobility along z axis, literature parameters.

It can be noticed how both holes and electrons mobilities do not match the reference in the central region of the device. Holes mobility is also mismatched near contacts. Successively, calibrating the model parameters, the results of figure 8.12 and 8.13 were recovered. The mismatch of near–contact regions is solved, and in general mobilities are reproduced with higher fidelity.

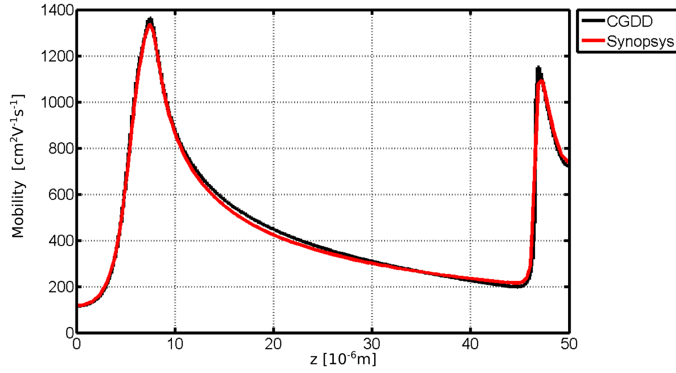

Figure 8.12.: Electrons mobility along z axis, calibrated parameters.

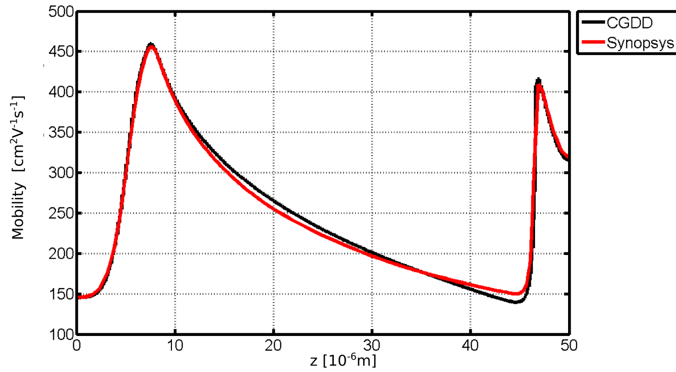

Figure 8.13.: Holes mobility along z axis, calibrated parameters.

8.4. Trap assisted generation–recombination

In this section we analyze the SRH generation–recombination model. The net recombination rate is compared with Sentaurus data on a simulation of the Gaussian resistor with 100 V applied voltage. A correct implementation of the carrier lifetimes model and of the band gap narrowing model is crucial for a correct estimation of R^{SRH}. Other mechanisms such as the impact ionization can be ignored given the low bias voltage.

It must be noted that, once the correct carrier lifetimes and equilibrium concentrations are correctly estimated, the trap assisted generation–recombination can vary only upon variation of the carrier densities, according to (SRH), which we

report here for the sake of convenience:

$$R^{\mathrm{SRH}} = \frac{np - N_{\mathrm{i,eff}}^2}{\tau_p \left[n + N_{\mathrm{i,eff}} \exp\left(\frac{E_{\mathrm{t}} - E_{\mathrm{i}}}{k_{\mathrm{B}} T} \right) \right] + \tau_n \left[p + N_{\mathrm{i,eff}} \exp\left(\frac{E_{\mathrm{i}} - E_{\mathrm{t}}}{k_{\mathrm{B}} T} \right) \right]}.$$

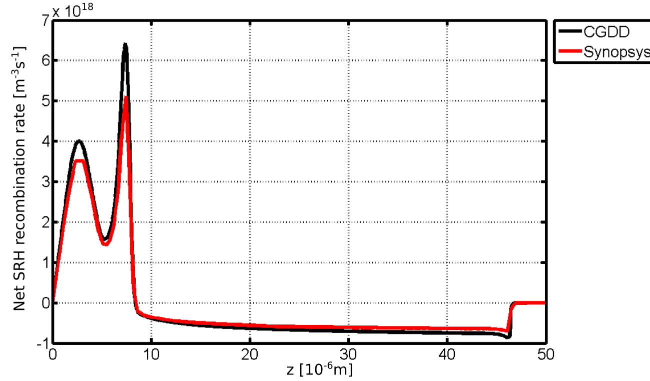

Figure 8.14.: Net SRH recombination rate on 100 V bias.

The small differences which can be noticed in figure 8.14 between computed and reference values are effectively negligible, and can be imputed to small differences in the computed carrier densities, due to the algorithmic differences between our code and the commercial software.

8.5. Impact ionization model

In order to test the impact ionization model we decided to simulate the reverse I-V characteristic of a *p*-*i*-*n* diode. The initially implemented model presented a power series approximation for the ionization coefficients. The simulations evidenced that this approximation introduced a non negligible error in the evaluation of the breakdown voltage, thus we decided to implement the model as described in chapter 2.

To test the model, we used a reverse bias characteristic simulation of the *p*-*i*-*n* represented in figure 8.15. For applied voltages below the V_{bd} threshold, the diode is in blocking regime, with a current near 0 A. Over the threshold, impact ionization is triggered and results in huge production of free carriers, which in turn generate high currents in the diode.

The simulation was performed in quasi–static conditions, adopting a voltage ramp growing from 0 V up to 700 V with variations of 1 V per second. At first, the model from [1] was employed for the coefficients of ionization α_n, α_p. Such

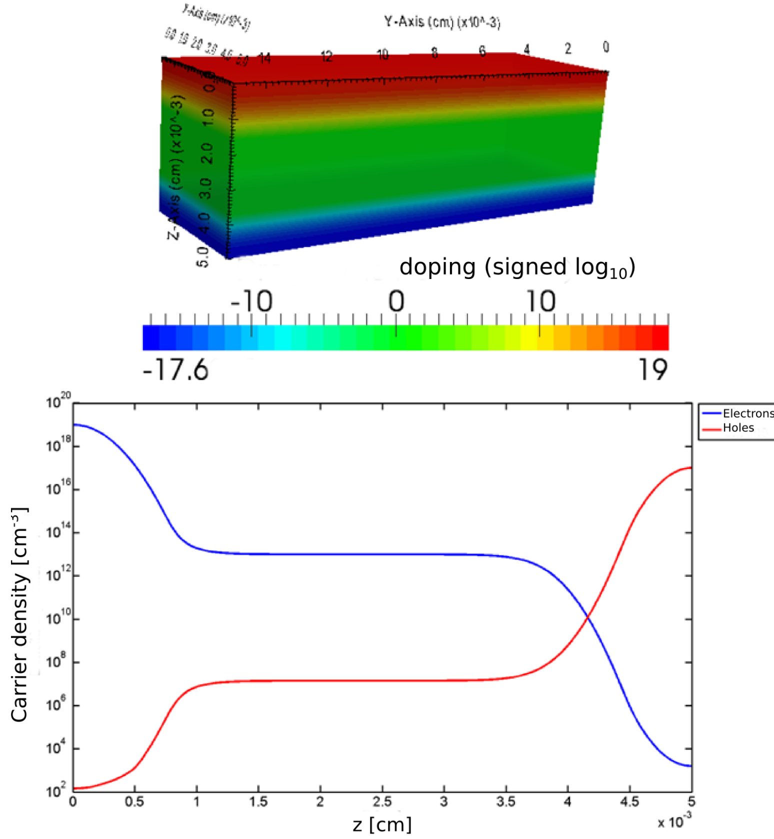

Figure 8.15.: Doping and carrier densities on the p-i-n diode along z axis

approximation, useful to derive an analytic estimate of V_{bd}, consists in expanding in power series the exponentials involved in the laws of α_n, α_p, reducing their expression to:

$$\alpha_n = \alpha_p = a_\alpha |\nabla \phi|^7 \tag{8.2}$$

with $a_\alpha = 1,8 \times 10^{-29}\,\mathrm{m}^6\mathrm{V}^{-7}$. Such approximation induces a generation of charge of

$$R^{\mathrm{II}} = a_\alpha |\nabla \phi|^7 (\vec{J}_n + \vec{J}_p) \tag{8.3}$$

Figure 8.16 compares reverse bias characteristics obtained with our simulator and with Sentaurus. We can notice a discrepance in the breakdown voltage threshold, which is around $-840\,\mathrm{V}$ in the produced simulations while at $-740\,\mathrm{V}$ in the reference simulations. In order to understand this mismatch, we analyzed the generation rates for electrons and holes at $-600\,\mathrm{V}$ reverse bias.

Figure 8.17 and 8.18 evidence the difference in the ionization rates between simulations and reference. Such mismatch can be considered depending both on the

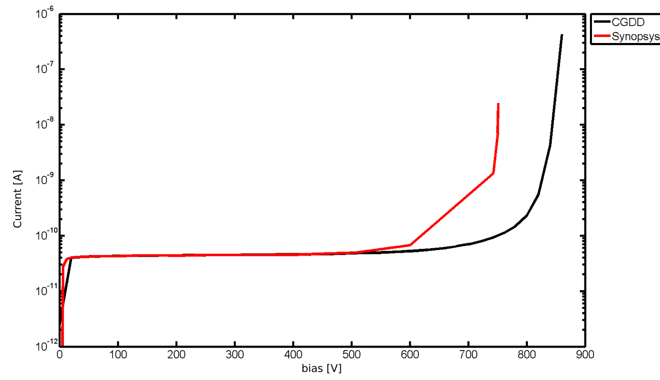

Figure 8.16.: Reverse bias characteristic of the *p*-*i*-*n* diode.

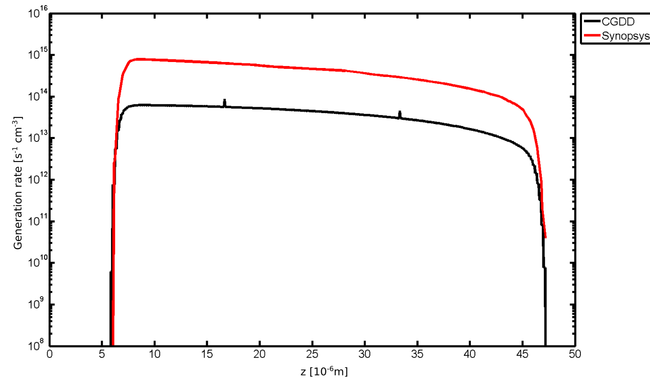

Figure 8.17.: Impact ionization generation rate for electrons, reduced model.

implemented model and on differences in the approximation of current densities, reported in figure 8.19 and 8.20. On the other hand, the electric field estimation in both reference and simulated cases is identical, as shown in figure 8.21.

To verify if the source of the error was imputable only to the approximated impact ionization model, a post–processing of the simulation output was performed, using the complete model presented in chapter 2. The resulting coefficients are compared with reference values in figure 8.22 and 8.23.

We could consider the hypothesis verified, as a marked improvement is evidenced in the post–processed curved. An implementation of the complete model was thus employed in a new simulation, reported in figure 8.24, figure 8.25 and figure 8.26. The correct breakdown voltage was obtained in this case.

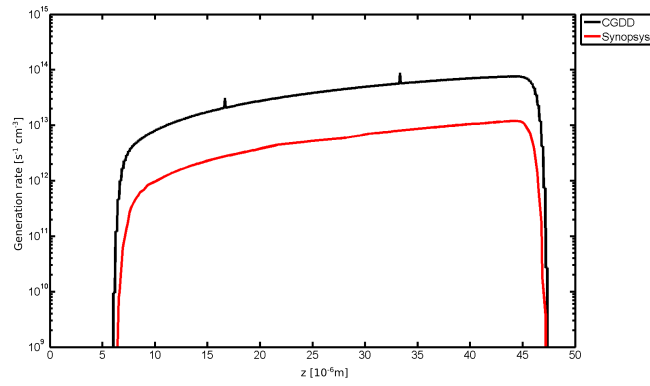

Figure 8.18.: Impact ionization generation rate for holes, reduced model.

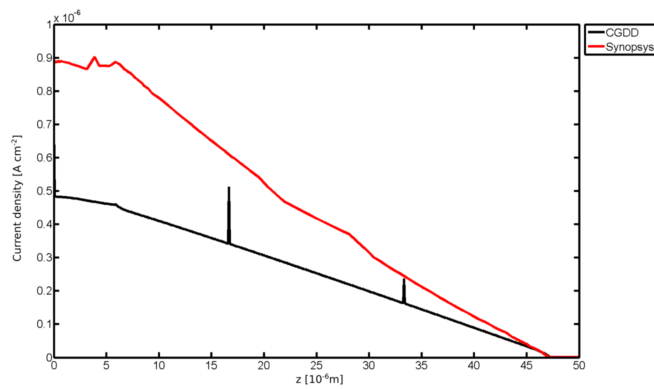

Figure 8.19.: Electron current density along z axis.

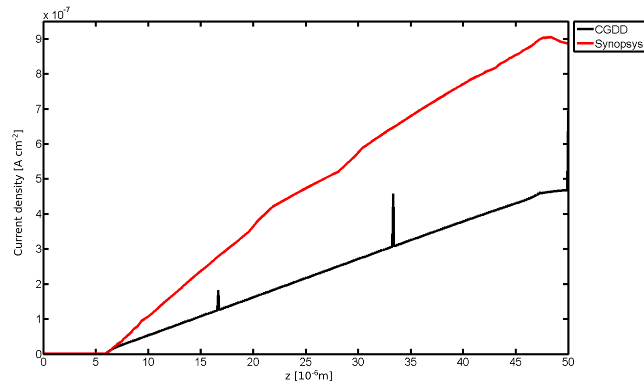

Figure 8.20.: Hole current density along z axis.

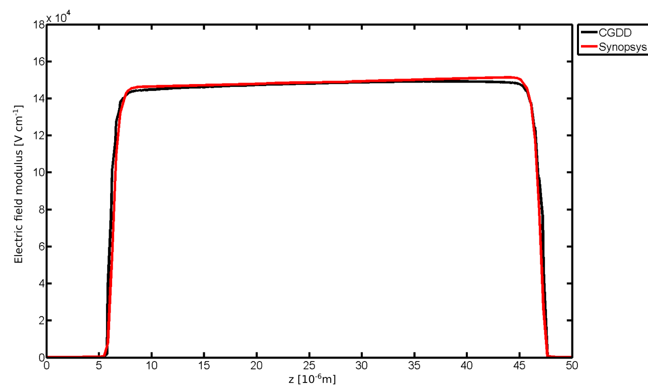

Figure 8.21.: Electric field strength along z axis.

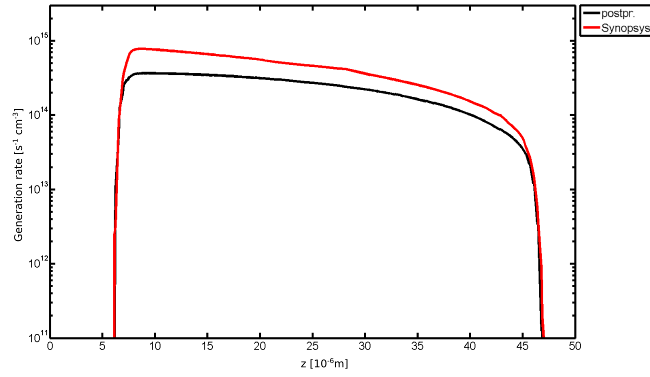

Figure 8.22.: Impact ionization generation rate for electrons, post–processed complete model.

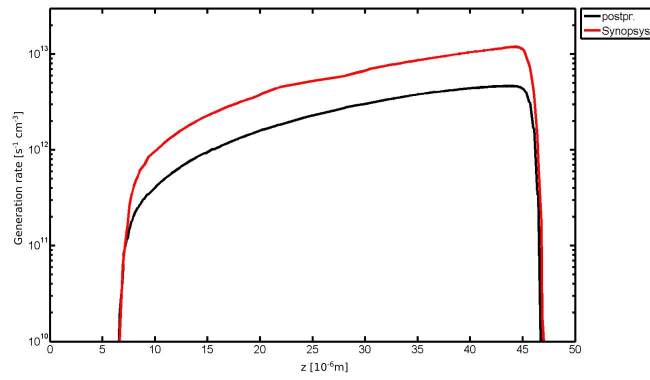

Figure 8.23.: Impact ionization generation rate for holes, post–processed complete model.

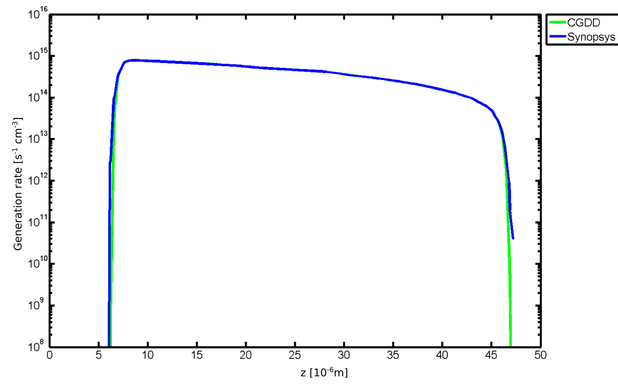

Figure 8.24.: Impact ionization generation rate for electrons, complete model.

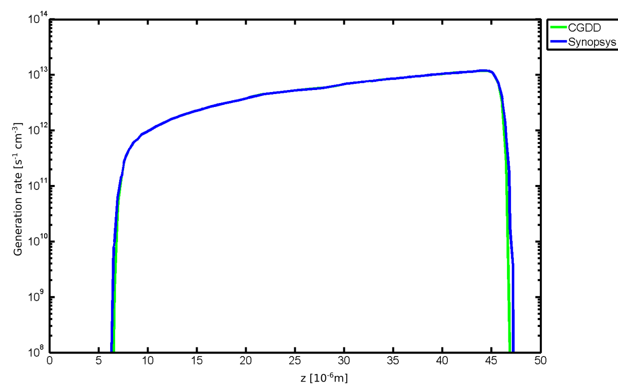

Figure 8.25.: Impact ionization generation rate for holes, complete model.

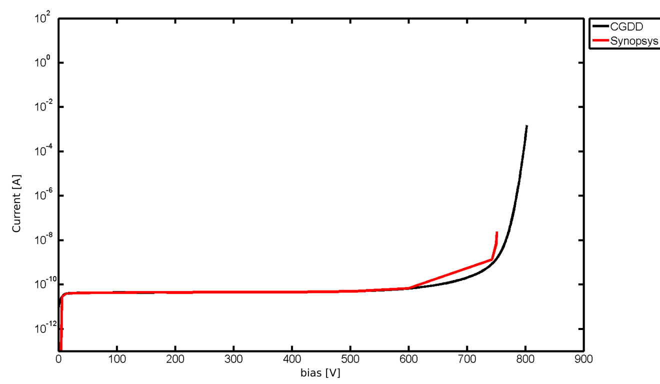

Figure 8.26.: Reverse bias characteristic for the *p*-*i*-*n* diode, complete impact ionization model

9. *p-i-n* Power Diode

9.1. Simulation in Quasi–static Regime

An investigation of quasi–static characteristics of the *p-i-n* diode of figure 8.15 has been performed. The reverse bias characteristic – which has already been discussed in chapter 8 – was obtained with a reverse bias ramp up to −830 V, and is reported in figure 9.1. The forward bias characteristic was studied with bias up to 4 V.

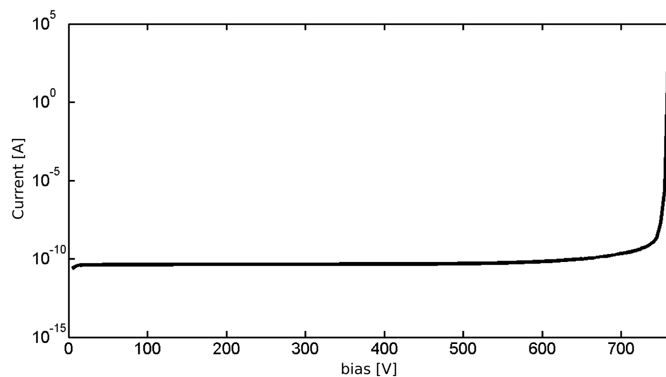

Figure 9.1.: Reverse bias characteristic

The high breakdown voltage (roughly 750 V) is obtained thanks to the drift region width w_{B} and its doping density. Such region sustains the most part of the applied voltage. The following relation:

$$V_{\mathrm{a}} \simeq |E_{\mathrm{d}}| w_B \tag{9.1}$$

where V_{a} is the applied voltage and $|E_{\mathrm{d}}|$, holds when the drift region is almost completely depleted, which happens for applied voltages bigger than the punch–through voltage, approximated as

$$V_{\mathrm{pt}} \simeq \frac{q N_{\mathrm{D}} w_{\mathrm{B}}^2}{2\varepsilon}. \tag{9.2}$$

As can be seen in figure 9.2, the punch–through occurs for our diode around the 38 V mark, and the electric field is almost uniform for higher bias, as shown in figure 9.3

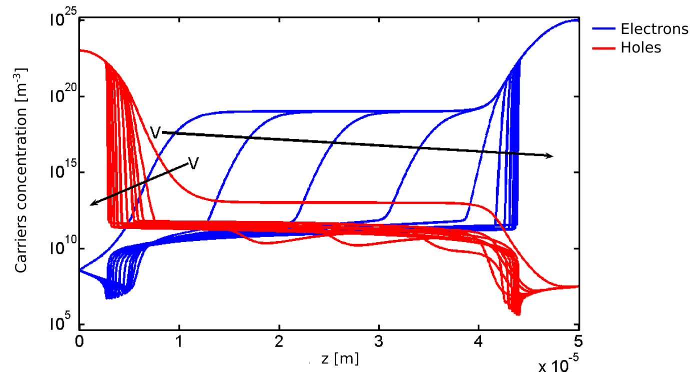

Figure 9.2.: Carrier densities in reverse bias, up to the punch–through.

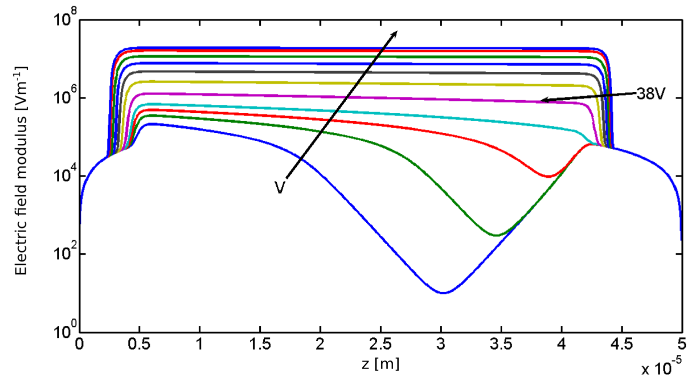

Figure 9.3.: Electric field trend in reverse bias.

As the bias approaches 750 V, the electric field grows sufficiently high, and the impact ionization is triggered, as shown in figure 9.4. Increasing w_B results in increased breakdown voltage, but also in higher on–state resistance. In direct bias regime, in fact, high injection of minority carriers in the drift region drives the device resistance making it independent of doping.

The forward bias characteristic is shown in figure 9.5: as the applied bias grows over 15 V, the saturation of current occurs around the 25 A mark. Mobility models are critical to this regard, as saturation depends on the limitation on carrier velocity, as shown in figure 9.6.

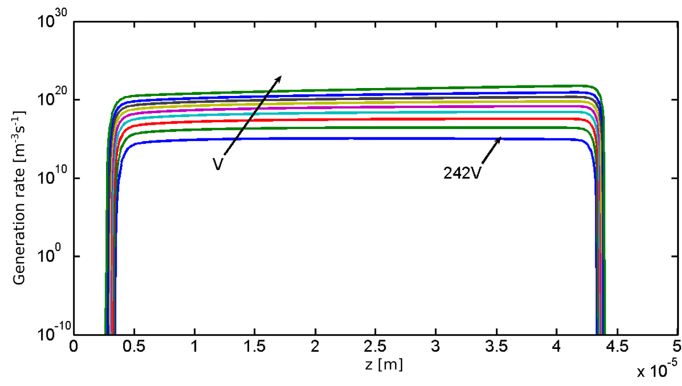

Figure 9.4.: Generation rate from impact ionization.

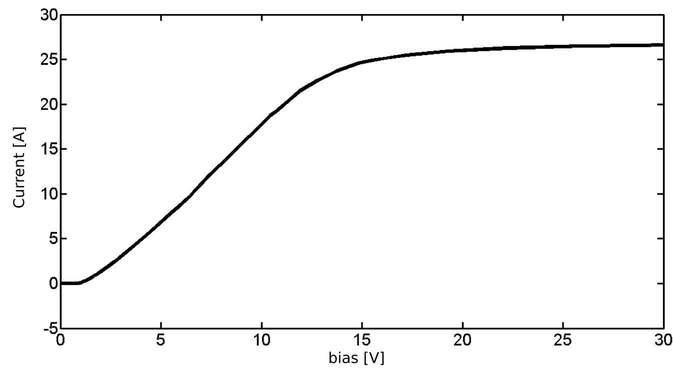

Figure 9.5.: Forward bias characteristic.

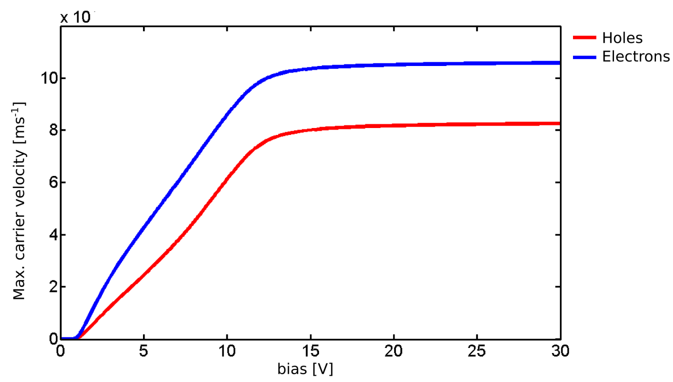

Figure 9.6.: Velocity saturation

9.2. Simulation in AC Regime

A power diode biased with a sinusoidal voltage source has been used as a test bench for the algorithm development, the reason being it presents several of the defining characteristics of power devices, and ranges over most regimes (conduction, depletion, switching, etc.). The three main static regimes are shown in figures 9.7 9.8, and 9.9.

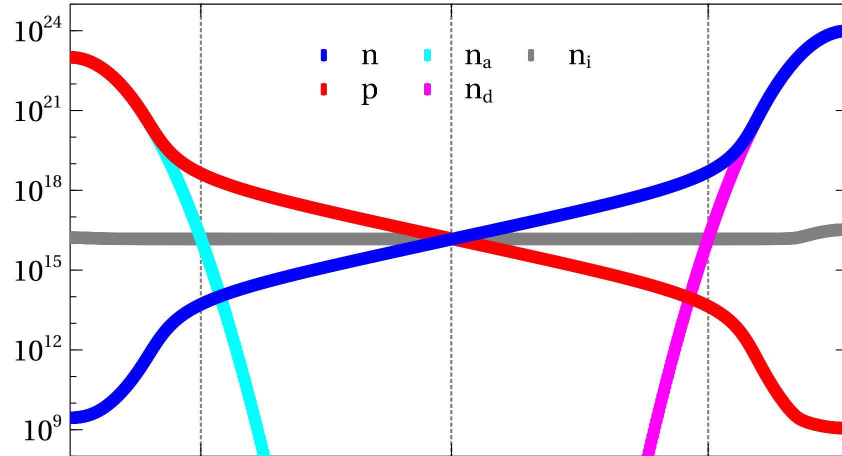

Figure 9.7.: Carrier densities in a *p-i-n* diode at thermal equilibrium. The device doping follows a “textbook” gaussian profile.

Figures 9.10, 9.11, and 9.12 show how the parameter λ influences the convergence properties. However, adaptive time stepping provides a way to recover the convergence for the BGS method.

Figures 9.13 and 9.14 compare the spectral radii and the time stepping directly. The deterioration of the convergence in reverse bias conditions with vanishing λ can be appreciated in the former, while the need to dampen the time step to obtain convergence in forward bias is evident in the latter.

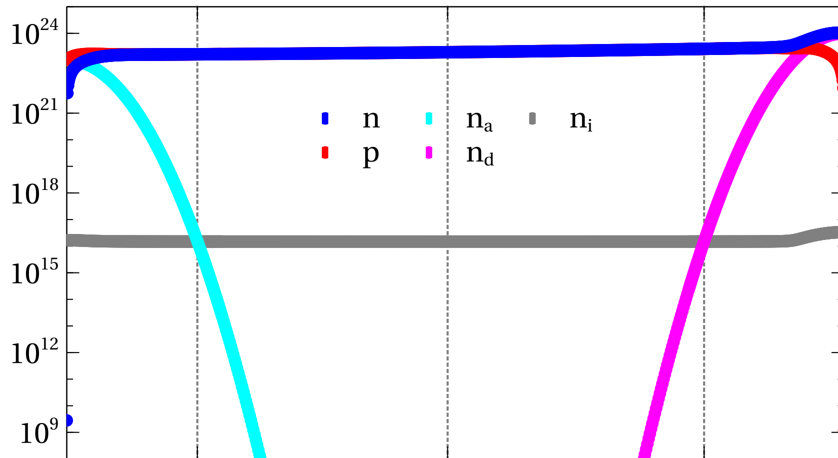

Figure 9.8.: Carrier densities in a *p*-*i*-*n* diode in forward bias. The device doping follows a “textbook” gaussian profile.

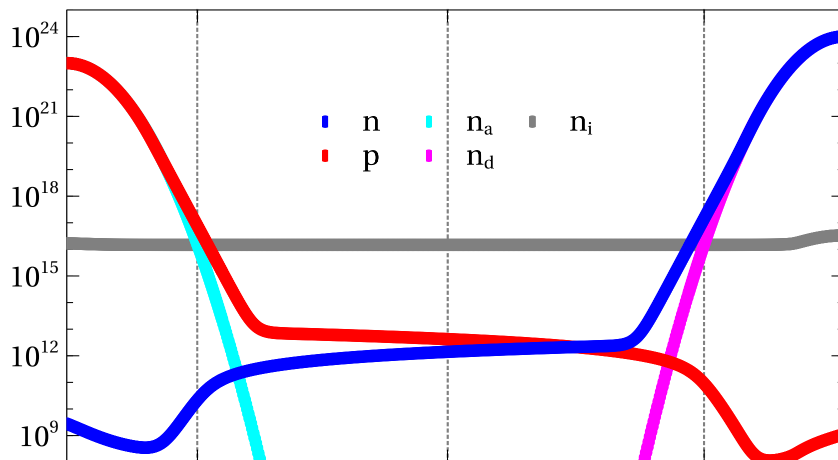

Figure 9.9.: Carrier densities in a *p*-*i*-*n* diode in reverse bias. The device doping follows a “textbook” gaussian profile.

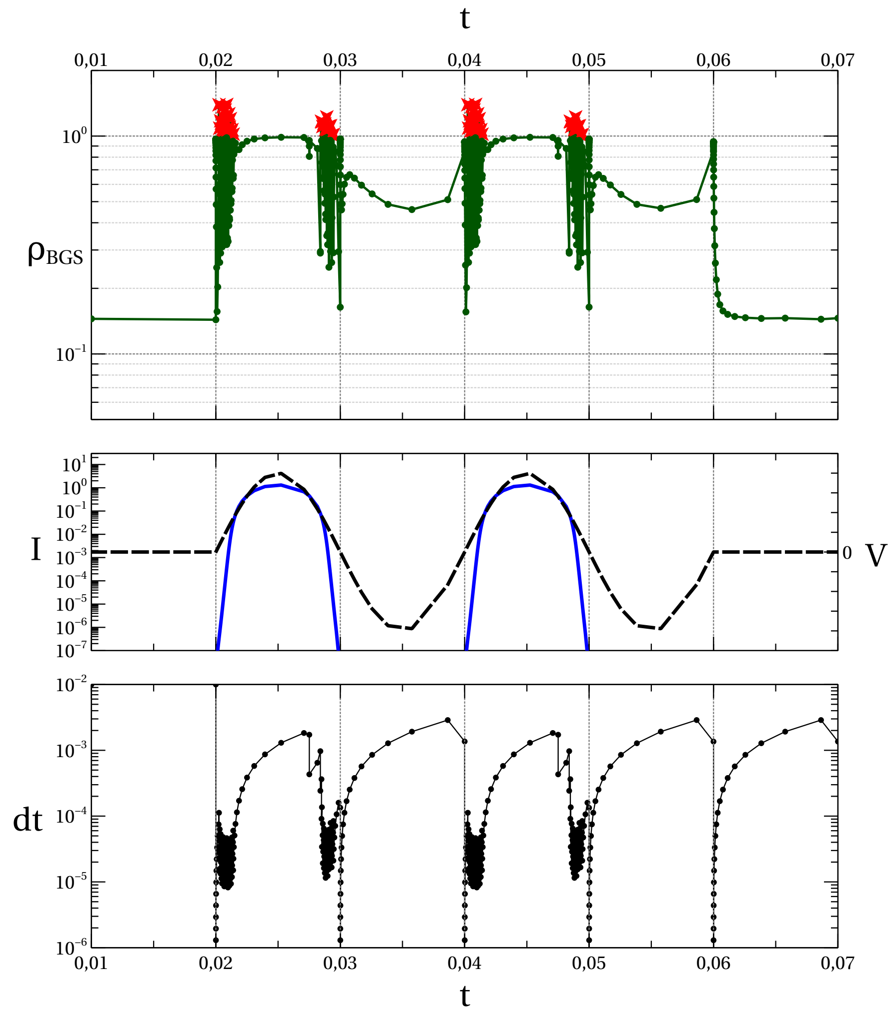

Figure 9.10.: Full simulation for the diode with $\lambda = 10^{-5}$. Top: spectral radius for the Block Gauß–Seidel method (green, red stars point out the values over unity); center: voltage (black dashed line) and forward current (blue); bottom: adapted time steps.

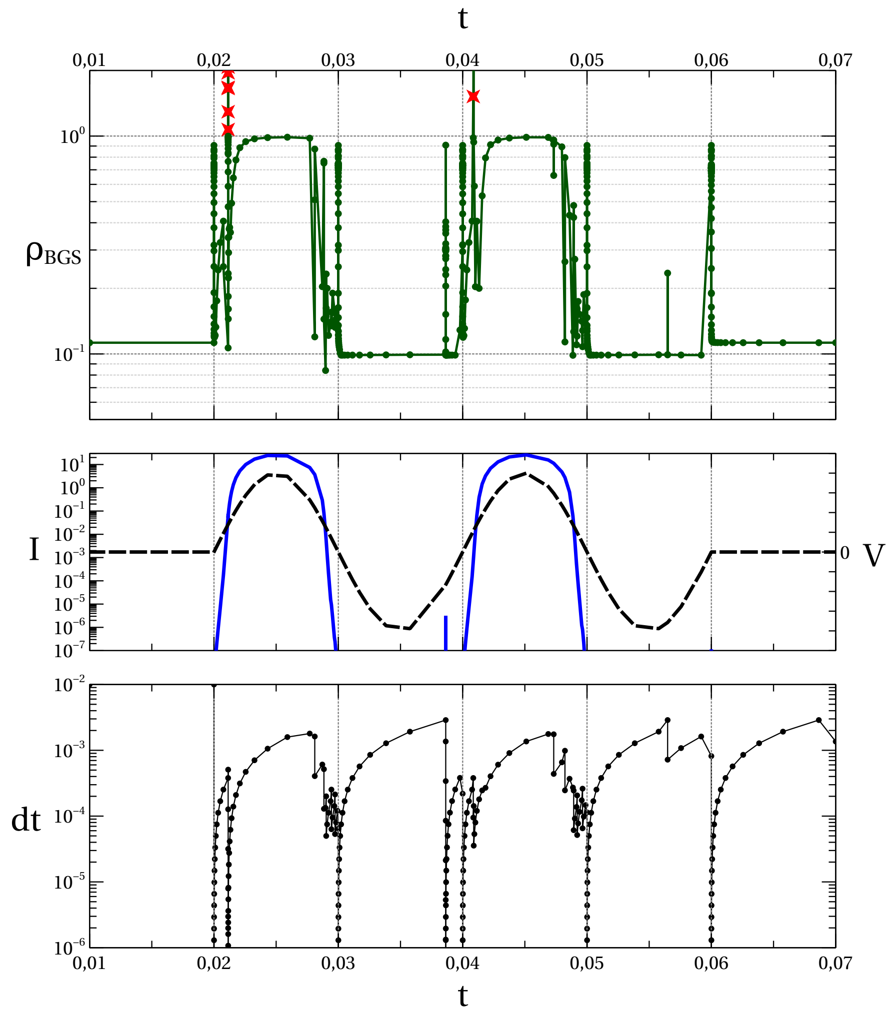

Figure 9.11.: Full simulation for the diode with $\lambda = 4 \times 10^{-5}$. Top: spectral radius for the Block Gauß–Seidel method (green, red stars point out the values over unity); center: voltage (black dashed line) and forward current (blue); bottom: adapted time steps.

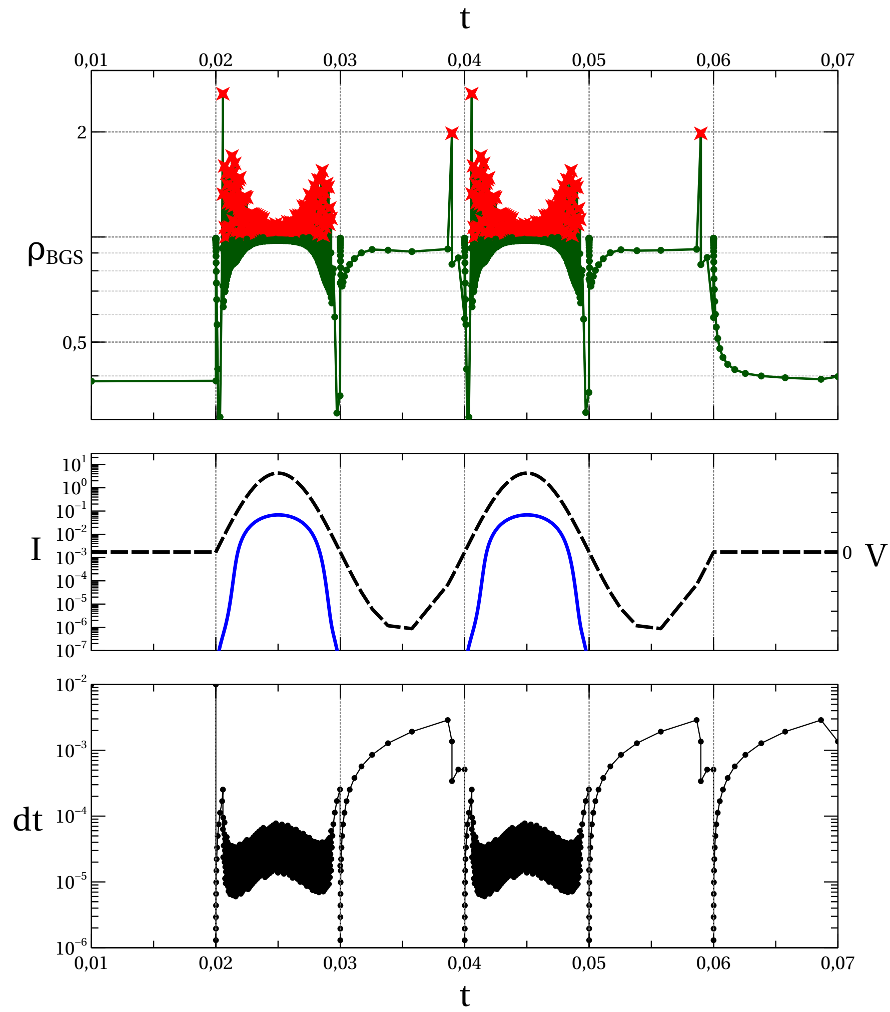

Figure 9.12.: Full simulation for the diode with $\lambda = 5 \times 10^{-6}$. Top: spectral radius for the Block Gauß–Seidel method (green, red stars point out the values over unity); center: voltage (black dashed line) and forward current (blue); bottom: adapted time steps.

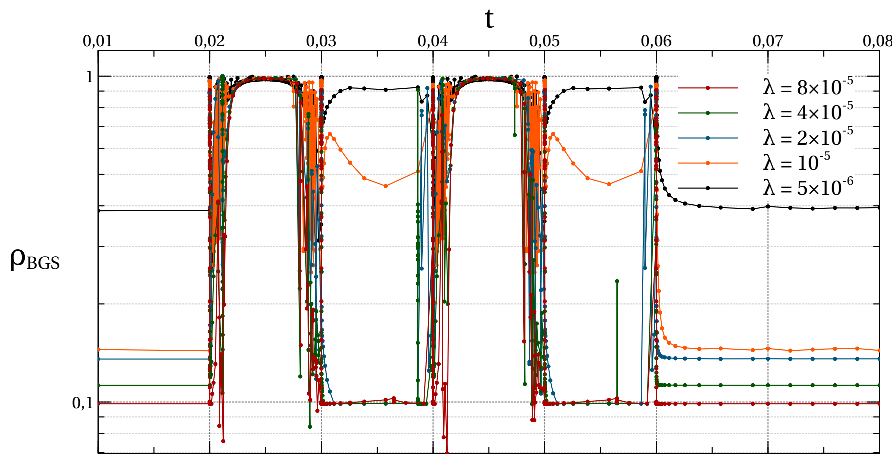

Figure 9.13.: Comparison of the spectral radius of block Gauß–Seidel method over a full simulation

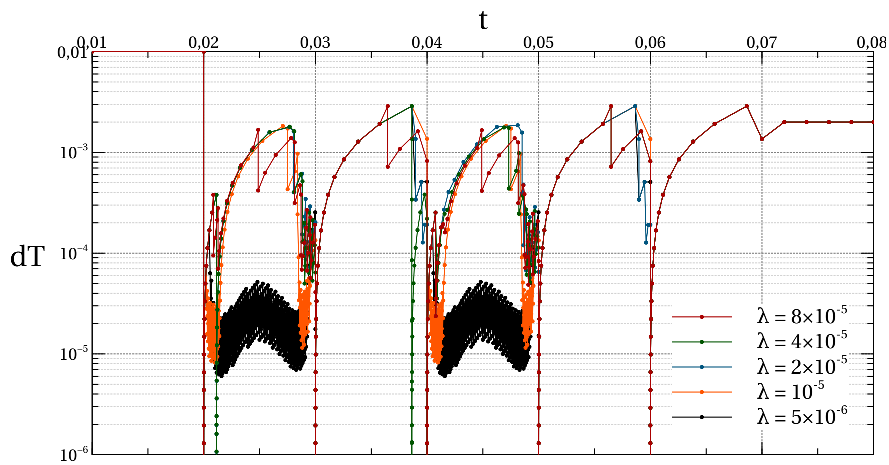

Figure 9.14.: Comparison of the adaptive time steps over a full simulation

9.3. Reverse Recovery Simulation

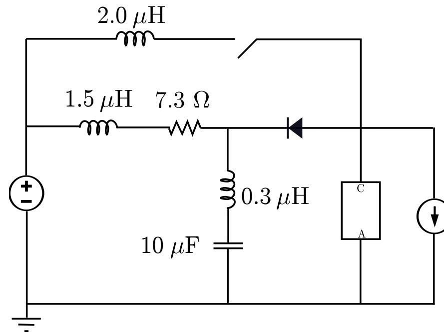

Figure 9.15.: Controlling circuit with protection elements for reverse recovery simulation. From *An algorithm for mixed–mode 3D TCAD for power electronics devices, and application to power p-i-n diode* D. Cagnoni, M. Bellini, J. Vobecký, M. Restelli, and C. de Falco [5]

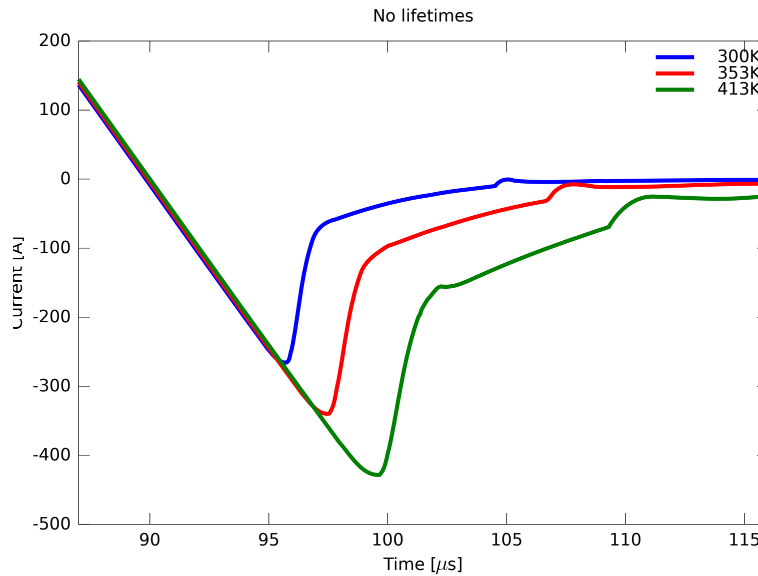

Figure 9.16.: Reverse recovery current for the *p-i-n* diode with standard lifetimes model. From *An algorithm for mixed–mode 3D TCAD for power electronics devices, and application to power p-i-n diode* D. Cagnoni, M. Bellini, J. Vobecký, M. Restelli, and C. de Falco [5]

As a benchmark test case, for both high injection regimes and dependence on temperature as a parameter, we considered the power diode studied in [4]. Such type of diode is irradiated with $1 - 5\,\mathrm{MeV}$ electrons at a dose between 5 and

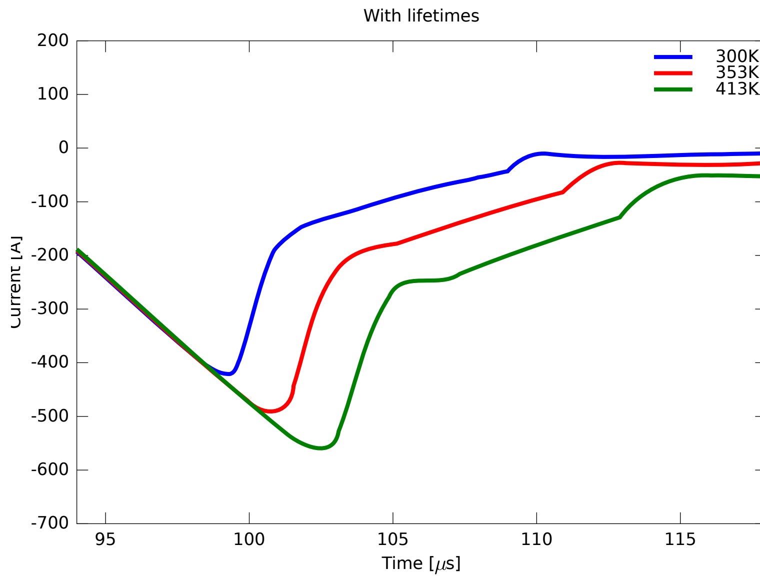

Figure 9.17.: Reverse recovery current for the *p-i-n* diode with optimized lifetimes. From *An algorithm for mixed–mode 3D TCAD for power electronics devices, and application to power p-i-n diode* D. Cagnoni, M. Bellini, J. Vobecký, M. Restelli, and C. de Falco [5]

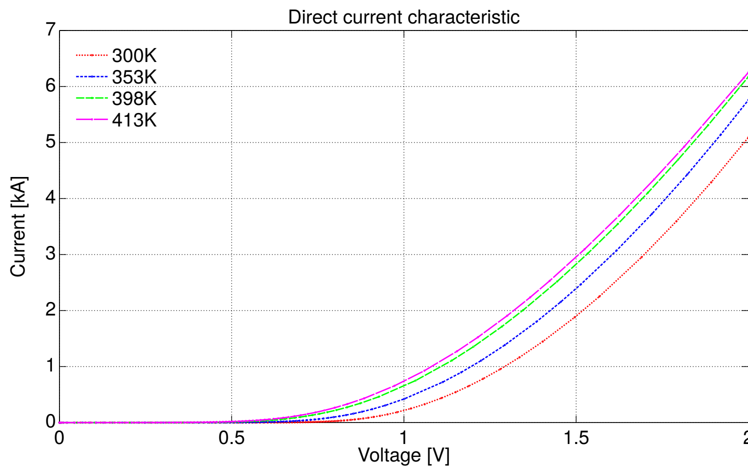

Figure 9.18.: IV characteristic for the *p-i-n* diode with standard lifetimes model. From *An algorithm for mixed–mode 3D TCAD for power electronics devices, and application to power p-i-n diode* D. Cagnoni, M. Bellini, J. Vobecký, M. Restelli, and C. de Falco [5]

20 kGy and $5 - 12$ MeV helium atoms at doses ranging between $10^{14} - 10^{15}\,\mathrm{m}^{-2}$, and annealed at a temperature below 300 °C. In these conditions the dominant deep

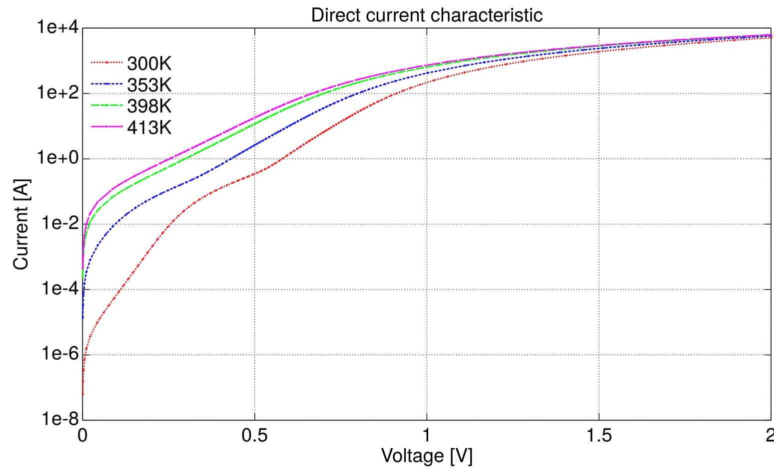

Figure 9.19.: IV characteristic for the *p-i-n* diode with standard lifetimes model, logarithmic scale. From *An algorithm for mixed–mode 3D TCAD for power electronics devices, and application to power p-i-n diode* D. Cagnoni, M. Bellini, J. Vobecký, M. Restelli, and C. de Falco [5]

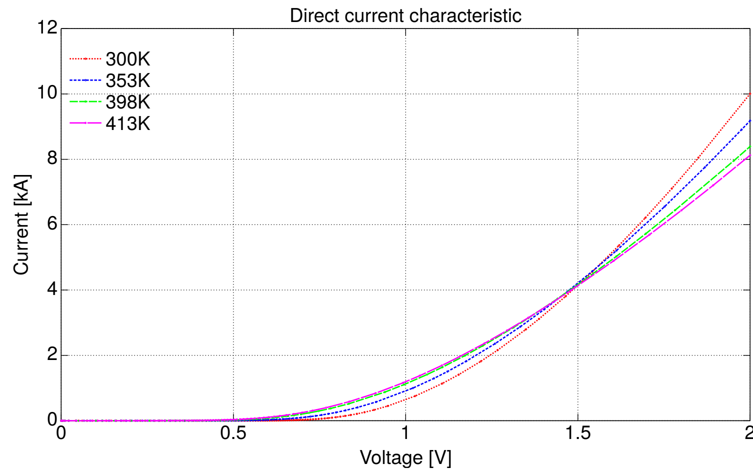

Figure 9.20.: IV characteristic for the *p-i-n* diode with optimized lifetimes. From *An algorithm for mixed–mode 3D TCAD for power electronics devices, and application to power p-i-n diode* D. Cagnoni, M. Bellini, J. Vobecký, M. Restelli, and C. de Falco [5]

levels are the vacancy–oxygen pair (V-O), roughly 0.16 eV below the conduction level, and the divacancy (V-V), roughly 0.42 eV below the conduction level.

As a result, an accurate modeling of the generation–recombination processes via these deep levels is necessary, in order to precisely reproduce the reverse recovery

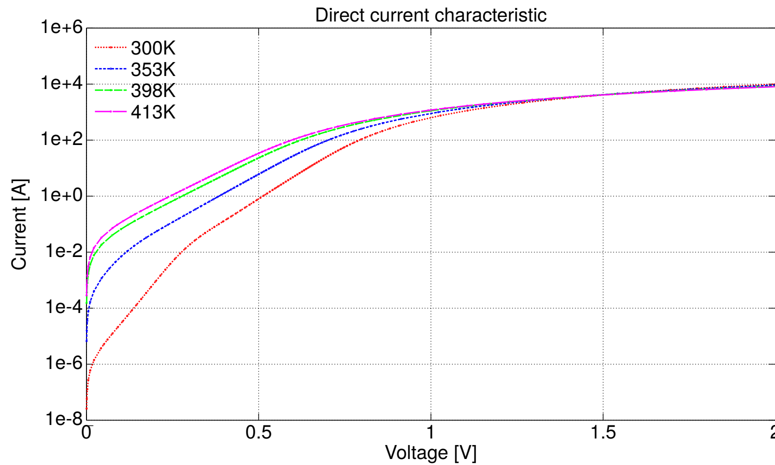

Figure 9.21.: IV characteristic for the *p-i-n* diode with optimized lifetimes, logarithmic scale. From *An algorithm for mixed–mode 3D TCAD for power electronics devices, and application to power p-i-n diode* D. Cagnoni, M. Bellini, J. Vobecký, M. Restelli, and C. de Falco [5]

characteristics of the diode. Complete deep levels models are computationally expensive and degrade convergence; thus, an effective carrier lifetime profile was obtained via optimization with a commercial simulator and introduced within the conventional SRH framework.

The schematic of testing circuit used for reverse recovery measurements is shown in figure 9.15. The inductance is tuned to match the $\frac{\mathrm{d}I}{\mathrm{d}t}$ of the measurements. The simulations are performed over a wide temperature range (300 to 413 K), and the switch is modeled as a time varying resistor, with the conductance ramping smoothly from 10^{-3} S to 10^{3} S in 10 μs (the time derivative of conductance is continuous). Figures 9.16 and 9.17 show the computed discharge profiles. The effect of lifetime controlling results in a prolonged and increased discharge of the power diode, at all temperatures, due to an increased charge buildup. Figures 9.18, 9.19, 9.20 and 9.21 show a detailed view of the computed forward IV characteristic, both with and without the computed lifetimes. The importance of introducing the optimized lifetimes is particularly evidenced in high–injection regime, where the crossing of characteristic curve typical of irradiated devices is correctly reproduced by the optimized carrier lifetimes. Low injection regime characteristics, visible in the log–scale graphs, do not present substantial differences.

10. Thyristor

10.1. Depletion Simulation

This section deals with simulations of a thyristor with analytical doping profiles (shown in figures 10.1 and 10.2) taken from a power devices textbook [3].

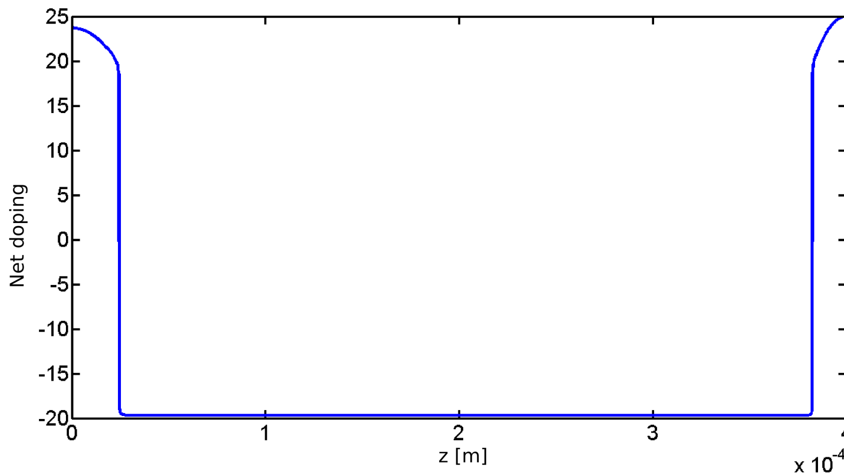

Figure 10.1.: Net doping along z axis, from gate to anode.

The performed simualtions investigate both forward and reverse blocking regimes, with up to 60 V for the former and up to −1400 V for the latter case. In both blocking regimes, the n^- drift region is gradually depleted as bias increases. as shown in figure 10.3 and 10.4.

In reverse bias, the n^+-p and n^--p^+ junctions are reverse–biased while the p-n^- junction is forward–biased. Figure 10.3 shows clearlys the growth of the depleted portion of the drift region starting from the n^--p^+ junction and injection of holes in the drift region from the p region as bias grows.

In forward bias, the p-n^- junction is reverse–biased while the n^+-p and n^--p^+ junctions are forward–biased. In such regime, shown in figure 10.4, the depleted portion grows in the drift region starting from the p-n^- junction, and we can notice injection of holes from the p^+ region in the n^- region.

Figure 10.5 and 10.6 show the trend of the electric field strength depending on the applied voltage. The most part of the applied voltage is sustained by the drift

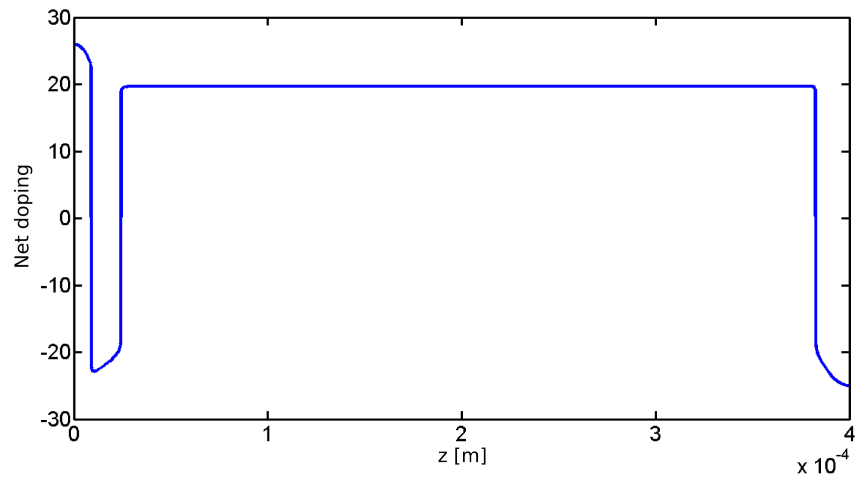

Figure 10.2.: Net doping along z axis, from cathode to anode.

region.

In both cases, the conduction is negligible, since as described in the introduction, unless neither the breakdown nor the punch-through conditions are not met, and without signals from the gate, not enough free carriers are present in the device.

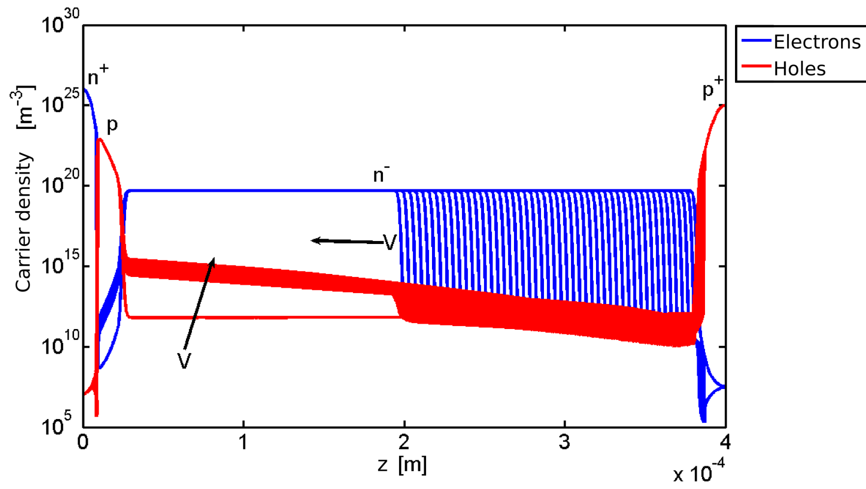

Figure 10.3.: Trend of the carriers concentration in reverse bias

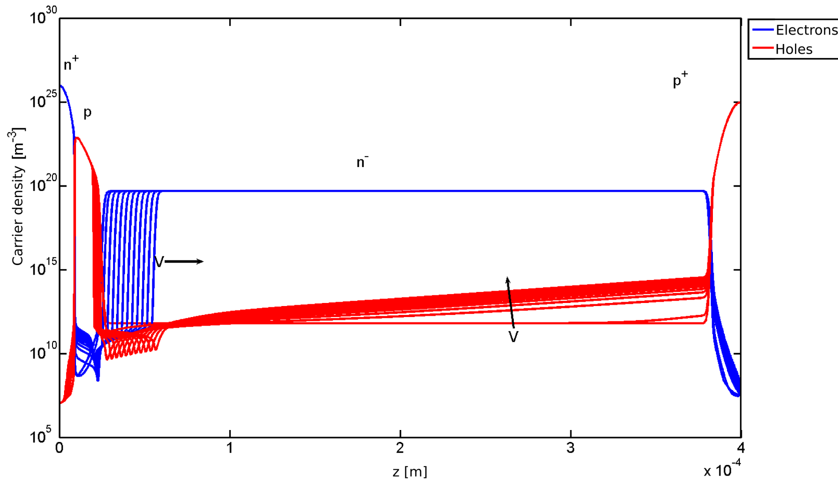

Figure 10.4.: Trend of the carrier concentration in forward bias

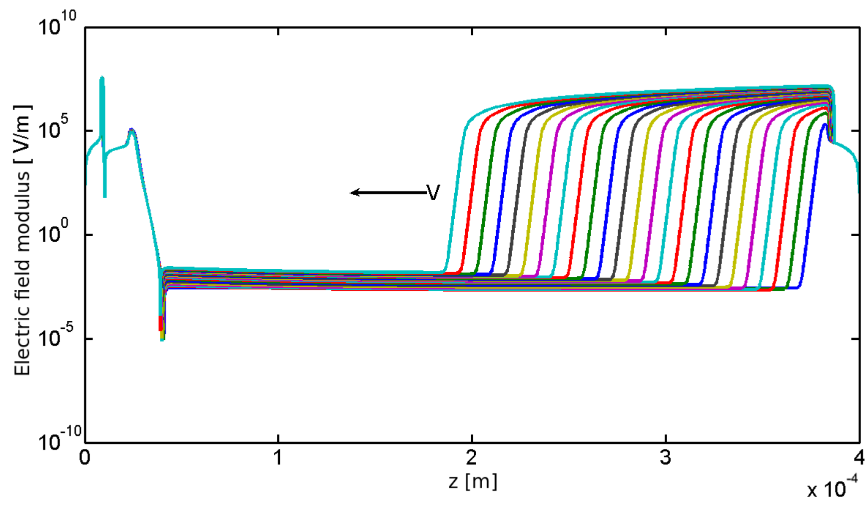

Figure 10.5.: Electric field trend in reverse bias

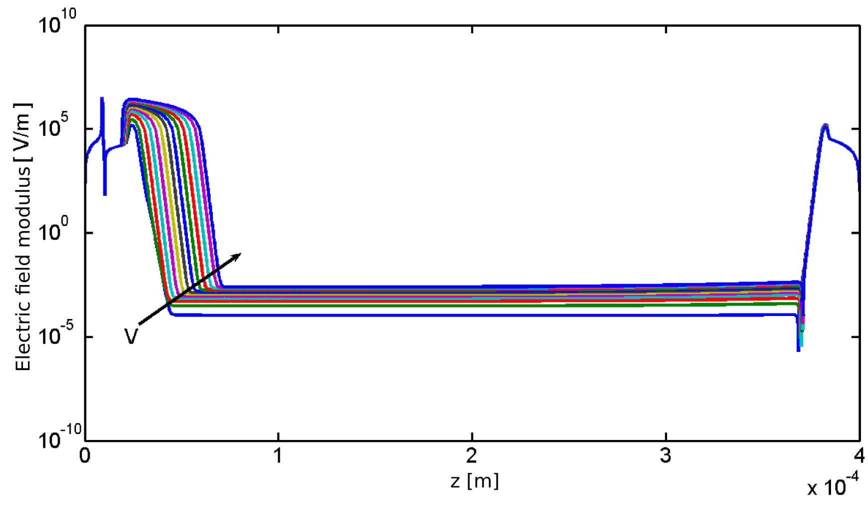

Figure 10.6.: Electric field trend in forward bias

10.2. Phase Controlled Thyristor

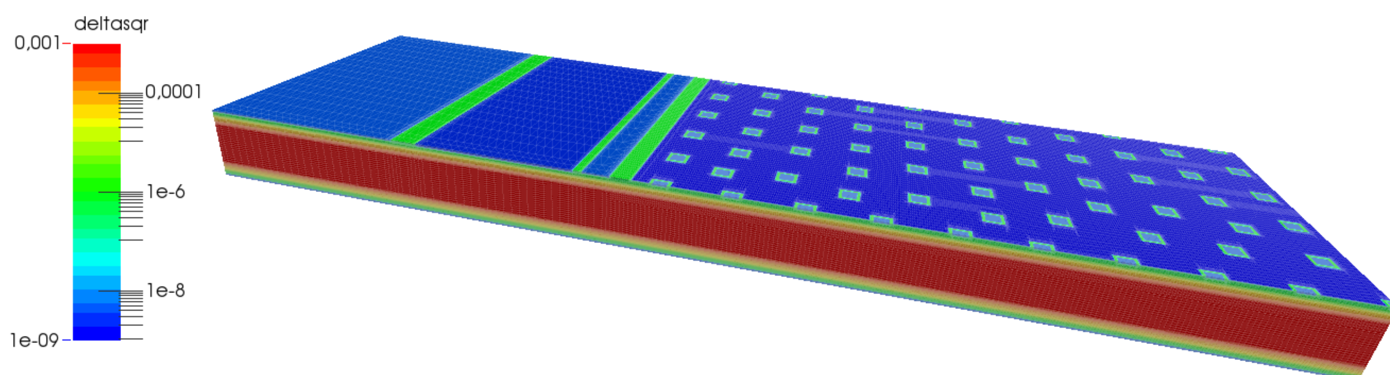

Figure 10.7.: Value of nondimensional parameter δ^2 on PCT surface. Cathode, gate, amplifying gate are visible.

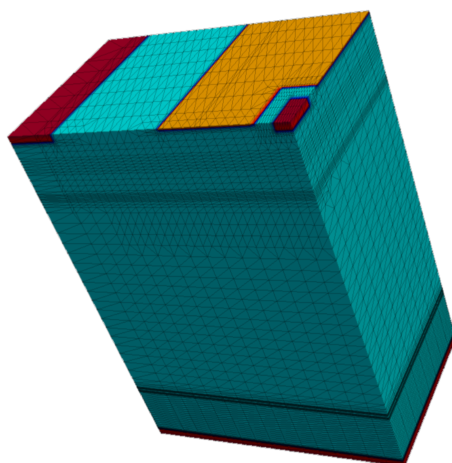

Figure 10.8.: Effective intrinsic density, comprising bandgap narrowing, and mesh.

Figure 10.7 depicts the domain used for the simulation of a realistic industrial device: a slice of a phase-controlled thyristor (PCT), its cathode covered by *shorts* with the function of increasing the device blocking rating.

The mesh used to represent the PCT is built upon roughly 1.1×10^6 nodes. In this section we employ it, together with meshes built over portions of the original domain, in order to evaluate the performance of our proposed linear solver. Figures 10.8 through 10.12 depict such subdomains, meshed with a number of nodes

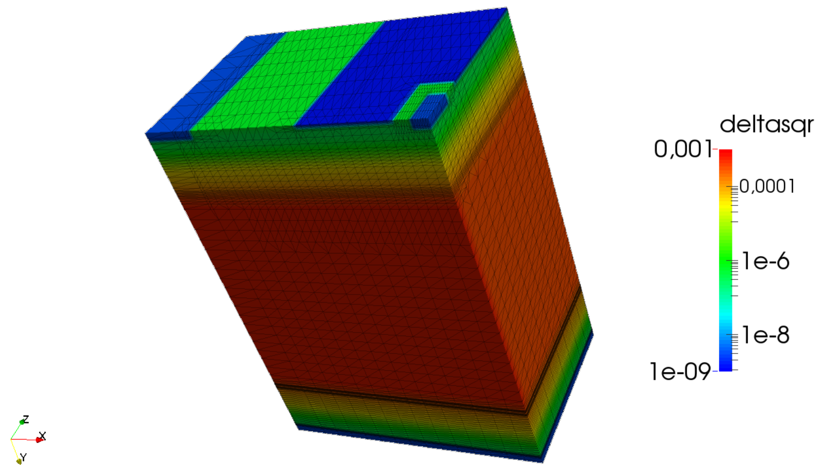

Figure 10.9.: Local nondimensional parameter δ^2on a portion of PCT.

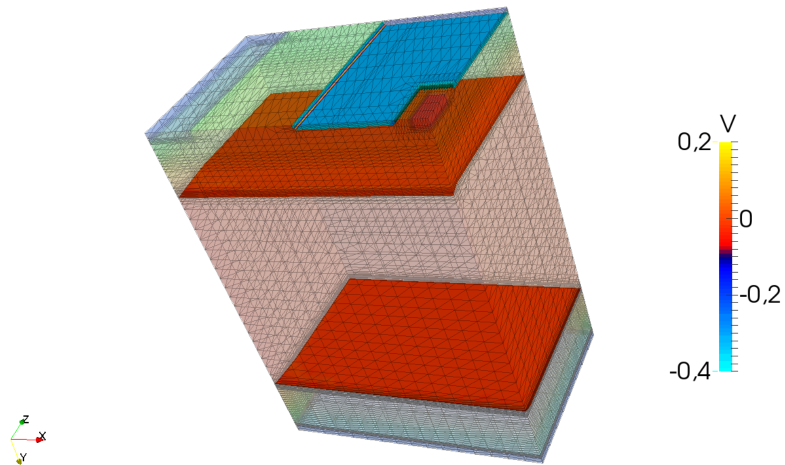

Figure 10.10.: Junction surfaces ($N_{\mathrm{bi}} = 0$) colored by electric potential at equilibrium [V].

between 10^4 and 10^5. All subdomains contain a portion of gate and a portion of cathode with a short, with the relative mesh refining.

Figure 10.13 reports the profiling of our solver on a 16 cores parallel run. The points in the graphics corresponding to a monolithic solution for the realistic mesh is missing, as the employed machine, with 270 Gb RAM, is not able to store the full Jacobian factors.

The implementation at the time of the writing is not fully optimized, as the *solve*

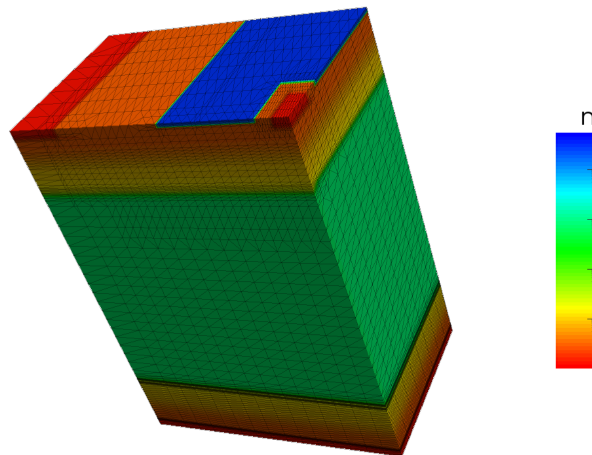

Figure 10.11.: Electron density at equilibrium, colored by logarithmic scale, and mesh.

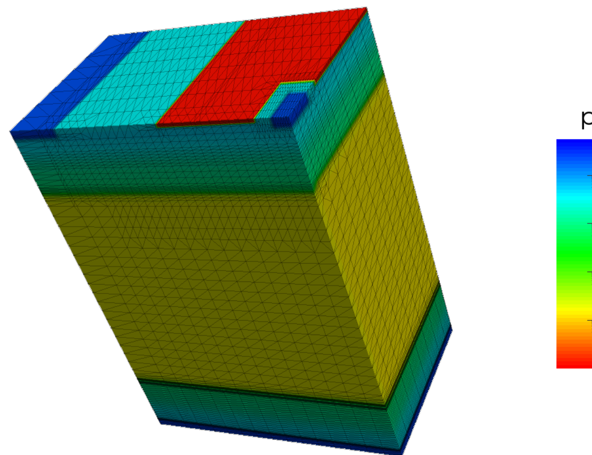

Figure 10.12.: Hole density at equilibrium, colored by logarithmic scale, and mesh.

stage of the BGS solver is still serial. As expected, the *solve* stage takes longer for the BGS solver than for the monolithic one, and in few iterations, the time employed on the *solve* stage may become comparable with the time employed in the *factorize* stage.

Besides the parallelization of some parts of the BGS algorithms, like the matrix-vector multiplications, which would reduce the single iteration time, a big benefit may be obtained through vector extrapolation techniques. As shown in figure 10.13, the additional time needed to perform RRE is almost negligible if com-

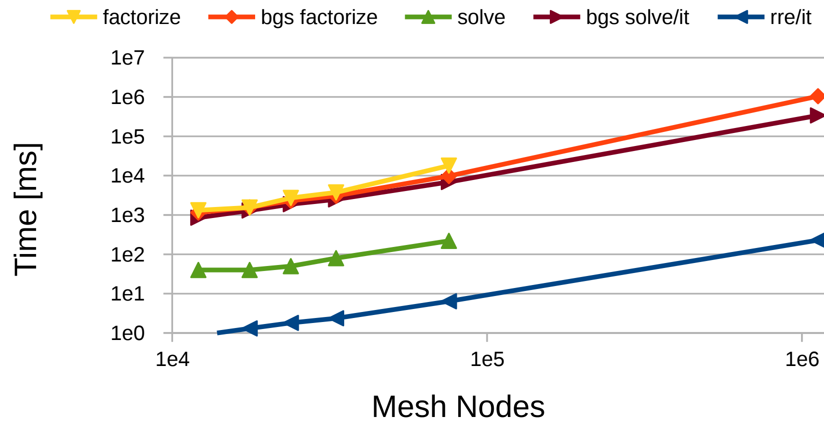

Figure 10.13.: Solver profiling: times for *factorize*, *solve*, and *extrapolation* phases for both the monolithic solver and the BGS method, versus number of mesh nodes.

pared to the total time for the *solve* stage in the BGS algorithm.

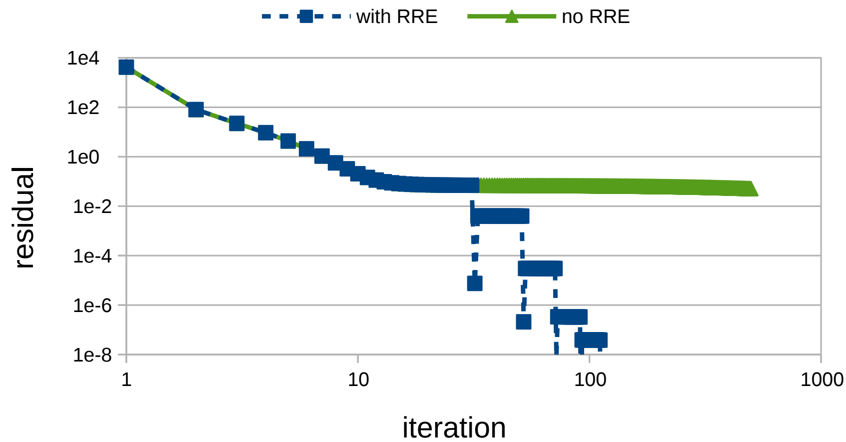

Figure 10.14.: Linear system solution with plain BGS algorithm (green), and with BGS algorithm accelerated through *Reduced Rank Extrapolation* (blue). History of convergence of the relative residual.

Figure 10.14 shows the history of convergence of two different instances of the BGS solver, in a plain version and in an accelerated version (RRE with rank of 20). It is easy to see how the extrapolation helps reducing the number of iterations, with only marginal computational cost.

11. Conclusions

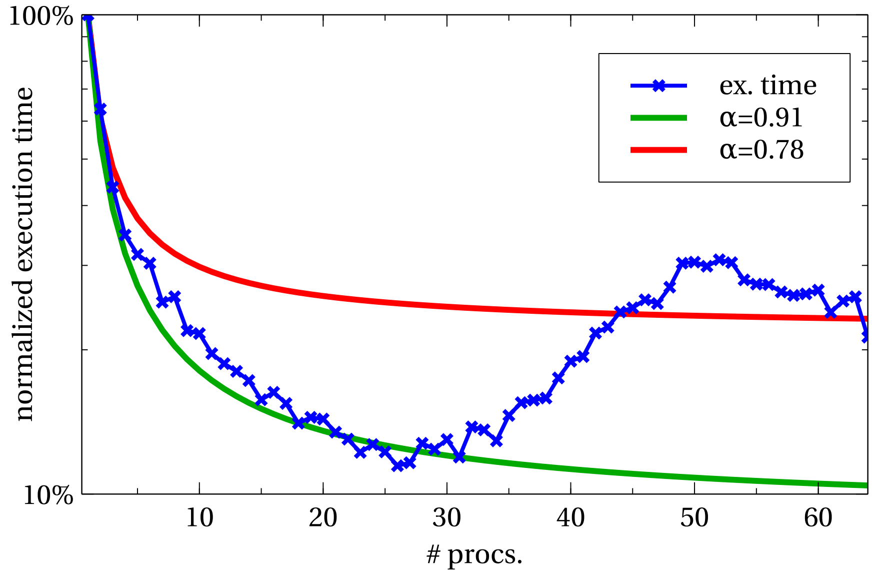

Figure 11.1.: Normalized runtime on multi–core machines, compared with theoretical trends given by Amdahl's law, for a portion of parallel computation equal to α. The drop–off for over 32 processors is due to the communications overhead of the testing architecture, a cluster of 32-core machines.

The present thesis was carried out in the framework of a collaboration between the Modeling and Scientific Computing (MOX) lab of Politecnico di Milano, and the Power Electronics department in the Corporate Research Center of ABB in Baden–Dättwil, Switzerland aimed at implementing a parallel 3D TCAD simulator especially tailored for the needs of the Power Semiconductors industry in general and for those of ABB in particular.

The resulting C++ code, named CGDD++, was developed from scratch during the preparation of the present thesis, building on the experience gained during a preliminary feasibility study, and the Fortran 2003 code (CGDD) that was implemented during that preliminary phase and was based on the FEMilaro [7] library.

CGDD++ relies on the BIM++ [6] library for spatial discretization of differential operators and uses MUMPS [9] or LIS [8] for the solution of linear systems of algebraic equations.

The development of CGDD was partially supported by the SuperComputing

Applications and Innovations (SCAI) department of CINECA, Italy through the Interdisciplinary Laboratory for Advanced Simulation (LISA) projects 3DSPEED (3D Simulation of PowEr Electronics Devices, 2014) and PDDD (3D Power electronics Drift Diffusion Device simulation, 2013).

The main feature of CGDD++, which were the objective of this thesis, is the ability to allow implementation and testing of a wide range numerical algorithms suited for very large scale parallel mixed–mode simulation of Power Semiconductor devices, including electro–thermal effects.

Particular emphasis was devoted during the development of this thesis to the implementation and assessment of various linear and nonlinear iteration strategies, in particular a block-iterative solution strategy for solving the very large linear system stemming from the application of the monolithic Newton method to the solution of mixed mode MNA/DD equations was developed and studied. Through extensive numerical testing the developed procedure was shown to enjoy interesting convergence properties at a cost which is significantly lower with respect to parallel direct solvers.

References

[1] W. Fulop. “Calculation of avalanche breakdown voltages of silicon p-n junctions”. In: *Solid-State Electronics* 10.1 (1967), pp. 39–43. ISSN: 0038-1101. DOI: 10.1016/0038-1101(67)90111-6.

[2] Mark E. Law, E. Solley, et al. “Self-Consistent Model of Minority-Carrier Lifetime, Diffusion Length, and Mobility”. In: *IEEE ELectron Device Letter* 12 (1991), pp. 401–403.

[3] B Jayant Baliga. *Fundamentals of power semiconductor devices*. Springer Science & Business Media, 2010.

[4] Marco Bellini and Jan Vobecky. “TCAD simulations of irradiated power diodes over a wide temperature range”. In: *Simulation of Semiconductor Processes and Devices (SISPAD), 2011 International Conference on*. IEEE. 2011, pp. 183–186.

[5] Davide Cagnoni, Marco Bellini, et al. “An algorithm for mixed-mode 3D TCAD for power electronics devices, and application to power p-i-n diode”. In: *Progress in Industrial Mathematics at ECMI 2014*. Mathematics in Industry. Springer, 2016.

[6] *BIM++*. URL: http://gitserver.mate.polimi.it/redmine/projects/bim (visited on 02/01/2016).

[7] *FEMilaro*. URL: http://code.google.com/p/femilaro/ (visited on 02/01/2016).

[8] *Lis: Library of Iterative Solvers for Linear Systems*. URL: http://www.ssisc.org/lis/ (visited on 02/01/2016).

[9] *MUMPS: a MUltifrontal Massively Parallel sparse direct Solver*. URL: http://mumps.enseeiht.fr/ (visited on 02/01/2016).

Appendix

A. Circuital examples

Example: KCL for a CMOS inverter

To contextualize the abstract setting proposed in 3.1.1 a simple example based on a CMOS inverter circuit is borrowed from [3].

The electrical schematic associated with this circuit is composed of 3 nodes (except ground) and 4 elements, as shown in fig. A.1. Ground node has been numbered as 0. In this case the system of balance equations reads:

$$\begin{array}{lrcl} \text{(node 1)} & i_{V1} + i_{G2} + i_{G1} & = & 0, \\ \text{(node 2)} & i_{U1} + i_{S1} & = & 0, \\ \text{(node 3)} & i_{D1} + i_{D2} & = & 0. \end{array} \tag{A.1}$$

Notice that the balance of ground node, namely:

$$\text{(node 0)} \quad i_{V2} + i_{S2} + i_{U2} = 0, \tag{A.2}$$

can be recovered summing all the equations in A.1 and taking into account that the algebraic sum of the components of each element current vector must be zero due to 3.1:

$$\begin{array}{rcl} i_{U1} + i_{U2} & = & 0, \\ i_{V1} + i_{V2} & = & 0, \\ i_{S1} + i_{G1} + i_{D1} & = & 0, \\ i_{S2} + i_{G2} + i_{D2} & = & 0. \end{array}$$

Defining the current vectors:

$$\mathbf{i}_U = \begin{bmatrix} i_{U1} \\ i_{U2} \end{bmatrix}, \ \mathbf{i}_V = \begin{bmatrix} i_{V1} \\ i_{V2} \end{bmatrix}, \ \mathbf{i}_{M1} = \begin{bmatrix} i_{G1} \\ i_{S1} \\ i_{D1} \end{bmatrix}, \ \mathbf{i}_{M2} = \begin{bmatrix} i_{G2} \\ i_{S2} \\ i_{D2} \end{bmatrix}, \tag{A.3}$$

and the local incidence matrices:

$$A_U = \begin{bmatrix} 0 & 0 \\ 1 & 0 \\ 0 & 0 \end{bmatrix}, \ A_V = \begin{bmatrix} 1 & 0 \\ 0 & 0 \\ 0 & 0 \end{bmatrix}, \ A_{M1} = \begin{bmatrix} 1 & 0 & 0 \\ 0 & 1 & 0 \\ 0 & 0 & 1 \end{bmatrix}, \ A_{M2} = \begin{bmatrix} 1 & 0 & 0 \\ 0 & 0 & 0 \\ 0 & 0 & 1 \end{bmatrix}, \tag{A.4}$$

it is possible to rewrite A.1 in a form that suits 3.3:

$$A_U \mathbf{i}_U + A_V \mathbf{i}_V + A_{M1} \mathbf{i}_{M1} + A_{M2} \mathbf{i}_{M2} = 0. \tag{A.5}$$

To derive a full system of equations from A.5 it is at this point necessary to define an appropriate set of unknowns and constitutive relations for the electrical elements appearing in A.1, as explained in section 3.1.2.

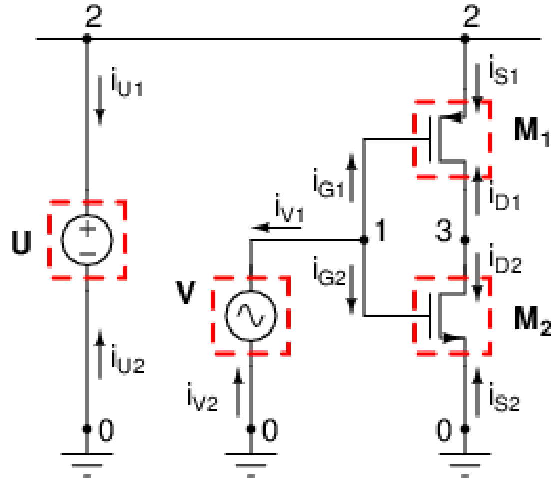

Figure A.1.: CMOS inverter circuit electrical schematic, composed of 4 elements (dashed red frame) and 3 nodes plus ground.

Example: Shichman-Hodges MOS-FET model

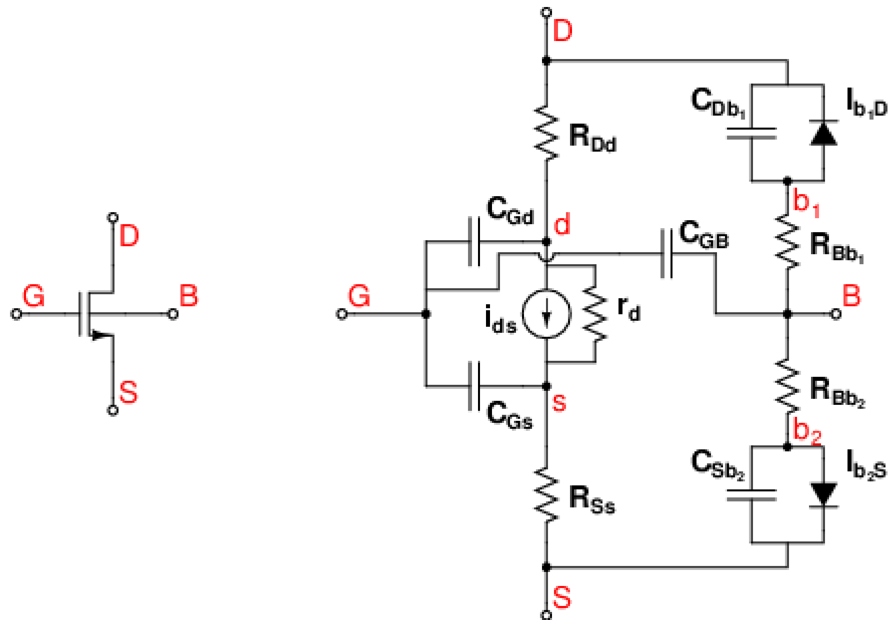

Figure A.2.: On the left the symbol usually used in schematics to represent a 4–pins nMOS-FET, on the right the corresponding Shichman-Hodges model composed of 5 linear capacitors, 5 linear resistors, 2 nonlinear resistors (diodes) and a voltage controlled current source. Notice the presence of 4 inner nodes.

Consider the n-channel MOS-FET shown in A.2 on the left. Its four pins are respectively associated with *gate* (G), *drain* (D), *source* (S) and *bulk* (B) terminals. The corresponding Shichman-Hodges model [5] is given by the equivalent circuit shown in A.2 on the right.

Though being one of the most simple MOS-FET model usually provided with SPICE-like circuit simulators (see [2, 1] for more sophisticated ones), it already introduces 4 inner nodes that do not appear in the original schematic. The current balance at these nodes is regarded in the usual DAE formulation of MNA 3.10 as being part of KCL, while in the proposed *element–wise* formulation it will be considered as part of the MOS-FET constitutive relations. It is precisely this latter feature that gives the *element–wise* notation the possibility to describe circuits on a hierarchical base.

Example: CMOS inverter, charge oriented MNA with element–wise formulation

In the following it is shown how to derive the full system of equations stemming from the charge–oriented MNA description of the CMOS inverter depicted in A.1. Consider then the circuit schematic and assume that the Shichman-Hodges model [5] is used for both the MOS-FETs. For the sake of simplicity the bulk terminals of the transistors are assumed to be connected to the ground node, so that the *element–wise* formulation starts from the system of balance equations (A.1). The vector of nodal potentials reads:

$$\mathbf{n} = \begin{bmatrix} e_1 & e_2 & e_3 \end{bmatrix}^T . \tag{A.6}$$

The set–up for a generic voltage source is depicted in A.3. It can be readily seen

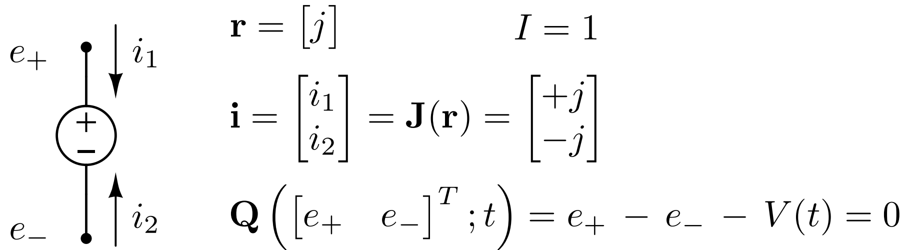

Figure A.3.: Voltage source set–up in the element–wise notation. Notice that in this case one internal variable is needed to properly describe the element, and thus one additional constitutive relation is given to close the set of MNA equations.

that one internal variable is employed (namely the branch current j), and thus the additional constitutive relation:

$$\mathbf{Q}([e_+, e_-]^T; t) \;=\; e_+ \;-\; e_- \;-\; V(t) = 0 \;, \tag{A.7}$$

is needed to close the system. In (A.7) e_+ and e_- indicate the generic node potentials of the considered two–pins element while $V(t)$ is the known voltage waveform of the source. A similar set–up is presented in (A.4) for the n-channel MOS-FET.

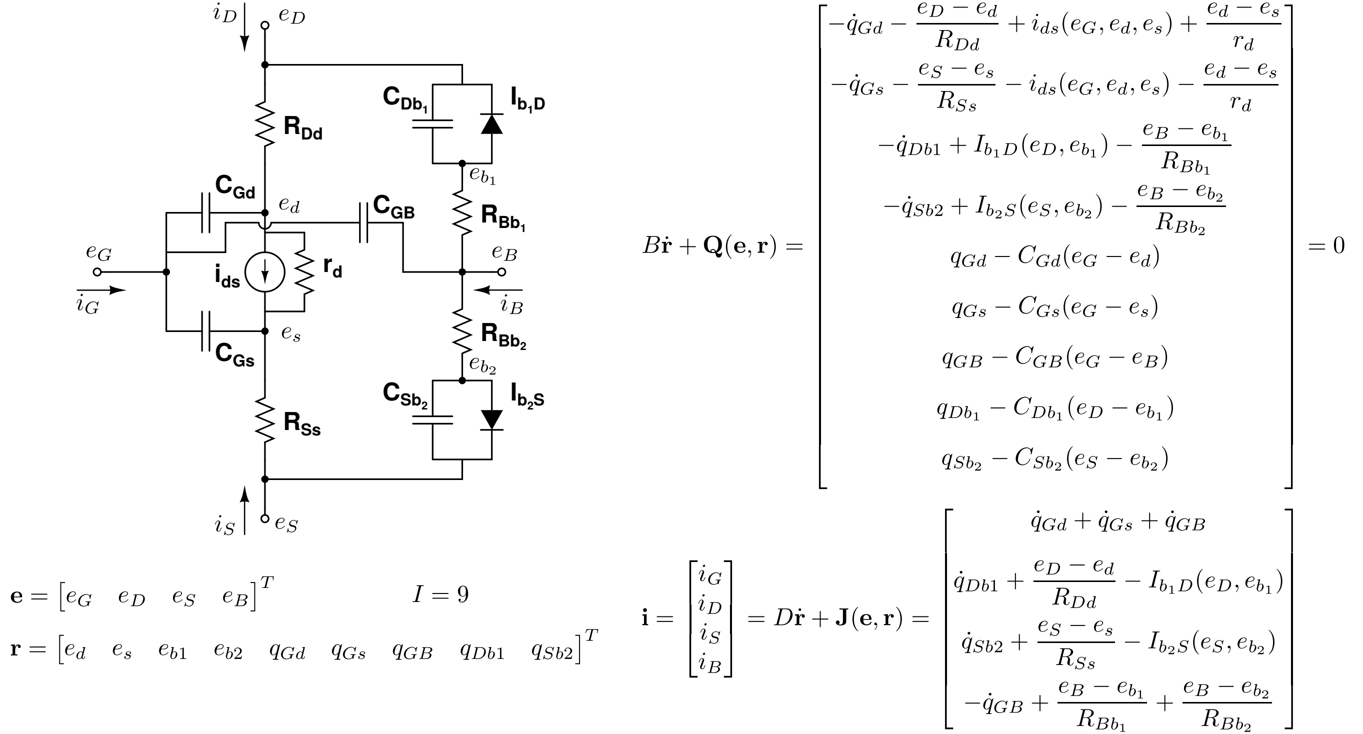

Figure A.4.: Set–up of the extended n-channel MOS-FET using the Shichman Hodges model in the element–wise notation. In this case 9 internal variables are present, and thus 9 additional constitutive relations are given to close the set of MNA equations. $I_{b_1D}(e_D, e_{b_1})$, $I_{b_2S}(e_S, e_{b_2})$ and $i_{ds}(e_G, e_d, e_s)$ are given functions modeling respectively the leakage currents through the diodes, and the current of the voltage controlled current source appearing in the equivalent circuit.

In this case 9 internal variables are required to completely describe the element: these are constituted by the four internal nodes potentials e_d, e_s, e_{b_1}, e_{b_2} and by the 5 charges associated with each capacitor (q_{Gd},q_{Gs},q_{GB},q_{Db_1},q_{Sb_2}). The current balances at the internal nodes are part of the nMOS-FET constitutive relations, as they stem from the choice to model the transistor with the Shichman Hodges equivalent circuit. Notice that no other k–pins element is allowed to be connected to these nodes, as they constitute only an internal representation of the MOS-FET. This latter feature is often employed in practice to enhance simulation performance exploiting a Schur-complement based technique on these inner equations, as shown in [4]. Of course a similar representation can be derived for the

p-channel MOS-FET.

At this point each flux vector appearing in (A.1) is expressed in a form that suits 3.11, while the additional constitutive relations of the corresponding element are provided in a form resembling 3.13. It is thus possible to follow the procedure depicted in chapter 3 and derive a closed system of:

- 3 balance equations at the electrical nodes 1-3:

$$
\begin{aligned}
j^{[\mathbf{V}]} + \dot{q}_{Gd}^{[\mathbf{M}_1]} + \dot{q}_{Gs}^{[\mathbf{M}_1]} + \dot{q}_{GB}^{[\mathbf{M}_1]} + \dot{q}_{Gd}^{[\mathbf{M}_2]} + \dot{q}_{Gs}^{[\mathbf{M}_2]} + \dot{q}_{GB}^{[\mathbf{M}_2]} &= 0 \;, \\
j^{[\mathbf{U}]} + \dot{q}_{Sb2}^{[\mathbf{M}_1]} + \frac{e_2 - e_s^{[\mathbf{M}_1]}}{R_{Ss}^{[\mathbf{M}_1]}} + I_{b_2 S}^{[\mathbf{M}_1]}(e_2, \theta_4, e_{b_2}^{[\mathbf{M}_1]}) &= 0 \;, \\
\dot{q}_{Db1}^{[\mathbf{M}_1]} + \frac{e_3 - e_d^{[\mathbf{M}_1]}}{R_{Dd}^{[\mathbf{M}_1]}} + I_{b_1 D}^{[\mathbf{M}_1]}(e_3, \theta_4, e_{b_1}^{[\mathbf{M}_1]}) + & \\
\dot{q}_{Db1}^{[\mathbf{M}_2]} + \frac{e_3 - e_d^{[\mathbf{M}_2]}}{R_{Dd}^{[\mathbf{M}_2]}} - I_{b_1 D}^{[\mathbf{M}_2]}(e_3, \theta_5, e_{b_1}^{[\mathbf{M}_2]}) &= 0 \;,
\end{aligned}
$$

- 1 constitutive relation for the input voltage source V:

$$e_1 - v(t) = 0 \;,$$

  where $v(t)$ is a given voltage waveform,

- 1 constitutive relation for the feed voltage source U:

$$e_2 - V_{DD} = 0 \;,$$

  where V_{DD} is the given feed voltage,

- 9 constitutive relations for the p-channel MOS-FET M_1:

$$
\begin{aligned}
-\dot{q}_{Gd}^{[\mathbf{M}_1]} - \frac{e_3 - e_d^{[\mathbf{M}_1]}}{R_{Dd}^{[\mathbf{M}_1]}} + i_{ds}^{[\mathbf{M}_1]}(e_1, \theta_4, e_d^{[\mathbf{M}_1]}, e_s^{[\mathbf{M}_1]}) + \frac{e_d^{[\mathbf{M}_1]} - e_s^{[\mathbf{M}_1]}}{r_d^{[\mathbf{M}_1]}} &= 0 \ , \\
-\dot{q}_{Gs}^{[\mathbf{M}_1]} - \frac{e_2 - e_s^{[\mathbf{M}_1]}}{R_{Ss}^{[\mathbf{M}_1]}} - i_{ds}^{[\mathbf{M}_1]}(e_1, \theta_4, e_d^{[\mathbf{M}_1]}, e_s^{[\mathbf{M}_1]}) - \frac{e_d^{[\mathbf{M}_1]} - e_s^{[\mathbf{M}_1]}}{r_d^{[\mathbf{M}_1]}} &= 0 \ , \\
-\dot{q}_{Db1}^{[\mathbf{M}_1]} - I_{b_1 D}^{[\mathbf{M}_1]}(e_3, \theta_4, e_{b_1}^{[\mathbf{M}_1]}) + \frac{e_{b_1}^{[\mathbf{M}_1]}}{R_{Bb_1}^{[\mathbf{M}_1]}} &= 0 \ , \\
-\dot{q}_{Sb2}^{[\mathbf{M}_1]} - I_{b_2 S}^{[\mathbf{M}_1]}(e_2, \theta_4, e_{b_2}^{[\mathbf{M}_1]}) + \frac{e_{b_2}^{[\mathbf{M}_1]}}{R_{Bb_2}^{[\mathbf{M}_1]}} &= 0 \ , \\
q_{Gd}^{[\mathbf{M}_1]} - C_{Gd}^{[\mathbf{M}_1]}(e_1 - e_d^{[\mathbf{M}_1]}) &= 0 \ , \\
q_{Gs}^{[\mathbf{M}_1]} - C_{Gs}^{[\mathbf{M}_1]}(e_1 - e_s^{[\mathbf{M}_1]}) &= 0 \ , \\
q_{GB}^{[\mathbf{M}_1]} - C_{GB}^{[\mathbf{M}_1]}(e_1) &= 0 \ , \\
q_{Db_1}^{[\mathbf{M}_1]} - C_{Db_1}^{[\mathbf{M}_1]}(e_3 - e_{b_1}^{[\mathbf{M}_1]}) &= 0 \ , \\
q_{Sb_2}^{[\mathbf{M}_1]} - C_{Sb_2}^{[\mathbf{M}_1]}(e_2 - e_{b_2}^{[\mathbf{M}_1]}) &= 0 \ ,
\end{aligned}
$$

- 9 constitutive relations for the n-channel MOS-FET M_2:

$$
\begin{aligned}
-\dot{q}_{Gd}^{[\mathbf{M}_2]} - \frac{e_3 - e_d^{[\mathbf{M}_2]}}{R_{Dd}^{[\mathbf{M}_2]}} + i_{ds}^{[\mathbf{M}_2]}(e_1, \theta_5, e_d^{[\mathbf{M}_2]}, e_s^{[\mathbf{M}_2]}) + \frac{e_d^{[\mathbf{M}_2]} - e_s^{[\mathbf{M}_2]}}{r_d^{[\mathbf{M}_2]}} &= 0 \, , \\
-\dot{q}_{Gs}^{[\mathbf{M}_2]} + \frac{e_s^{[\mathbf{M}_2]}}{R_{Ss}^{[\mathbf{M}_2]}} - i_{ds}^{[\mathbf{M}_2]}(e_1, \theta_5, e_d^{[\mathbf{M}_2]}, e_s^{[\mathbf{M}_2]}) - \frac{e_d^{[\mathbf{M}_2]} - e_s^{[\mathbf{M}_2]}}{r_d^{[\mathbf{M}_2]}} &= 0 \, , \\
-\dot{q}_{Db1}^{[\mathbf{M}_2]} + I_{b_1 D}^{[\mathbf{M}_2]}(e_3, \theta_5, e_{b_1}^{[\mathbf{M}_2]}) + \frac{e_{b_1}^{[\mathbf{M}_2]}}{R_{Bb_1}^{[\mathbf{M}_2]}} &= 0 \, , \\
-\dot{q}_{Sb2}^{[\mathbf{M}_2]} + I_{b_2 S}^{[\mathbf{M}_2]}(0, \theta_5, e_{b_2}^{[\mathbf{M}_2]}) + \frac{e_{b_2}^{[\mathbf{M}_2]}}{R_{Bb_2}^{[\mathbf{M}_2]}} &= 0 \, , \\
q_{Gd}^{[\mathbf{M}_2]} - C_{Gd}^{[\mathbf{M}_2]}(e_1 - e_d^{[\mathbf{M}_2]}) &= 0 \, , \\
q_{Gs}^{[\mathbf{M}_2]} - C_{Gs}^{[\mathbf{M}_2]}(e_1 - e_s^{[\mathbf{M}_2]}) &= 0 \, , \\
q_{GB}^{[\mathbf{M}_2]} - C_{GB}^{[\mathbf{M}_2]}(e_1) &= 0 \, , \\
q_{Db_1}^{[\mathbf{M}_2]} - C_{Db_1}^{[\mathbf{M}_2]}(e_3 - e_{b_1}^{[\mathbf{M}_2]}) &= 0 \, , \\
q_{Sb_2}^{[\mathbf{M}_2]} + C_{Sb_2}^{[\mathbf{M}_2]}(e_{b_2}^{[\mathbf{M}_2]}) &= 0 \, ,
\end{aligned}
$$

All these equations describe the behavior of the CMOS inverter circuit. The corresponding system variables are the 3 nodal potentials $\mathbf{e}$, the branch currents $j^{[\mathbf{U}]}$,$j^{[\mathbf{V}]}$ and $j^{[\mathbf{E}]}$ associated with the voltage sources, the 8 inner node potentials plus the 10 capacitor charges contributed by the two MOS-FETs.

Bibliography

[1] Andrei Vladimirescu and Sally Liu. *The Simulation of MOS Integrated Circuits Using SPICE2*. Tech. rep. EECS Department, University of California, Berkeley, 1980. URL: http://www.eecs.berkeley.edu/Pubs/TechRpts/1980/9610.html.

[2] D. P. Foty. *MOSFET modeling with SPICE: principles and practice*. Upper Saddle River, NJ, USA: Prentice-Hall, Inc., 1997. ISBN: 0-13-227935-5.

[3] Massimiliano Culpo. “Numerical Algorithms for System Level Electro-Thermal Simulation”. PhD thesis. Bergische Universität Wuppertal, 2009.

[4] Uwe Feldmann, Masataka Miyake, et al. “On Local Handling of Inner Equations in Compact Models”. In: *Scientific Computing in Electrical Engineering SCEE 2008*. Ed. by Janne Roos and Luis R.J. Costa. Vol. 14. Mathematics in Industry. Springer Berlin Heidelberg, 2010, pp. 143–150. ISBN: 978-3-642-12293-4. DOI: 10.1007/978-3-642-12294-1_19.

[5] H. Shichman and D.A. Hodges. “Modeling and simulation of insulated-gate field-effect transistor switching circuits”. In: *Solid-State Circuits, IEEE Journal of* 3.3 (Sep 1968), pp. 285–289. ISSN: 0018-9200.

Grazie

A Carlo de Falco e Marco Bellini, che mi hanno permesso di vivere l'istruttiva esperienza del dottorato.

Ai compagni di viaggio/lavoro che ho conosciuto in questi tre anni, e che sono diventati anche cari amici.

Alla mia famiglia, per avermi sempre supportato ed incoraggiato.

A Rita, che mi rende una persona migliore.

A Colui che mi ha donato la presenza di tutti loro: Gesù Cristo, che è Vita e dà la Vita. Spero, in Lui, di poter essere un dono per chi incontrerò come tutte queste persone sono state per me.